

NASA/CR-2000-210653



High-Lift Flight Tunnel

Phase II Report

David Lofftus
MSE Technology Applications, Inc., Butte, Montana

Thomas Lund
University of Texas at Arlington, Arlington, Texas

Donald Rote
Argonne National Laboratory, Argonne, Illinois

December 2000

The NASA STI Program Office ... in Profile

Since its founding, NASA has been dedicated to the advancement of aeronautics and space science. The NASA Scientific and Technical Information (STI) Program Office plays a key part in helping NASA maintain this important role.

The NASA STI Program Office is operated by Langley Research Center, the lead center for NASA's scientific and technical information. The NASA STI Program Office provides access to the NASA STI Database, the largest collection of aeronautical and space science STI in the world. The Program Office is also NASA's institutional mechanism for disseminating the results of its research and development activities. These results are published by NASA in the NASA STI Report Series, which includes the following report types:

- **TECHNICAL PUBLICATION.** Reports of completed research or a major significant phase of research that present the results of NASA programs and include extensive data or theoretical analysis. Includes compilations of significant scientific and technical data and information deemed to be of continuing reference value. NASA counterpart of peer-reviewed formal professional papers, but having less stringent limitations on manuscript length and extent of graphic presentations.
- **TECHNICAL MEMORANDUM.** Scientific and technical findings that are preliminary or of specialized interest, e.g., quick release reports, working papers, and bibliographies that contain minimal annotation. Does not contain extensive analysis.
- **CONTRACTOR REPORT.** Scientific and technical findings by NASA-sponsored contractors and grantees.
- **CONFERENCE PUBLICATION.** Collected papers from scientific and technical conferences, symposia, seminars, or other meetings sponsored or co-sponsored by NASA.
- **SPECIAL PUBLICATION.** Scientific, technical, or historical information from NASA programs, projects, and missions, often concerned with subjects having substantial public interest.
- **TECHNICAL TRANSLATION.** English-language translations of foreign scientific and technical material pertinent to NASA's mission.

Specialized services that complement the STI Program Office's diverse offerings include creating custom thesauri, building customized databases, organizing and publishing research results ... even providing videos.

For more information about the NASA STI Program Office, see the following:

- Access the NASA STI Program Home Page at <http://www.sti.nasa.gov>
- E-mail your question via the Internet to help@sti.nasa.gov
- Fax your question to the NASA STI Help Desk at (301) 621-0134
- Phone the NASA STI Help Desk at (301) 621-0390
- Write to:
NASA STI Help Desk
NASA Center for AeroSpace Information
7121 Standard Drive
Hanover, MD 21076-1320

NASA/CR-2000-210653



High-Lift Flight Tunnel

Phase II Report

David Lofftus
MSE Technology Applications, Inc., Butte, Montana

Thomas Lund
University of Texas at Arlington, Arlington, Texas

Donald Rote
Argonne National Laboratory, Argonne, Illinois

National Aeronautics and
Space Administration

Langley Research Center
Hampton, Virginia 23681-2199

Prepared for Langley Research Center
under Purchase Order L-8871

December 2000

Acknowledgments

The lead author would like to extend his appreciation to his co-authors and their respective organizations for all their hard work and dedication.

In addition, a number of other individuals deserve acknowledgment. At NASA Langley Research Center, Dennis Bushnell for his vision and leadership and Henry Wright for his unwavering support and technical contributions. At MSE, Paul Laird, Doug Rosholt, and Brian Park for their technical contributions and Connie Martin for her careful and patient editing of this and many other reports. Finally at Argonne National Laboratory, Brian Concannon for his technical knowledge and hard work.

The work was conducted through the U.S. Department of Energy–National Energy Technology Laboratory at the Western Environmental Technology Office under DOE Contract Number DE-AC22-96EW96405.

The use of trademarks or names of manufacturers in the report is for accurate reporting and does not constitute an official endorsement, either expressed or implied, of such products or manufacturers by the National Aeronautics and Space Administration.

Available from:

NASA Center for AeroSpace Information (CASI)
7121 Standard Drive
Hanover, MD 21076-1320
(301) 621-0390

National Technical Information Service (NTIS)
5285 Port Royal Road
Springfield, VA 22161-2171
(703) 605-6000

Contents

	Page
Figures.....	v
Tables.....	vii
Acronyms.....	viii
Executive Summary.....	1
Background.....	3
History.....	3
Relationship of Reynolds Number, Mach Number, and Tunnel Size.....	4
Concept Description.....	5
Tunnel System.....	7
Cart System.....	9
Magnetic Levitation System.....	10
Project Participants.....	12
Statement of Problem and Approach.....	13
Problem Definition.....	13
Approach.....	15
HiLiFT Project Research Summary.....	16
Tunnel System Design.....	16
Alternatives Considered.....	16
Design.....	17
Tunnel System Structural Analyses.....	20
Cart and Sting System Design and Analyses.....	24
Requirements.....	24
Material Selection.....	24
Design Characteristics.....	24
Structural Analyses.....	26
Pedestal Mounted Model (Bipod Model Support).....	29
Maglev System.....	30
System Options and Selection.....	30
System Description.....	30
Control Systems.....	35
Aerodynamic Analyses.....	38
Influence of the Cart and Model Support System.....	38
Results.....	38
Effects of Acoustic Waves.....	40
Aerodynamic Loads.....	47
Flow Establishment Time.....	48
Background Disturbance Levels.....	54
Thermal Analyses.....	56
Selection of Insulation.....	56
Free Convection.....	57
Cooldown Simulations.....	59
Set Point Simulation.....	62
Structural Supports.....	62
Infrastructure Design.....	62
Buildings and Grounds.....	62
Electrical.....	63
Nitrogen System.....	64

Contents (Cont.)

	Page
Data Quality.....	66
Coefficients of Lift and Drag.....	66
Pitch, Roll, and Yaw Errors.....	69
Operating Cost Analysis.....	70
Construction Cost and Schedule.....	73
Conclusions and Recommendations.....	76
References.....	78

Figures

	Page
1. Variation of Reynolds Number with Temperature for Various Pressures at Mach 0.3.	5
2. Chord Reynolds Numbers of Existing Commercial Aircraft.	5
3. Artist’s Concept of the HiLiFT Facility.	6
4. Internal View of the HiLiFT Concept.	7
5. HiLiFT Velocity Profiles.	7
6. View of the Entrance End of the Tunnel.	8
7. Isometric View of Cart Construction Details.	10
8. Lift, Guidance, and Thrust Magnet Placement.	11
9a. Diagram of Tunnel Pressure Vessel, Plan View.	18
9b. Diagram of Tunnel Pressure Vessel, Elevation View.	18
10. Distributed Load Midspan Between Support Rings on the Tunnel Shell.	21
11. Maximum Stress on the Tunnel Model from Test-1 Loads.	21
12. Maximum Deflection from Loads on the Test Model.	22
13. ANSYS Output for Mode 1.	23
14. ANSYS Output for Mode 7.	23
15. ANSYS Output for Mode 10.	23
16. Cart and Model Plan View.	25
17. Cart and Model Elevation View.	25
18. Visualization of Mode Shape for Mode 5.	28
19. Visualization of Mode Shape for Mode 8.	28
20. Bipod Mount of the NASA-Ames 12-ft (3.7 m) Pressure Wind Tunnel.	29
21. Cart Magnet Placement.	31
22. Power Circuit and Sectionalizing.	32
23. Effect of a Sequence of –8 kN Pulses of Period 1.2 s and Width 0.02 s on the Oscillations of the Relative Velocity.	33
24. Feedback Control Gain=1,000 V/m/s. Impact on Response to the Same Sequence of Pulses Used in Figure 23.	33
25. Lift/Guidance Magnet (Laminations Parallel to Plane of Page).	34
26. Magnet Control System.	36
27. Response of the Air Gap to the Input Impulse to $\Delta f_a(t)$	36
28. Tunnel Run Simulation Block Diagram.	37
29. Combined Influence of the Cart and Model Support System on the Model.	39
30. Typical Interactions with the Compression Wave.	40
31. Typical Interactions with the Expansion Wave.	41
32. Relative Strength of the Reflected Longitudinal Acoustic Wave.	43
33. Longitudinal Acoustic Wave Shape.	44
34. Proposed End Wall Damping System.	45
35. Time History of the Relative Strength of the Reflected Oblique Acoustic Waves.	47
36. Lift History for the Unsteady Wing Motion.	49
37. Approach to Steady State as Characterized by the Lift Deficit.	49
38. Flow Establishment Time as a Fraction of Available Test Time, Plotted as a Function of Mach Number.	50
39. Typical Lift Error due to Nonequilibrium Flow During a Continuous Pitch Change Maneuver.	52
40. Residual Lift Error from Corrected Measurement Values Obtained during a Continuous Pitch Change Maneuver.	53
41. Decay of Residual Turbulence Between Runs.	55
42. Total Insulation Capital Cost Plus Nitrogen Consumption Costs for 20-Year Hilift Tunnel Life (Multiple Tunnel Diameters).	57

Figures (Cont.)

	Page
43. Equilibrium Free Convection Velocity Distribution for HiLiFT Tunnel, 3 ft (0.91 m) of Foam Insulation.....	58
44. Predicted Temperatures of Bulk Gas and Tunnel Top/Sides/Bottom from Uniform Initial Condition of $-250\text{ }^{\circ}\text{F}$ ($-157\text{ }^{\circ}\text{C}$).....	59
45. Tunnel Shell Components Cooldown, LN_2 Injection into Bulk Tunnel Gas, 950,000 lb/hr (430,000 kg/hr), 2 atm (0.2 MPa) pressure.	60
46. Predicted Circumferential Tunnel Cooldown Temperatures, LN_2 Injected Behind Acoustic Insulation, 200,000 lb/hr (90,700 kg/hr) Total Nitrogen Flow.	61
47. Predicted Circumferential Tunnel Cooldown Temperatures, LN_2 Injected Behind Acoustic Insulation, 400,000 lb/hr (181,400 kg/hr) Total Nitrogen Flow.	61
48. Overall HiLiFT Facility General Arrangement.....	63
49. HiLiFT Electrical System 1-Line Diagram.....	64
50. Nitrogen System Process Flow Diagram.....	65
51. Operational Sequence for Test Program.....	72
52. Project Schedule.....	75

Tables

	Page
1. HiLiFT Baseline Configuration Requirements	13
2. Required Model Range of Motion	14
3. HiLiFT Data Quality Measures.....	14
4. Baseline HiLiFT Model Loads, Including a High Lift Case and a High Side Force Case	14
5. HiLiFT Operational Productivity Criteria.....	14
6. Table of Tunnel Design Requirements.....	17
7. Tunnel Modal Frequencies and Mode Shapes	22
8. Cart and Sting Design Requirements	24
9. Summary of Static Deflections—Baseline Case.....	26
10. Modal Analysis Summary.....	28
11. Major 12.5 kV Switchgear Required and Loads Served.....	64
12. Coefficient of Drag/Coefficient of Lift Error Sources from Free- Stream and Non-Free-Stream Effects and Approach to Mitigating Them.....	67
13. Sources of Attitude Error In Pitch, Roll, and Yaw.....	69
14. Angle of Attack/Roll Angle/Yaw Angle Error Sources and Approach to Mitigating Them	69
15. Rough-Order-of-Magnitude Costs for Tunnel Operations.....	70
16. Table of Operational Costs.....	71
17. Detailed Cost Computation Table for Selected Operational Example.....	72
18. Project Phases and Cost Estimation Confidence Levels	74
19. Project Construction Cost Estimate Summary	74
20. Total Project Cost Summary	75

Acronyms

amp	amperes
ANL	Argonne National Laboratory
ASME	American Society of Mechanical Engineers
ASTM	American Society for Testing and Materials
atm	atmosphere
BMS	bipod model support
Btu	British thermal unit
CFD	Computational Fluid Dynamics
cm	centimeters
EDS	ElectroDynamic Suspension
EMS	ElectroMagnetic Suspension
FEA	finite element analysis
FRP	fiber-reinforced-plastic
ft	feet
ft ³	cubic feet
GASL	General Applied Science Laboratories, Inc.
gpm	gallons per minute
HiLIFT	High-Lift Flight Tunnel
Hz	hertz
ID	inner diameter
I&C	instrumentation and control
in	inch, inches
K	Kelvin

Acronyms (Cont.)

kA	kiloampere
kg	kilograms
kN	kilonewton
kPa	kiloPascal
kV	kilovolt
kW	kilowatt
kW-hr	kilowatt hour
lb	pound(s)
LGM	lift and guidance magnets
LIM	linear induction motor
LN ₂	liquid nitrogen
LSM	linear synchronous motor
m	meters
m ²	square meter
m ³	cubic meter
MJ	megajoules
mm	millimeters
MOP	maximum operating pressure
MPa	megaPascal
mph	miles per hour
MSE	MSE Technology Applications, Inc.
MW	megawatt
NASA-Ames	NASA Ames Research Center
NASA-LaRC	NASA Langley Research Center

Acronyms (Cont.)

NWTC	National Wind Tunnel Complex
psi	pounds per square inch
psig	pounds per square inch gauge
R&D	research and development
ROM	rough-order-of-magnitude
s	second
SCM	superconducting magnet
UTA	University of Texas at Arlington

Executive Summary

The High-Lift Flight Tunnel (HiLiFT) concept is a revolutionary approach to aerodynamic ground testing and it was an outgrowth of the National Wind Tunnel Complex (NWTC) study. Contrary to conventional wind tunnels where the test medium is moved over a stationary model, the HiLiFT concept utilizes emerging magnetic levitation and linear motor technologies from the high-speed ground transportation industry to propel the model through a tube containing a quiescent test medium. The test medium (nitrogen) in HiLiFT is temperature-controlled and pressurized to achieve low-speed Reynolds numbers higher than any existing ground test facility in the world. In addition to flight Reynolds number capability, the quiescent test medium of the HiLiFT concept is expected to provide low disturbance and acoustic testing capabilities currently unavailable anywhere in the world.

A Phase I study, completed in February 1998, established that the technology exists to construct a HiLiFT ground test facility. Phase II, which is the subject of this report, was completed in July 1999 and validated the technology with analytical assessments as well as conceptual design. Phase III, if funded, will demonstrate the technology with the implementation of a pilot facility and appropriate experiments.

The approach to Phase I was to establish that critical enabling technologies required for HiLiFT are, or would be, available in the timeframe necessary for HiLiFT development. The Phase I effort showed that the magnetic levitation and linear motor technologies are available, but no fully comparable system has previously been designed and tested. During Phase I, the pressure vessel and cryogenic systems were determined to be feasible. Initial construction cost estimates were also established, but additional design of high risk systems were required to validate costs. Outputs of the Phase I study included recommendations that component design and sizing of maglev and linear motor systems be conducted; model dynamics and attitude control be investigated and quantified, and a comprehensive productivity study be performed.

The Phase II objective was to thoroughly examine the HiLiFT concept relative to the facility requirements derived from the NWTC study. Phase II activities included a comprehensive feasibility study, which particularly addressed the critical elements identified in the Phase I studies. The HiLiFT feasibility study was instituted to validate that the concept of a large-scale pressurized, cryogenic tube was technically feasible and to determine its construction and operating costs. Study participants included National Aeronautics and Space Administration Langley Research Center (NASA-LaRC) as the Program Manager and MSE Technology Applications, Inc. (MSE) of Butte, Montana as the prime contractor and study integrator. MSE's subcontractors included the University of Texas at Arlington (UTA) for aerodynamic analyses and the Argonne National Laboratory (ANL) for maglev and linear motor technology support.

The current design concept calls for the HiLiFT to be a 20-foot (ft) (6.1-m) diameter stainless steel tube possessing a clear 16-ft (4.9-m) diameter space in the center for testing. The tunnel is one-half mile in length, with thermal insulation installed on the outside and acoustic damping material on the inside. It will be pressurized to 7.5 atmospheres (atm) using nitrogen at $-250\text{ }^{\circ}\text{F}$ ($-157\text{ }^{\circ}\text{C}$). The required temperature and pressure will be maintained by carefully controlled injections of liquid nitrogen. A set of two isolation valves on one end will allow models to enter or leave the test chamber while the tunnel is being held at test conditions. Models can be tested at full flight Reynolds number from 0.05 to 0.50 Mach with accelerations up to 3 g (29.3 m/s^2).

The Phase II design and analytical studies concentrated on determination of the aerodynamic environment within the tunnel, model cart design, magnetic levitation and propulsion system analyses and design, test thermal environment, and HiLiFT construction cost and schedule estimates. Additional Phase II activities

included analyses of operating cost, safety, productivity, and performance. It was determined that a national HiLiFT facility, including a smaller pilot facility, can be constructed for a cost of approximately \$400M, and it could be operational by 2013 if fully funded. The design studies validated the Phase I conclusion that the HiLiFT facility is feasible to build and operate with reasonable extensions of existing technology, and the analytical studies revealed no insurmountable difficulties to realizing a practical high Reynolds number ground test facility. However, significant work remains in order to realize the promise shown by the study, particularly in the area of the model cart design and model attitude control.

In summary, the Phase II feasibility study described in this report provides excellent assurance that the HiLiFT concept will provide a valuable low-speed, high Reynolds number ground test facility. During Phase III, the emphasis should be on concept and system demonstration using simplified or subscale hardware. Key activities include tunnel design and manufacture, thermal design and analysis, maglev system design and operation, model cart design and performance, and aerodynamic performance. At the conclusion of Phase III, all key hardware and concepts will have been validated, and the results of the testing and analysis will have been incorporated into a single system design. Full-scale and detailed design efforts can follow Phase III with confidence in technology, implementation, expected data quality and quantity, and cost and schedule estimates.

Background

History

In October of 1996, NASA-LaRC initiated an effort to develop new subsonic, high Reynolds number ground testing concepts. The objective of this initiative was to conceive of a means to achieve subsonic flight Reynolds number test capability, on the order of 70 million, in a more cost-effective manner than that offered by conventional wind tunnel approaches. The initiative was spearheaded by NASA-LaRC's Chief Scientist and the study was conducted by NASA-LaRC's Systems Engineering Competency.

The first research facility concept considered was a large, cryogenic Ludweig tube proposed by General Applied Science Laboratories, Inc. (GASL). The proposed Ludweig tube was 24 ft [7.3 meters (m)] in diameter, 2,500-ft (763-m) long, and pressurized to 10 atm [1.0 megaPascal (Mpa)] with $-250\text{ }^{\circ}\text{F}$ ($-157\text{ }^{\circ}\text{C}$) gaseous nitrogen. These design parameters provided approximately 5 seconds of subsonic testing at the target Reynolds number. However, it was found that each 5-second operation cycle (or shot) exhausted 750 tons [$6.8 \cdot 10^5$ kilograms (kg)] of gaseous nitrogen at a cost of approximately \$75,000.

Although the large cryogenic Ludweig tube was found to be cost prohibitive, it initiated a series of further investigations into other "pulse type" ground testing techniques. It was through these investigations that the HiLiFT was conceived by the systems engineering competency.

The HiLiFT is a revolutionary new approach to aerodynamic ground testing. Contrary to conventional wind tunnels where the test medium is driven over a stationary model, the HiLiFT concept utilizes emerging magnetic levitation and linear motor technologies from the high-speed ground transportation industry to propel the model through a tube containing a quiescent test medium (air or nitrogen). Unlike traditional tow tanks, the test medium in the flight tunnel is temperature controlled and pressurized to achieve low-speed Reynolds numbers higher than any existing test facility in the world. Utilizing various combinations of pressure and temperature, HiLiFT can provide: 1) a full-span Reynolds number of 70 million at Mach 0.3 equivalent to that of a Boeing 747 transport; or 2) a Reynolds number of 1 billion equivalent to that of a U.S. Navy Los Angeles class submarine. In addition to flight Reynolds number capability, the quiescent test medium of the HiLiFT concept is expected to provide low disturbance and acoustic testing capabilities unavailable in the world today.

The current methods and facilities used to perform subsonic aerodynamic testing are primarily continuous flow wind tunnels driven by fans or compressors. These wind tunnels are large, complex, expensive facilities with numerous ancillary systems. A small number of conventional wind tunnels utilize pressure and cryogenic fluids, usually nitrogen, to achieve higher Reynold's numbers. However, both the capital costs and operating costs of these facilities are very high due to their complexity, power requirements, and nitrogen consumption. Other disadvantages of conventional facilities include high noise levels from the fan system resulting in detrimental test section turbulence and low reliability or productivity due to the overall complexity of the facility.

The flight tunnel consists of a sealed tube, a high-speed transportation system, and a mobile model support cart as its primary components. The tube is filled with air or gaseous nitrogen at a given temperature and pressure. The model support cart is then accelerated via a magnetic levitation and/or a linear motor system. Once the desired test velocity is reached, the velocity is maintained constant by the magnetic levitation/linear motor systems for a specified period of time before the model support cart is

decelerated. Test data gathered during the run is stored onboard the model support cart for future retrieval or sent to an outside data acquisition system by wireless transmission.

Relationship of Reynolds Number, Mach Number, and Tunnel Size

The design objective of the HiLiFT facility is to duplicate the true flight Reynolds numbers and Mach numbers for a wide variety of commercial and military flight vehicles. The Reynolds number and Mach number of an aircraft traveling in a gaseous medium are governed by the following equations.

Reynolds number = $\frac{\rho LV}{\mu}$ where:

- ρ gas density [kg/square meter (m^2)]
- L characteristic length (usually nominal wing chord length) (m)
- V velocity of aircraft [m/second (s)]
- μ gas viscosity ($N \cdot s/m^2$)

Mach Number = $\frac{V}{a} = \frac{V}{\sqrt{\gamma RT}}$ where:

- V velocity (m/s)
- a speed of sound in gas (m/s)
- γ ratio of specific heats of gas = C_p/C_v
- R gas constant ($J/kg \cdot K$)
- T temperature of gas (K)

Pressure effect: When the pressure is changed, the density changes proportionately according to the ideal gas law. Other parameters essentially remain the same with pressure; therefore, the Reynolds number is essentially directly proportional to pressure.

Temperature effect: Density, velocity, and viscosity all change with temperature. Density changes in accordance with the ideal gas law. Velocity changes because the velocity is equal to the test Mach number times the speed of sound, and the speed of sound changes with the square root of temperature. The viscosity of air or nitrogen also changes with temperature.

The primary design goal for the HiLiFT concept was to achieve a Reynolds number of 55 million per foot at Mach 0.3. Using the previously cited relations for Mach number and Reynolds number yields the Reynolds number/temperature curves at varying pressures shown in Figure 1. The operating point selected was -250 °F (-157 °C) at 7.5 atm (0.76 MPa). This gave approximately a 1/19-scale model and a velocity of 225 ft/s (153 miles per hour (mph) or 68.6 m/s) at Mach 0.3. A diagram showing how the proposed HiLiFT compares with existing, conventional wind tunnels and with the chord Reynolds numbers of existing commercial aircraft is presented in Figure 2.

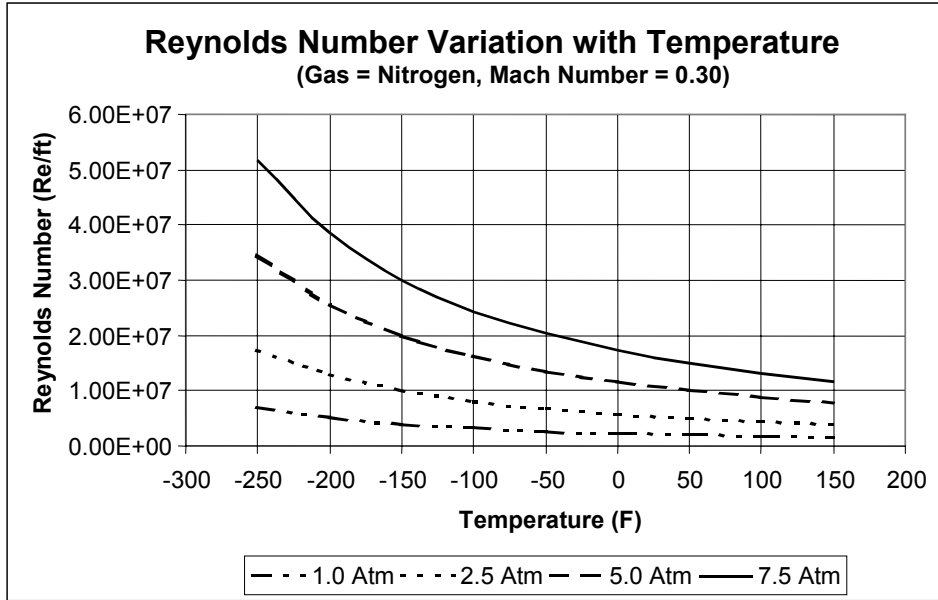


Figure 1. Variation of Reynolds number with temperature for various pressures at Mach 0.3.

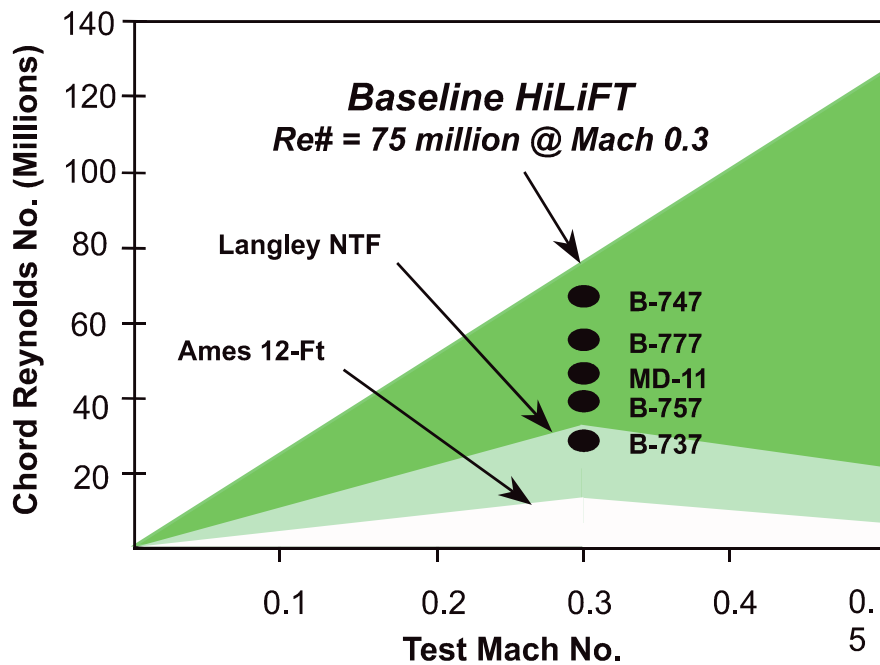


Figure 2. Chord Reynolds numbers of existing commercial aircraft.

Concept Description

The current design concept for the HiLiFT is a circular cross-section cylinder 20 ft (6.1 m) in diameter and 2,500-ft (762-m) long, with a 16.5-ft (5-m) diameter useable clear space in the tunnel center for

“flying” the models. The tunnel is pressurized with nitrogen ranging from 1 to 7.5 atm (0.1 to 0.76 MPa) of internal pressure and from +70 °F (+21 °C) to –250 °F (–157 °C) in temperature. The tunnel walls and support structure will be fabricated from stainless steel and mounted on concrete foundations set every 50 ft (15.2 m). The end of the tunnel nearest the facility support building will be firmly attached to the foundation, while the other end will be allowed to expand and contract by moving on roller bearings. A magnetic levitation and propulsion (maglev) system will be mounted on a rail support system within the tunnel, which also serves to stiffen the tunnel, thus reducing the structural effects of the cart and model accelerating through the tunnel. A pressure lock system will be employed as a means of moving models in and out of the tunnel so they can be modified and maintained while allowing the tunnel to remain at operating temperatures and pressures. Antireflective materials will be used for the tunnel walls to minimize the effects of reflected acoustic waves.

An early artist’s concept of what the HiLiFT facility might look like from the outside is shown in Figure 3, and the early artist’s concept of what the interior of the tunnel might look like as the cart and model are being moved into position is shown in Figure 4. The velocity profiles for various Mach numbers and the length of the available test time are given in Figure 5.

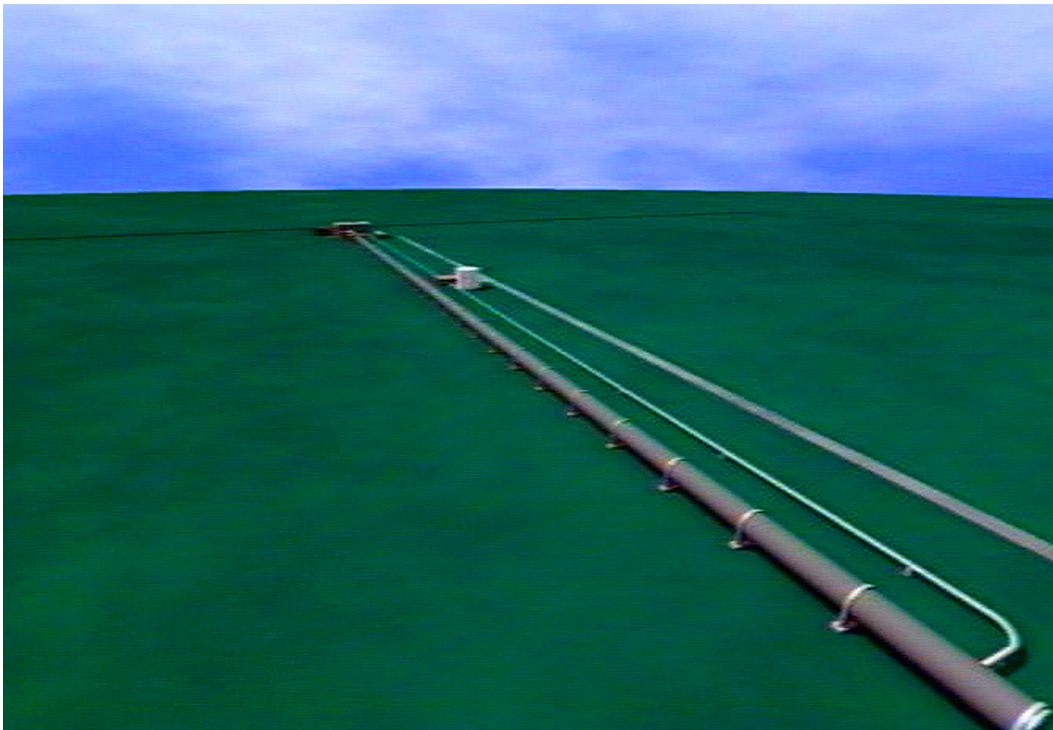


Figure 3. Artist’s concept of the HiLiFT facility.

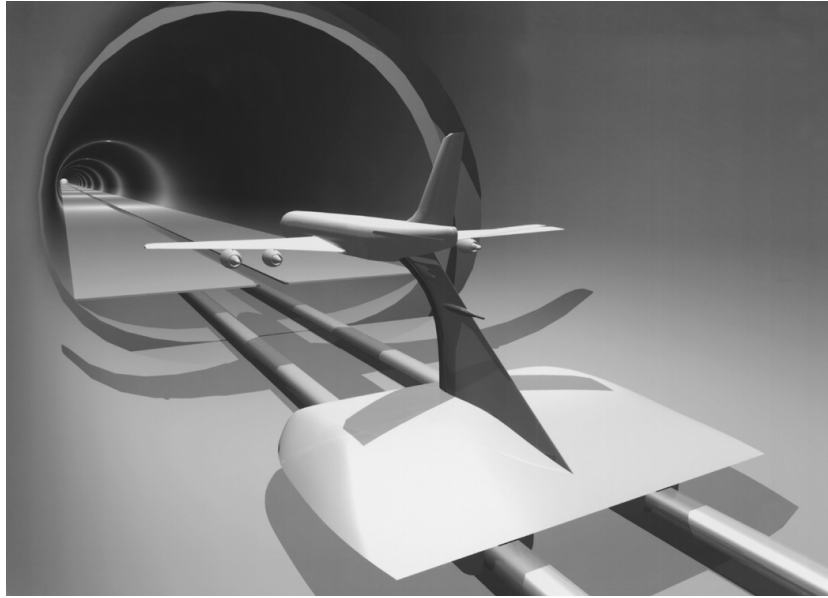


Figure 4. Internal view of the HiLiFT concept.

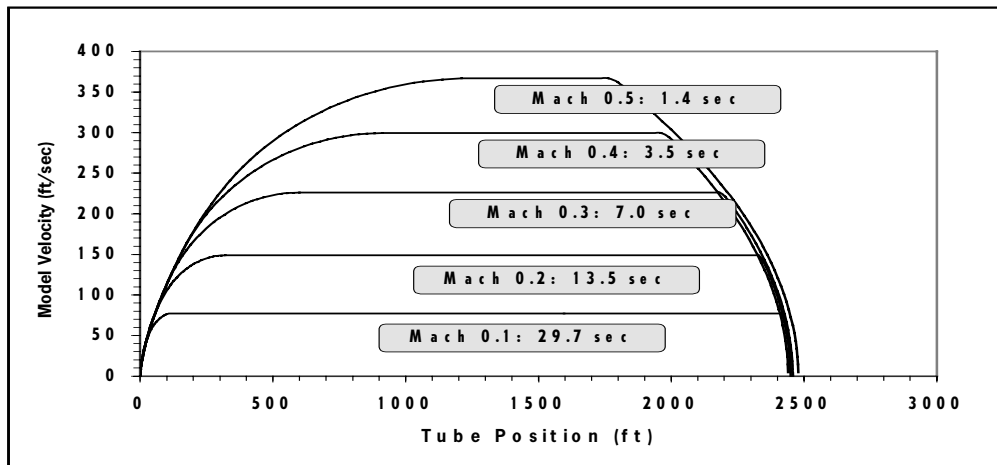


Figure 5. HiLiFT velocity profiles.

Tunnel System

The tunnel pressure vessel shell has an internal diameter of 20 ft (6.1 m) and a test section 2,500-ft (762-m) long. The model/cart test preparation section of the vessel is an additional 136-ft (41.5-m) long.

The material chosen for the HiLiFT tunnel design is 304/304L dual certified stainless steel. It was chosen for its high tensile strength, high stiffness, corrosion resistance, and suitability for use at cryogenic temperatures. The entire 2,500-ft (762-m) length of the tunnel shell will be a single welded cylinder. It will be allowed to expand and contract longitudinally from thermal changes and pressure expansion. The entrance end of the 2,500-ft (762-m) long vessel test section will be anchored in place, while the rest of the tunnel will be allowed to move on rollers.

The pressure vessel shell is stiffened and supported with support rings. The support rings will be welded in place on the outer circumference of the pressure vessel shell and will provide an attachment area to support the weight of the pressure vessel shell and its contents on the rolling support cradle structures located under the pressure vessel. The support rings add stiffness to maintain the round shape of the thin wall shell for the cylindrical pressure vessel. They will be 2-inches (in) [5.1-centimeters (cm)] thick by 24-in (61-cm) high and located at 50-ft (15.2-m) intervals along the length of the pressure vessel shell. The bottom portion of the outer diameter of each support ring is set in and supported by a cradle in the top portion of the rolling supports. A cut-away view of the entrance end of the tunnel showing the cart and model is shown in Figure 6.

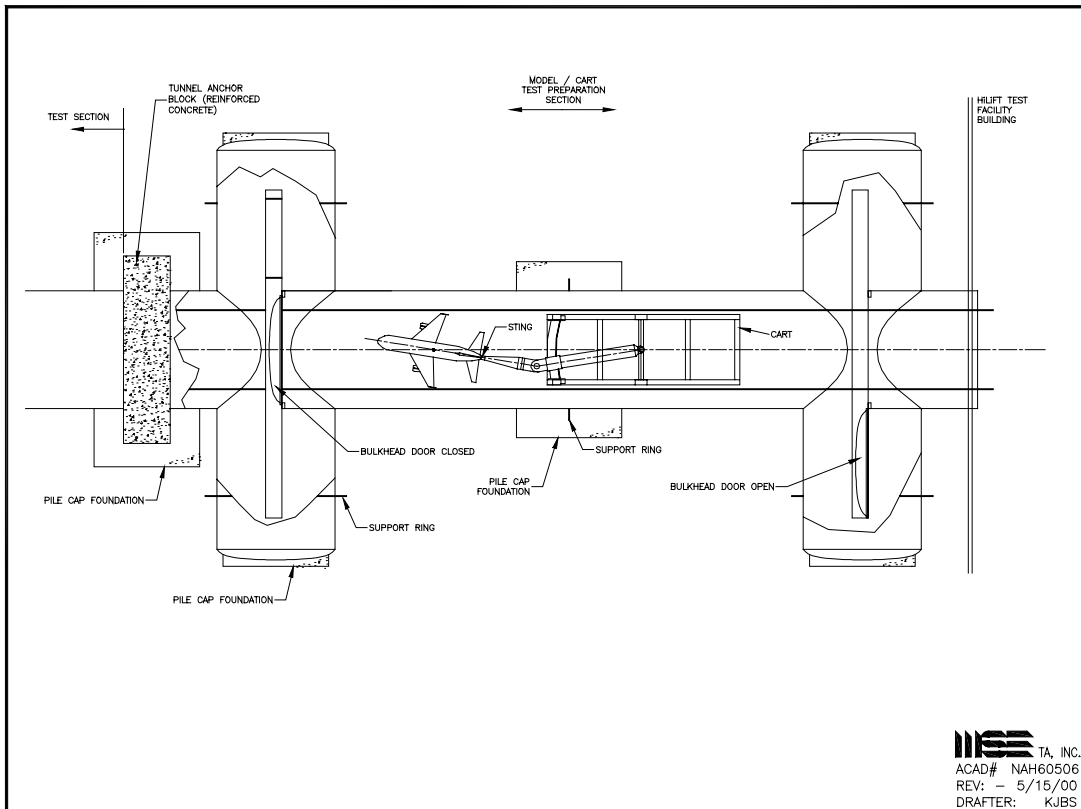


Figure 6. View of the entrance end of the tunnel.

The support cradles are mounted on roller bearings that allow movement in the tunnel longitudinal direction from expansion and contraction of the vessel shell due to thermal changes. The first support cradle will have a longitudinal movement of just over 2 in (5.1 cm), while the last support cradle at the far end of the pressure vessel will have a longitudinal movement of approximately 106 in (2.7 m). The roller bearing tracks require a vertical and lateral adjustment mechanism capable of lifting and moving the entire tunnel structure to maintain the pressure vessel alignment.

The Maglev lift magnets, thrust magnets, and guidance magnets will attach to angle mounting rails, which will be welded to the inside bottom surface of the pressure vessel shell. There are two mounting angles for the right and left lift magnets, two mounting angles for the right and left thrust magnets, and one mounting angle for the guidance magnets.

The model/cart test preparation section of the tunnel shown in Figure 6 will be fitted with two pressure-tight movable bulkhead doors. These doors will allow the tunnel test section operating pressure and temperature to be maintained while the cart and model are removed from the test section for maintenance or modification. The outer circumference of the bulkhead doors will be pulled tightly against their sealing surface using electrically driven clamping bolts.

The tunnel of the HiLiFT will be thermally insulated and jacketed with a closed-cell silica glass insulation to minimize heat gains and attendant operating costs. The pressure vessel shell, support rings, and vessel-stiffening frame will be covered with thermal insulation. Six-inch (15.2 cm) thick custom manufactured curved panels that fit the curvature of the pressure vessel are laminated together to make a composite 36 in (0.91 m) insulation layer around the tunnel.

Acoustic wedges (as used in anechoic chambers) will be installed on the inside surface of the pressure vessel shell for sound wave attenuation. The acoustic wedges will be installed on the upper approximately 75% of the circumference of the shell wall and will extend along the entire 2,500-ft (762-m) test section.

Cart System

The baseline cart/model support system consists of a deck structure to house the suspension and propulsion magnets and an adjustable boom assembly to support the model/balance subassembly. The entire structure is constructed of graphite/epoxy composite except for bearings and metallic positioning mechanisms, end fittings for composite members, fairing plates, and fasteners. An isometric view of the details of cart construction is shown in Figure 7.

Vertical structural supports for the main boom and positioning hardware are also graphite/epoxy composite. The aft boom is attached to the aft supports and rear shaft. Teflon® bearings support the boom rear yoke and shaft. The forward vertical supports and yaw traverse support are arcs with a 16-ft (4.9-m) center of curvature. The boom assembly serves to position the model/balance. It is supported by tandem pitch positioners actuated by electric ball screws, as well as a yaw positioner that is also actuated by an electric ball screw. The main boom is a hollow 24-in (61-cm) diameter, 3-in (7.6-cm) wall, graphite/epoxy composite member that bears all the loads transmitted to it from the balance and sting. It is made from the same materials as the other structural members.

A “knuckle” and two roll mechanisms are mounted at the forward end of the boom. The knuckle is a simple hinge consisting of an outer yoke attached to the aft piece of the boom and a steel pivot pin mounted to the forward piece of the boom. The pivot pin rotates in two Teflon bearings mounted in the outer yoke. Since the knuckle can only move in one plane, the first roll mechanism keeps the knuckle plane congruent with the plane defined by the tunnel centerline and the center of the knuckle. Model position is adjusted by simultaneously moving the center boom pitch and yaw positioners, knuckle, and first roll mechanism for the desired pitch/yaw combination. The second roll mechanism establishes the desired model roll. All actuator mechanisms are enclosed in structural members so they can be insulated and heated for reliable operation. Antibacklash gearing, preloaded bearings, and close manufacturing tolerances will be specified for all commercial items to minimize free play in the model positioning system. Fairing shapes are applied to the knuckle and the leading and trailing edges of major structural members for a more streamlined cart.

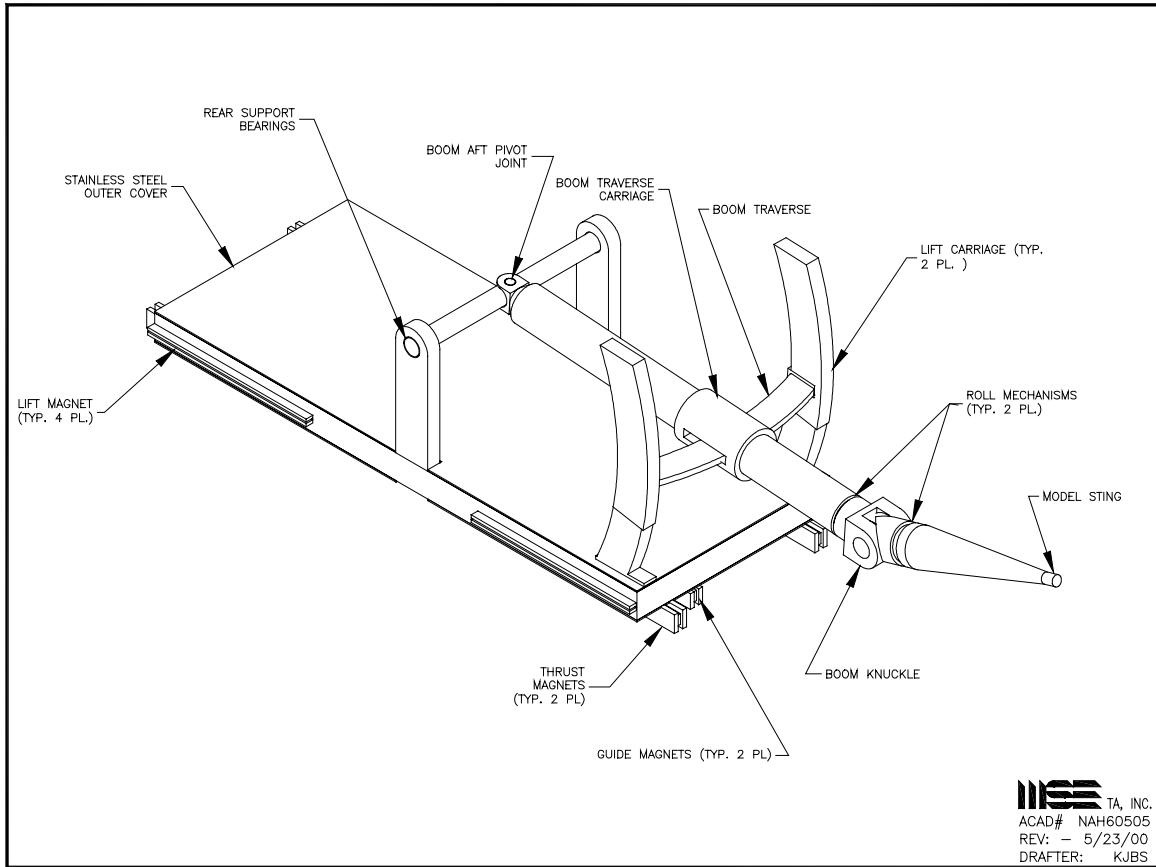


Figure 7. Isometric view of cart construction details.

Calculated cart weights indicate a cart made primarily of AS-4 graphite/epoxy composites is less than 60% the weight of a cart fabricated entirely of steel at 25,200 pounds (lb) (11,431 kg) vs. 39,500 lb (17,917 kg) and approximately the same weight of a cart fabricated primarily of titanium at 27,780 lb (12,601 kg). The net effect of extra weight is twofold. First, it requires more power to accelerate the cart. The extra cart mass also requires larger magnets, batteries, and power conductors. Second, the additional mass drives the modal frequencies lower, meaning the cart and associated structures will vibrate at lower frequencies.

Magnetic Levitation System

System Selection. A wide variety of technical options spanning a range of magnetic levitation, propulsion, and guidance options and system configurations were examined. The four main candidates identified were:

- An iron-core linear induction motor (LIM) using either single- or double-sided magnets with an attractive-force suspension system;
- An iron-core linear synchronous motor (LSM) used in combination with an attractive-force suspension system (the ElectroMagnetic Suspension (EMS) option);

- An air-core LSM used in combination with a null-flex repulsive-force suspension system using superconducting magnet technology (the ElectroDynamic Suspension (EDS) option); or
- A permanent magnet, repulsive force system.

The LIM option was discarded for a variety of technical reasons including poor speed control and poor power factor (less efficient operation) leading to increased tunnel heating. The permanent magnet option was added late in the selection process but was discarded since it is not fully developed, and involved too many developmental risks. Therefore, the choice was between the EMS and the EDS options.

In this design, the greatest emphasis was placed on the more practical issues such as minimizing technical risk and satisfying the stringent magnet position control requirements. The EMS system had the advantage since it required magnet air gap control for normal operation; therefore, the need to meet specific HiLiFT project control requirements was more of a refinement step than the development of a new technology. The EDS system does not normally require control of the magnets to maintain the air gap clearances, and therefore, to meet specific control requirements meant developing a new control technology for superconducting magnets (SCM). For these reasons the EMS option was selected for HiLiFT.

Separate magnets were designed for use as lift, guidance, and thrust magnets. A total of two thrust magnets were required, along with two guidance magnets and four lift magnets. Their placement is shown in Figure 8.

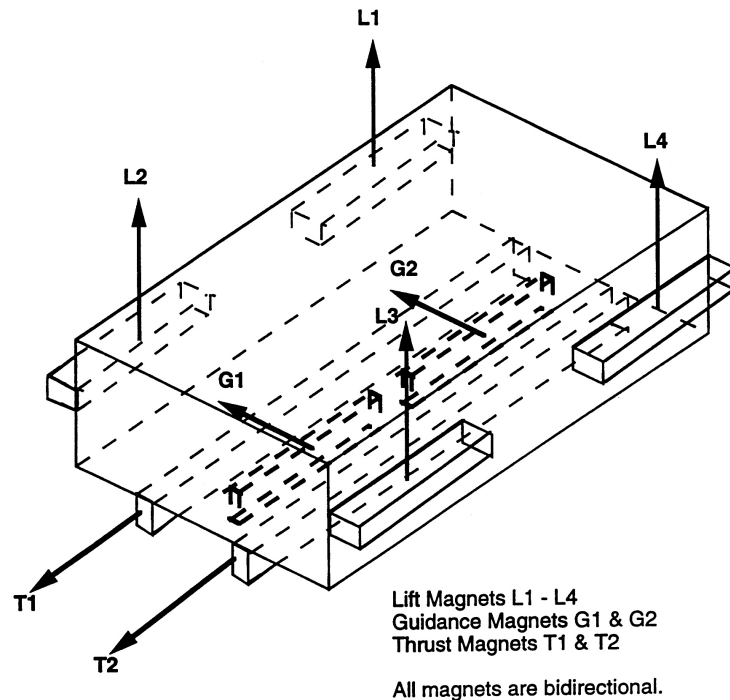


Figure 8. Lift, guidance, and thrust magnet placement.

Thrust Motors. The thrust motors are LSMs and are used to accelerate and decelerate the cart. The thrust magnets are located along the bottom of the cart, on either side of the centerline. The LSM stators

are mounted along the length of the tunnel. The thrust motors are double sided and are driven with a three-phase power supply capable of variable voltage and frequency operation. Energizing the three-phase winding gives rise to alternating north and south magnetic poles that travel smoothly in the direction of cart travel and pull/push on the mating poles of the cart thrust magnets.

Lift and Guidance Magnets. The lift and guidance magnets (LGM) are of the same basic design and operation, except that the lift magnets must be energized at all times the cart is moving to counteract gravity as well as vertical forces, while the guidance magnets only counteract horizontal forces. The lift and guidance magnets are a double gap design where only one gap at a time is energized. This allows bidirectional control with a single magnet set. There are a total of four lift magnets arranged along the sides of the cart at the four corners. Additionally, there are two guidance magnets underneath and along the length of the cart that are slightly offset from the centerline. The reaction rails are attached to the tunnel.

The electric power required on the cart will be provided by batteries. This power is used for LSM thrust magnets, lift and guidance magnets, heating electronics and battery compartments, and running control and communications electronics. To supply this power, lithium-ion batteries were selected. Each cart magnet will have its own controller and feedback sensors. The batteries must be kept in a temperature-controlled compartment to protect them from freezing and maximize the system performance. The electrolytes are in gel form and will not be affected by the high accelerations experienced.

Control Subsystems. The magnet control subsystem performs the following functions:

- Maintains the air gaps to a predetermined tolerance—this prevents the magnet surfaces from contacting the guideway surfaces, as well as maintaining the required limits on cart orientation.
- Adjusts the magnet currents (forces) to compensate for changes in load as a function of time.

These two functions are closely related, since preservation of the air gap requires adjustments to be made in the magnet current to compensate for changes in applied or disturbance forces. In addition to compensating for applied or disturbance forces, the control system must also make adjustments to compensate for any irregularities in the critical guideway surfaces caused by static or dynamic loads or temperature changes.

Project Participants

Participants in this study included the following:

NASA-LaRC – concept origination, program management, funding source

MSE – Prime Integrating Contractor and Project Manager, tunnel design and analysis, cart design and analysis, thermal analysis, infrastructure design, cost analysis

ANL – Maglev system design and analysis, effects of cryogenic temperatures

UTA – aerodynamic analyses

Statement of Problem and Approach

Problem Definition

The HiLiFT feasibility study was instituted to determine if the concept of a large-scale pressurized, cryogenic tube with a moving research model was technically feasible and, if so, determine its construction and operating costs. The level of performance that could be expected for low-speed, high-lift testing was also evaluated. The three areas of study can be summarized as:

- Technical feasibility
- Construction and operating costs
- Operating performance

The basic research requirements for the HiLiFT facility were determined by NASA-LaRC and are delineated in Tables 1 through 5. These requirements were derived through recommendation from NASA-LaRC research personnel and from the findings of NASA’s NWTC Project. Between 1990 and 1995, the NWTC Project developed conceptual designs of a proposed large-scale subsonic wind tunnel and a proposed large-scale transonic wind tunnel. The subsonic wind tunnel was to have a test section area similar to that of HiLiFT and was to operate in a similar Mach number and dynamic pressure test regime. Therefore, it was felt that the research requirements for HiLiFT would be similar to that of the proposed subsonic wind tunnel.

In one case, the HiLiFT study team proposed a significant departure from the NWTC subsonic wind tunnel requirements. This departure was in the area of turbulence intensity (see Table 3). The NWTC requirement for turbulence intensity was 0.05%, but because the HiLiFT facility is envisioned to provide a quiescent test medium for low-noise acoustic research, the turbulence intensity requirement was revised to 0.005%. This requirement is particularly stringent, and as described later in this report, is extremely difficult to achieve.

Table 1. HiLiFT Baseline Configuration Requirements

Baseline configuration	
Test concept	Stationary medium, magnetically propelled model
Core test volume	16 ft (4.88 m) circular, 2,500-ft (762-m) long
Test medium	Nitrogen
Test pressure	1 atm (0.10 MPa) to 7.5 atm (0.76 MPa) absolute
Test temperature	+70 °F (21 °C) to -250 °F (-157 °C)
Mach number range	0.05 to 0.50
Full span Reynolds number	$55 \cdot 10^6$ /ft-chord ($16.8 \cdot 10^6$ m-chord) at Mach 0.3
Operating cycle	Seven days per week, three shifts per day
Allowable model acceleration/deceleration	3.0 g (29.3 m/s ²)

Table 2. Required Model Range Of Motion

Model range of motion	
Angle-of-attack range	+20 to -10 degrees referenced from horizontal plane
Yaw range	+16 to -16 degrees referenced from vertical plane
Roll range	±180 degrees from tunnel longitudinal axis
<p>Maximum angles may occur simultaneously. The entire model shall stay within core test volume for all combined ranges of motion. The model center-of-pressure shall stay within ±2 inches (5.08 cm) of the center of the core test volume for all combined ranges of motion.</p>	

Table 3. HiLiFT Data Quality Measures

Data quality measures	
Pitch angle data	Corrected to within ±0.01 degree
Yaw angle data	Corrected to within ±0.02 degree
Roll angle data	Corrected to within ±0.01 degree
Drag coefficient (C_D)	Corrected to within 0.0005 at Mach 0.3 (0.2%, see section on free-stream errors)
Lift coefficient (C_L)	Corrected to within 0.005 at Mach 0.3 (0.2%, see section on free-stream errors)
Initial turbulence intensity	0.005% RMS between 1 Hz to 200 kHz at Mach 0.3

Table 4. Baseline HiLiFT Model Loads, Including A High Lift Case And A High Side Force Case

HiLiFT model loads		
Load type	High lift load case	High side force load case
Lift load	0 to ±52,210 lb (232.2 kN)	0 to ±29,760 lb (132.4 kN)
Drag load	0 to 13,214 lb (58.78 kN)	0 to 13,214 lb (58.78 kN)
Side load	0 to ±585 lb (2.60 kN)	0 to ±3,655 lb (16.26 kN)
Pitching moment	0 to ±35,917 ft-lb (48.70 kN-m)	0 to ±29,811 ft-lb (40.42 kN-m)
Rolling moment	0 to ±37,310 ft-lb (50.59 kN-m)	0 to ±12,312 ft-lb (16.69 kN-m)
Yawing moment	0 to ±8,047 ft-lb (10.91 kN-m)	0 to ±8,941 ft-lb (12.12 kN-m)
Model dead weight	0 to 1,393 lb (6,196 N)	0 to 1,393 lb (6,196 N)
<p>Model support structures shall be designed for a dynamic load range of ±25% of the maximum combined static loads. Model support structures shall be designed for an impulse loading of 50% of the maximum combined static loads.</p>		

Table 5. HiLiFT Operational Productivity Criteria

Productivity criteria	
Shell pressurization rate	1 psi (6.9 kPa) per minute
Shell depressurization rate	1 psi (6.9 kPa) per minute
Minimum tunnel cool-down rate	0.5 °F (0.28 °C) per minute
Minimum tunnel warm-up rate	0.5 °F (0.28 °C) per minute
Minimum test run rate	8 runs per hour
Data collection rate	20 data points per occupancy hour
Data collection cost	\$250 per data point

Approach

The approach taken to completing the Phase II feasibility was to focus on key analyses and subsystems that were identified during both Phase I and Phase II project planning efforts.

Key items addressed during the feasibility study include:

- tunnel structure design;
- cart design;
- aerodynamics analysis of the tunnel environment;
- magnetic levitation and propulsion design; and
- thermal environment within the tunnel.

Other items that were studied in less detail include:

- nitrogen supply system design;
- power supply system design;
- buildings and grounds;
- systems safety issues;
- operational costs; and
- system productivity.

The roles and responsibilities of the various team members included:

- NASA-LaRC – requirements development and productivity studies;
- MSE – project management, systems integration, structural design and analysis of the cart and tunnel subsystems, thermal analyses, nitrogen subsystem design, buildings and grounds, power subsystem design, safety analyses, and operations cost estimation;
- ANL – magnetic levitation and propulsion subsystem design; and
- UTA – aerodynamics analyses.

HiLiFT Project Research Summary

Tunnel System Design

The basic configuration of the HiLiFT tunnel after the completion of the feasibility study is quite close to the original concept. However, at the beginning of the project, studies were conducted to determine whether better alternatives existed. An overview of these studies is presented in *Alternatives Considered*; full details can be found in Reference 1. The completed design is described in *Design*, and an overview of the analyses conducted on the design is contained in *Tunnel System Structural Analysis*. Full details can be found in Reference 2.

Alternatives Considered

The basic configuration of the tunnel is a linear tube with a circular cross section. Other configurations were investigated to determine whether this could be improved upon including toroidal, center pivot, square and buried with either a flat or domed top and various others. No ideas emerged that were deemed better than the round linear tube. The other options suffered from structural flaws, the need to join materials with dissimilar coefficients of thermal expansion, or excessive cost.

The test article, or model, is powered and guided by a magnetic levitation propulsion system attached to a cart at the bottom of the tunnel. Other placements for the maglev tracks were investigated including an X shape, a three-support structure like an inverted Y, and ring structures. No better approach emerged because the cost of construction to ensure the entire tube was highly dimensionally stable (rather than just the bottom) was prohibitive. In addition, the alternative structures did little to ease the burden on the guidance magnets, which have to counteract large moments and forces.

Suspension techniques other than maglev were also investigated. These included direct magnetic suspension of the model (no model cart), air suspension like a hovercraft, and low friction slides. No cost savings were evident and the other techniques had significant technical difficulties to overcome to operate in the HiLiFT environment. The only other promising technique was the “wheels-on-rail” concept with an appropriate suspension system. If the maglev system proves to be unworkable, wheels-on-rail could be employed.

An investigation was conducted into the best choice for the tunnel materials. Exotic metals, such as titanium, were found to be unduly expensive for the marginal performance gain in this application. Fiber-reinforced-plastic (FRP) and other composite materials are not suited to the manufacture of extremely large structures and have poor fracture resistance, especially at cryogenic temperatures. Concrete may be used at cryogenic temperatures; however, it does poorly with rapid temperature changes and requires sufficient reinforcing steel to serve as a pressure vessel so that any cost advantage is lost. Concrete’s weight and brittleness also count against it. Relatively ordinary metals such as aluminum, high nickel steel, and stainless steel emerged as the only suitable materials for the tunnel. The cost of constructing the tunnel from each material was nearly the same; however, the 304/304L stainless steel was chosen for its high tensile strength, high stiffness, corrosion resistance, and suitability for use at cryogenic temperatures.

The question of whether to make the tunnel a solid piece and contend with the large movement due to thermal expansion and contraction or use expansion joints was addressed. Inquiries to expansion joint manufacturers revealed that the HiLiFT would be too large for expansion joints to be feasible.

A critical question was whether the insulation should be placed inside or outside the pressure vessel. Placing the insulation inside would maintain temperature agility since the temperature of the massive tunnel structure would not have to be changed. However, it became clear that due to the loads imposed on the maglev track by acceleration and aerodynamics, a significant structure would be required to react out the forces and moments. This structure must penetrate the insulation and would be such a heat source that the tunnel could not be adequately cooled and kept turbulence free. Therefore, it was determined that the insulating material must be placed outside the pressure vessel. It was then necessary to determine how to protect the insulating material from the sun, wind, precipitation, etc. This became more complicated by the need to remove the insulation periodically to inspect and perform maintenance on the tunnel. After costing several options, the best alternative was to enclose the tunnel within a preengineered steel-frame building (a “Butler building”).

Design

Requirements. The requirements shown in Table 6 were used for the structural design study of the HiLiFT tunnel. They are derived from the HiLiFT Requirements Document and the American Society of Mechanical Engineers (ASME) Boiler and Pressure Vessel Code.

Table 6. Table Of Tunnel Design Requirements

Parameter	Value
Tunnel core test volume (clear space)	16 ft (4.9 m) diameter, circular cross-section
Tunnel pressure vessel inside diameter	20 ft (6.1 m)
Tunnel pressure vessel test section length	2,500 ft (762 m)
Tunnel atmosphere (test medium)	Gaseous nitrogen
Tunnel minimum operating pressure	1 atm absolute/0 psig (0 MPa gauge)
Tunnel maximum operating pressure (MOP)	7.5 atm absolute/95.6 psig (0.659 MPa gauge)
Tunnel design pressure (1.17 x MOP)	112 psig (0.772 MPa gauge)
Tunnel hydrostatic test pressure (1.5 x MOP)	143 psig (0.986 MPa gauge)
Tunnel pressure vessel code requirement	Tunnel must be ASME Code Stamped pressure vessel
Tunnel atmosphere operating temperature	70 to -250 °F (21 to -157 °C)
Tunnel vessel design temperature range	100 to -320 °F (38 to -196 °C)
Geographical location of HiLiFT facility	Langley Research Center, Hampton, VA
Soil conditions, allowable bearing capacity	Less than 1,000 lb/ft ² (47.88 kPa)
Cryogenic pressure vessel design life expectancy	50 years
Cryogenic pressure vessel, thermal fatigue life	13,000 cycles, minimum
Cryogenic pressure vessel, pressurization fatigue life	26,000 cycles, minimum
Pressure vessel design fatigue life	250,000 cycles

Design Details. As shown in Figures 9a and 9b, the tunnel pressure vessel shell has an internal diameter of 20 ft (6.1 m) and a test section 2,500-ft (762-m) long. The model/cart test preparation section of the vessel is an additional 136-ft (41.4-m) long. The material chosen for the pressure vessel shell is 304/304L dual-certified stainless steel plate. The same material is used throughout the design including the support rings, stiffening frame, support cradles, angle mounting rails, and bulkhead doors. The minimum calculated shell plate thickness was 0.717 in (1.82 cm) and was rounded up to a nominal thickness of 0.750 in (1.91 cm) where the additional thickness serves as a corrosion allowance and compensates for mill plate tolerances.

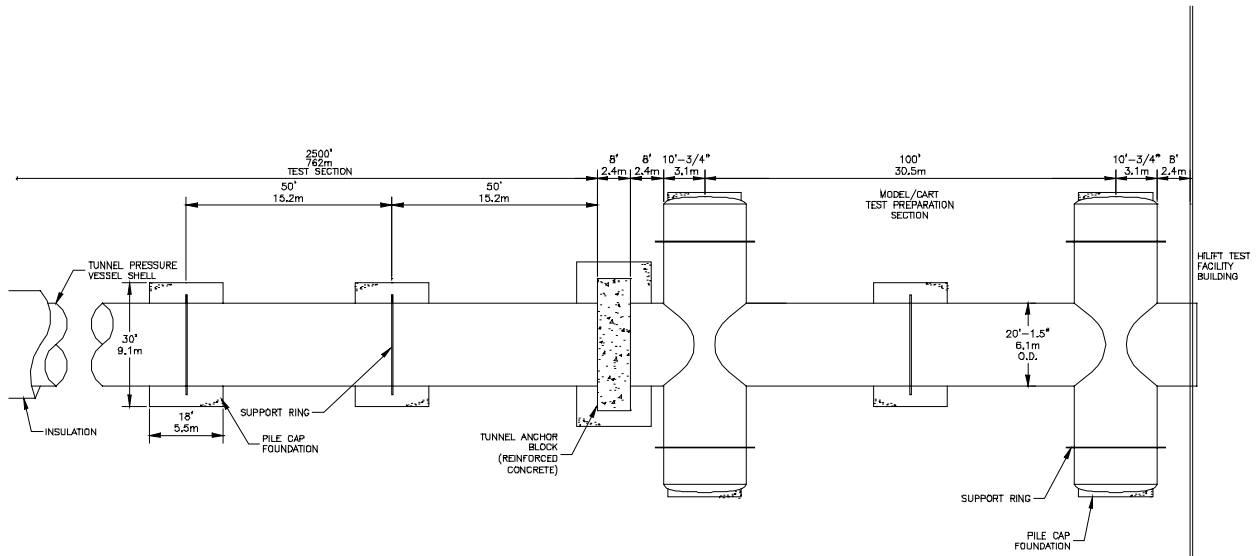


Figure 9a. Diagram of tunnel pressure vessel, plan view.

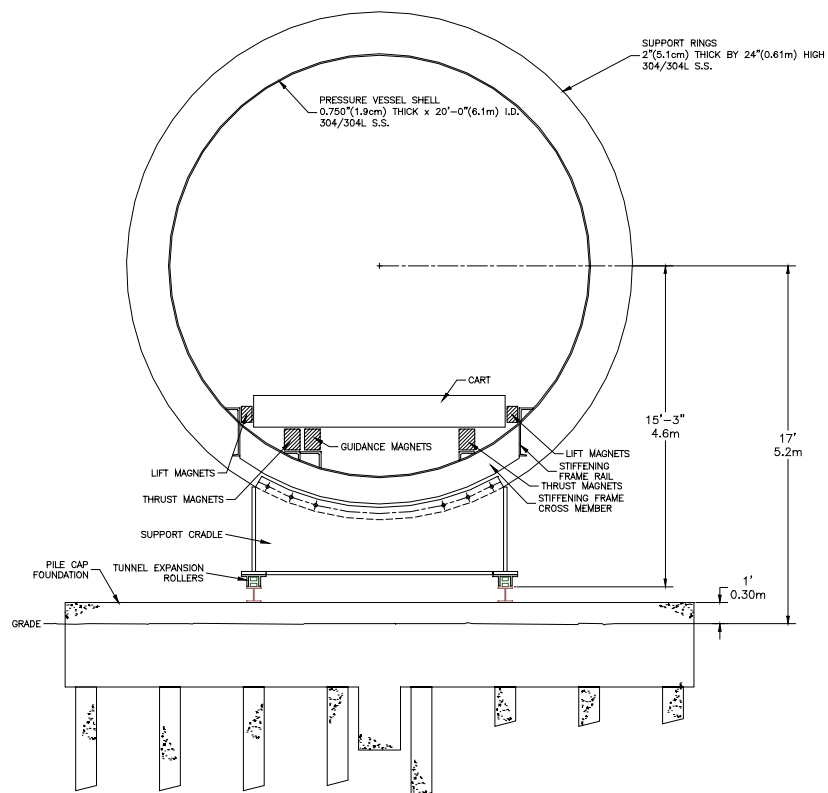


Figure 9b. Diagram of tunnel pressure vessel, elevation view.

The plates will be joined using longitudinal and circumferential butt-welded joints. In order to attain the full strength and safety of the plate, the joints will be welded inside and outside of the vessel shell. The joints will be 100% radiography inspected. The entire 2,500-ft (762-m) length of the tunnel shell will be a single welded cylinder with no expansion joints. The entire length of the vessel shell will be allowed to expand and contract longitudinally from thermal changes and pressure expansion. The pressure vessel shell underbelly is stiffened by a stiffening-frame to prevent unacceptable local bending and bowing of the pressure vessel shell caused by the weight and forces of the model cart moving through the tunnel. The entrance end of the 2,500-ft (762-m) long vessel test section will be anchored in place by the main anchor block to prevent movement. The remainder of the test section will be allowed to move on rollers. The 136-ft (41.4-m) long test preparation section of the vessel is also anchored by the main anchor block with the free end allowed to move on rollers.

The pressure vessel shell is stiffened and supported with support rings. The support rings will be welded in place on the outer circumference of the pressure vessel shell and will provide an attachment area to support the weight of the pressure vessel shell and its contents on the rolling support cradle structures located underneath. The support rings add stiffness to maintain the cylindrical shape of the pressure vessel. The support rings will be 2-in (5.08-cm) thick by 24-in (0.61-m) high and located at 50-ft (15.2-m) intervals along the length of the pressure vessel shell. There are 50 support rings along the length of the pressure vessel test section; each ring is supported on a rolling support cradle. There are five support rings on the pressure vessel cart/model test preparation section; each ring is supported by an additional rolling support cradle. Each of the 55 support rings is sandwiched between and bolted to the lateral upright flanges of its support cradle.

The support cradles are mounted on roller bearings that allow movement in the tunnel longitudinal direction from expansion and contraction of the vessel shell due to thermal changes. The roller bearings under the support cradles travel on short parallel tracks that are mounted on top of reinforced-concrete pile cap foundations. The support ring is held in place in the cradle between two vertical plates of the support cradle. The vertical plates form the sides of the support ring cradle, which create a footprint for a set of four roller bearing assemblies.

Each support cradle will have a tube welded along each side near its attachment to the tunnel-stiffening ring for thermal conditioning. Following structural assembly and installation of the tunnel insulation subsystem, polyurethane foam will be sprayed in place around each support in a manner so that it does not interfere with the operation of the roller-bearing system. A vapor barrier will be placed around the foam and sealed to the lower end of the support and the outer surface of the tunnel insulation.

The support cradle structure and the four roller bearing assemblies under each support cradle are designed with a load capacity of 600 tons ($544 \cdot 10^3$ kg). The maximum total weight on the roller bearings and the roller track during the hydrostatic test is 567 tons ($514 \cdot 10^3$ kg). In normal operation, the support cradle structure and roller bearing assemblies are required to support a maximum load of 179 tons ($162 \cdot 10^3$ kg). The maximum static load from the tunnel weight on the roller bearings is 135 tons ($122 \cdot 10^3$ kg).

The roller bearing tracks require a vertical and lateral adjustment mechanism capable of lifting and moving the entire tunnel structure to establish and maintain the pressure vessel alignment. The first support cradle will have a longitudinal movement of just over 2 in (5.08 cm), while the last support cradle at the far end of the pressure vessel will have a longitudinal movement of approximately 106 in (2.7 m).

The support cradles and roller bearing assemblies will be mounted on steel-reinforced concrete pile cap foundations. Concrete piles will support each pile cap. The top surface of the pile cap supports the I-beam rail system for the roller bearings with vertical and lateral adjustment.

The reaction rails for the maglev lift magnets, guidance magnets, and the LSM stator will attach to angle mounting rails, which will be welded to the inside bottom surface of the pressure vessel shell. There are two mounting angles for the right and left lift magnets, two mounting angles for the right and left thrust magnets, and one mounting angle for the guidance magnets.

The model/cart test preparation section of the tunnel is fitted with two pressure-tight movable bulkhead doors. These doors allow the tunnel test section operating pressure and temperature to be maintained while the cart and model are removed from the test section for maintenance or modification. The bulkhead doors and short sections of bridge rails are mounted on a carriage track running perpendicular to the tunnel centerline. The carriage track will be operated by electric motors. The outer circumference of the bulkhead doors will be pulled tightly against their sealing surface using electrically driven clamping bolts.

Insulation and Acoustic Damping. The HiLiFT tunnel will be thermally insulated and jacketed with Foamglas® (a closed-cell silica glass insulation) to minimize heat gains and attendant operating costs. The pressure vessel shell, the support rings, and the vessel-stiffening frame will be covered with thermal insulation. Six-in-thick custom manufactured curved Foamglas panels that fit the curvature of the pressure vessel are laminated together to make a composite 36 in (0.91 m) insulation layer around the tunnel. Individual panel seams are overlapped and sealed. The outside surface of the last layer will be covered with a combination aluminum jacket and vapor barrier.

Acoustic wedges (as used in anechoic chambers) will be installed on the inside surface of the pressure shell for sound wave attenuation. In testing conducted by the manufacturer, one reflection against 18-in (0.46-m) deep acoustic wedges absorbed 19.5% of the low frequency energy where the majority of the acoustic noise is expected to be generated. The acoustic wedges will be installed on approximately the upper three-quarters of the shell circumference and will extend along the entire 2,500-ft (762-m) test section.

Pressure Testing. After completion of the pressure vessel construction, it will be pressure tested by a method accepted by the ASME Boiler and Pressure Vessel Code. The code allows either hydrostatic or pneumatic testing, with the hydrostatic test being the preferred method. Accordingly, a hydrostatic pressure proof-load test will be conducted by filling the pressure vessel shell with water and then pressurizing the interior of the vessel according to the ASME code. The hydrostatic test pressure will be 143 pounds per square inch gauge (psig) (0.986 MPa gauge), which is 1.5 times the vessel's maximum allowable working pressure of 95.6 psig (0.659 MPa gauge). The HiLiFT pressure vessel, support cradles, support cradle rollers, pile cap foundations, and all calculations presented in this study assume that the pressure vessel is to be hydrostatically pressure tested.

Tunnel System Structural Analyses

Static Deflection Analysis. A static deflection analysis was performed using ANSYS®, a finite element analysis (FEA) computer-simulated engineering software package. The static deflection model represents five sections of the full-size tunnel where each of the five sections is 50-ft (15.2-m) long for a total model length of 250 ft (76.2 m).

Two different test loads were used. Test-1 loads of 88,210 lb ($40.0 \cdot 10^3$ kg) represent the weight of the cart and aircraft model, as well as the maximum negative lift force from the aircraft model as specified in the design requirements document. Test-2 loads of 42,965 lb ($19.5 \cdot 10^3$ kg) represent the weight of the cart and aircraft model, as well as a more nominal negative lift force from the aircraft model. Both loads were applied as a distributed load midspan between support rings on the tunnel shell as shown in Figure 10 (internal nitrogen pressure was neglected for these analyses).

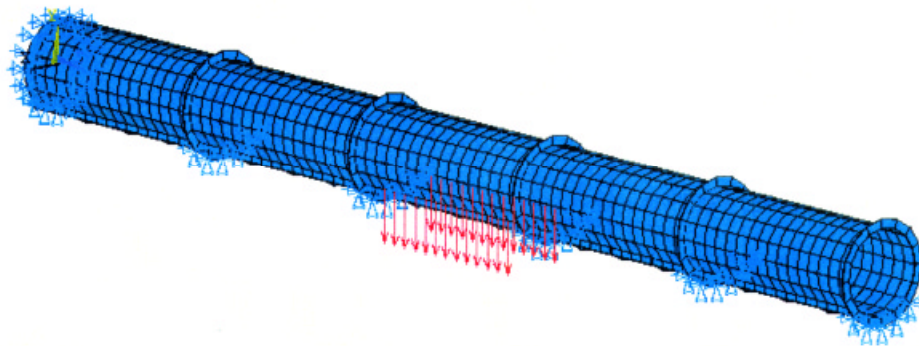


Figure 10. Distributed load midspan between support rings on the tunnel shell.

The maximum stress on the tunnel model from the Test-1 loads was 3,612 pounds per square inch (psi) (24.9 MPa), as shown in Figure 11. The maximum stress on the tunnel model from the Test-2 loads was 1,760 psi (12.1 MPa) with the same pattern as in Test-1. Both of these are versus a material maximum allowable stress of 18,800 psi (130 MPa) per the ASME Broiler and Pressure Vessel Code.

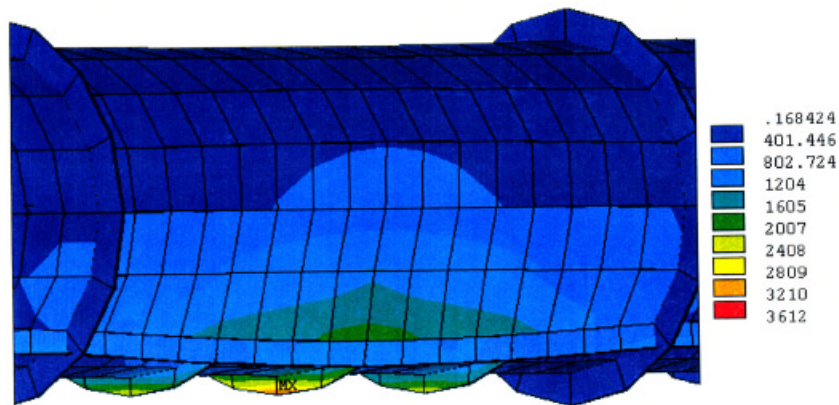


Figure 11. Maximum stress on the tunnel model from Test-1 loads.

The maximum deflection from the loads in Test-1 was 0.057 in [1.45 millimeters (mm)], as shown in Figure 12. The maximum deflection from the loads in Test-2 was 0.029 in (0.74 mm) and followed the same pattern as Test-1.

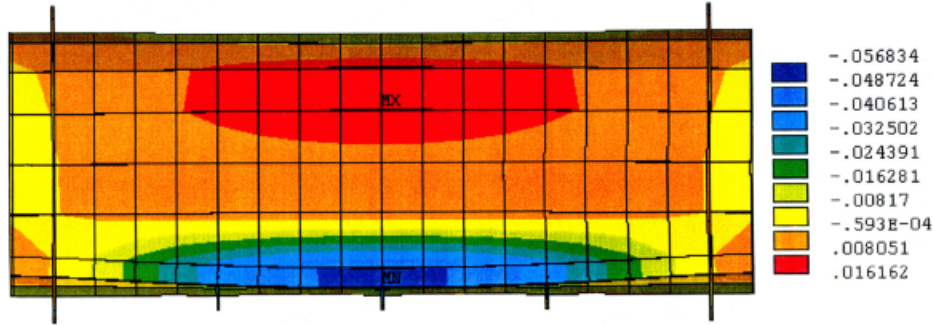


Figure 12. Maximum deflection from loads on the test model.

Dynamic Analysis. Modal analysis is used to determine the vibration characteristics including natural frequencies and mode shapes of a structure. The natural frequencies and mode shapes are important parameters in the design of a structure for dynamic loading conditions. There are no loads or forces applied to the model for the modal analysis.

A modal analysis was completed for the HiLiFT structure using ANSYS®. This model is the same model used for the harmonic response analysis.

The modal analysis calculated all of the peak frequencies seen on the harmonic response graph plus hundreds more. Sixteen of the frequencies and a brief description of the mode shapes are presented in Table 7.

Table 7. Tunnel Modal Frequencies And Mode Shapes

Number	Frequency	Direction	Description
1	2.98 Hz	Z	Longitudinal movement, upper half of vessel, flexing of support rings.
2	5.23 Hz	Z	Longitudinal movement, upper half of vessel, flexing of support rings.
3	7.97 Hz	X	Lateral movement, upper half of vessel.
4	8.01 Hz	Z	Longitudinal movement, upper half of vessel.
5	8.07 Hz	X	Lateral movement, upper half of vessel.
6	8.26 Hz	X	Lateral movement, upper half of vessel.
7	8.53 Hz	X	Lateral movement, upper half of vessel.
8	8.87 Hz	X	Lateral movement, upper half of vessel.
9	9.28 Hz	X	Lateral movement, upper half of vessel; small lower shell wave.
10	9.29 Hz	X, Y	Sinusoidal shell wave, little support ring movement.
11	12.00 Hz	Y	Sinusoidal shell wave, lower shell wave, little support ring movement. Dominant peak frequency on harmonic response graph.
12	14.00 Hz	Y	Sinusoidal shell wave, lower shell wave, little support ring movement. Dominant peak frequency on harmonic response graph.
13	19.98 Hz	Y	Sinusoidal shell wave, lower shell wave, little support ring movement.
14	21.98 Hz	Y	Sinusoidal shell wave, lower shell wave, little support ring movement.
15	24.99 Hz	Y	Sinusoidal shell wave, 1st section affected only
16	26.35 Hz	Y, Z	Sinusoidal shell wave, little shell wave. Sinusoidal support ring wave, elephant ear action of support rings.

Note: X direction = side-to-side, Y direction = vertical, Z direction = longitudinal

A copy of the ANSYS output for mode numbers 1, 7, and 10 is shown in Figures 13, 14, and 15, respectively.

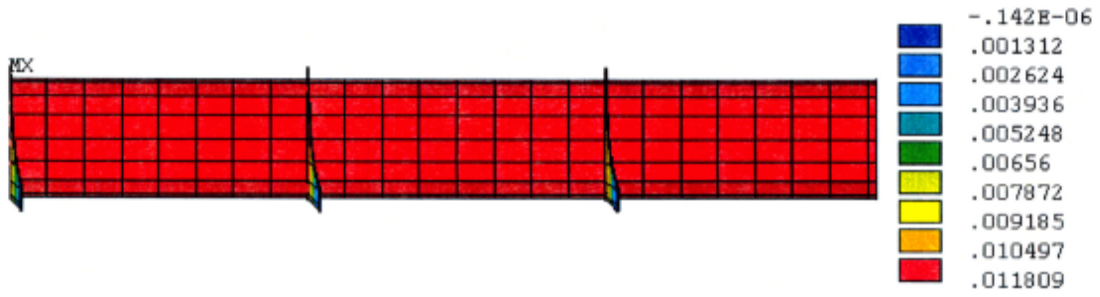


Figure 13. ANSYS output for Mode 1.

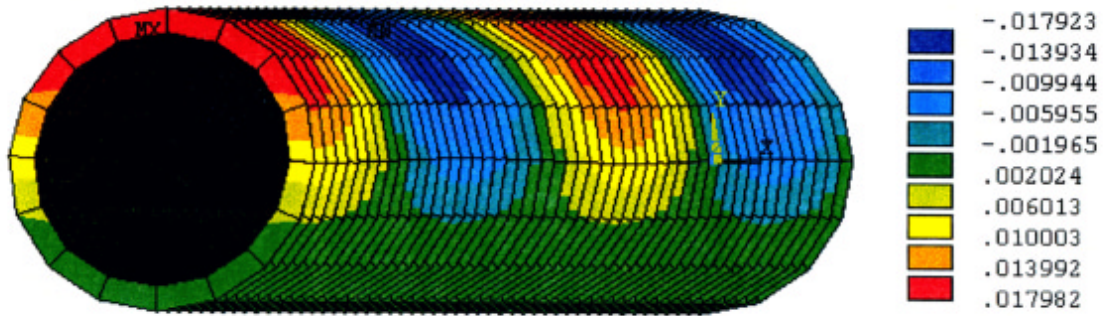


Figure 14. ANSYS output for Mode 7.

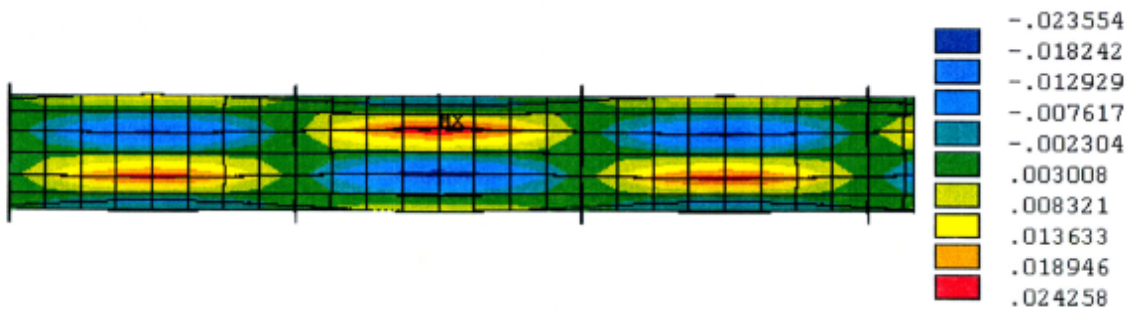


Figure 15. ANSYS output for Mode 10.

Cart and Sting System Design and Analyses

Requirements

The key requirements for the HiLiFT cart are summarized in Table 8.

Table 8. Cart And Sting Design Requirements

Parameter	Value
Model angle-of-attack range	+20 to -10 degrees referenced from horizontal plane
Model yaw range	+16 to -16 degrees referenced from vertical plane
Model roll range	± 180 degrees from tunnel longitudinal axis
Model loads	see Table 4
Model center of pressure	Within ± 2 in (5.1 cm) of the center of the core test volume
Model support structures dynamic design criteria	A. Designed for a dynamic load range of $\pm 25\%$ of the maximum combined static loads B. Designed for an impulse loading of 50% of the maximum combined static loads

Material Selection

Calculated cart weights indicate a cart made primarily of AS-4 graphite/epoxy composites is less than 60% the weight of a cart fabricated entirely of steel at 25,200 lb (11,431 kg) vs. 39,500 lb (17,917 kg) and approximately the same weight of a cart fabricated primarily of titanium at 27,780 lb (12,601 kg). These numbers assume the metal cart components are thinner than composite members, since they have a higher elastic modulus and mechanical strength. The allowable stress for low-end composites is on the order of 40,000 psi (276 MPa), while for American Society for Testing and Materials (ASTM) A286 steel, it is approximately 78,000 psi (538 MPa). The net effect of the extra weight is twofold. First, it requires more power to accelerate the cart. The extra cart mass also requires larger magnets, batteries, and power conductors. Second, the additional mass drives the modal frequencies lower, meaning the cart and associated structures will vibrate with lower driving frequencies, which is undesirable, as discussed in *Model Analysis* section.

Design Characteristics

The baseline cart/model support system consists of a deck structure to house the suspension and propulsion magnets and an adjustable boom assembly to support the model/balance subassembly. The entire structure is constructed of graphite/epoxy composite except for bearings and metallic positioning mechanisms, end fittings for composite members, fairing plates, and fasteners. The deck is fabricated from 18-in (45.7-cm) by 9-in (22.9-cm) by 0.5-in (1.3-cm)-thick members connected by welded A286 steel fittings with bolted fasteners. Plan and elevation views of the model and cart are shown in Figures 16 and 17.

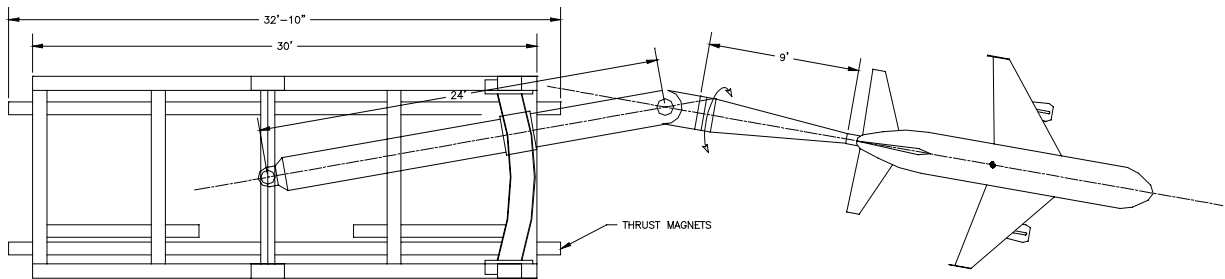


Figure 16. Cart and model plan view.

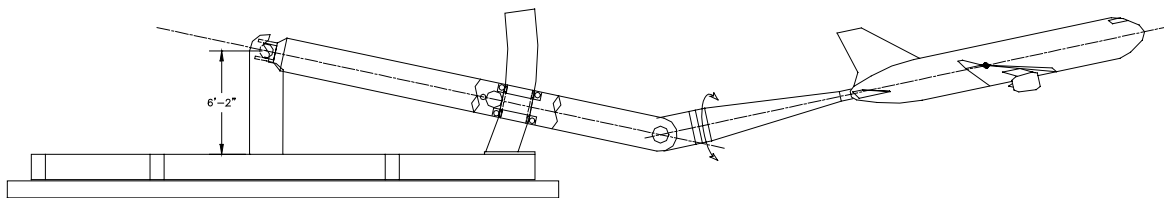


Figure 17. Cart and model elevation view.

Vertical structural supports for the main boom and positioning hardware are also 18 in (45.7 cm) by 9 in (22.9 cm) by 0.5 in (1.3 cm) graphite/epoxy composite. The aft supports and rear shaft form a structural pseudo-bent to which the aft boom is attached. Teflon bearings [12 in (30.5 cm) inner diameter (ID)] support the boom rear yoke and rear shaft at their respective attachment points. The forward vertical supports and the yaw traverse support are arcs with a 16-ft (4.9-m) center of curvature. This ensures free movement without any axial relative motion between the boom and traverse.

The onboard batteries are mounted inside the deck to power lift magnets, instrumentation, positioning mechanisms and other cart accessories during test runs. The dimensions of each of the two battery banks, fore and aft, is 10 ft (3.0 m) by 5 ft (1.5 m) by 1-ft (0.3 m). These batteries are kept warm in insulated and heated enclosures fabricated from stainless steel/polyurethane foam sandwich material.

The boom assembly serves to position the model/balance. It is supported by tandem pitch positioners actuated by electric ball screws, as well as a yaw positioner that is also actuated by an electric ball screw. The ball screws are mounted on gimbals at both ends, so they are only loaded in the axial direction. Other loads are borne by positioner carriages on each vertical support and the yaw traverse.

The main boom is a hollow 24-in (61.0 cm) diameter, 3-in (7.6 cm) wall, graphite/epoxy composite member that bears all the loads transmitted to it from the balance and sting. It is wound from the same materials as the other structural members; the main differences are its larger size and greater wall thickness. This member houses the instrument cables for model data and power wiring for the roll mechanisms mounted at its end.

A “knuckle” and two roll mechanisms are mounted at the forward end of the boom. The knuckle is a simple hinge consisting of an outer yoke attached to the aft piece of the boom and a 12-in (30.5 cm) steel pivot pin mounted to the forward piece of the boom. The pivot pin rotates in two 12-in (30.5 cm) Teflon bearings mounted in the outer yoke. Since the knuckle can only move in one plane, the first roll mechanism keeps the knuckle plane congruent with the plane defined by the tunnel centerline and the center of the knuckle. Model position is adjusted by simultaneously moving the center boom pitch and yaw positioners, knuckle, and first roll mechanism for the desired pitch/yaw combination. The second roll mechanism establishes the desired model roll. All actuator mechanisms are enclosed in structural members; therefore, they can be insulated and heated for reliable operation. Antibacklash gearing, preloaded bearings, and close manufacturing tolerances will be specified for all commercial items to minimize free play in the model positioning system. Fairing shapes are applied to the knuckle and to the leading and trailing edges of major structural members for a more streamlined cart.

Structural Analyses

Static Deflection Analysis. Static analysis is used to examine the response of a structure when the time-dependent effects of inertia and damping are not significant components of that response. The HiLiFT project used static analysis to estimate the steady-state deflections of the cart due to applied lift, drag, and yaw loads. Static end-of-boom deflections for baseline model loads are summarized in Table 9.

It can be seen from the data that the static deflections are generally not within the required tolerances of 2 in. The boom thickness used in this analysis was 3 in (7.6 cm) for the 24-in (61-cm)-diameter boom. The 24-in (61-cm)-diameter boom was chosen to minimize the effects on aerodynamic performance. This will require the boom angle to be placed in an offset position in anticipation of deflections. The model attitude will change during the acceleration and deceleration phases of each run but will be within the required ± 2 in (5.1 cm) during the data collection portion of the run.

Table 9. Summary of Static Deflections—Baseline Case.

Load/geometry case	Model deflection	Maximum stress
<u>High lift</u> Cart E=17,000,000 psi (117,000 MPa) Boom E=17,000,000 psi (117,000 MPa) Sting E=30,000,000 psi (207,000 MPa) Sting Dia=12.5 in (31.8 cm) Boom Dia=24 in (61.0 cm)	8.3 in (21.1 cm) upward 0.08 in (0.20 cm) sideways	Sting: 34,042 psi (235 MPa) Boom: 18,107 psi 125 MPa) Traverse: 29,817 psi (206 MPa) Front Support: 13,089 psi (90 MPa)
<u>High side force</u> Cart E=17,000,000 psi (117,000 MPa) Boom E=17,000,000 psi (117,000 MPa) Sting E=30,000,000 psi (207,000 MPa) Sting Dia=12.5 in (31.8 cm) Boom Dia=24 in (61.0 cm)	4.45 in upward (11.3 cm) 0.34 in sideways (0.86 cm)	Sting: 21,483 psi (148 MPa) Boom: 11,477 psi (79 MPa) Traverse: 16,633 psi (115 MPa) Front Support: 6,334 psi (44 MPa)

A 12.5-in (31.8-cm)- diameter composite sting with a 3.5-in (8.9-cm) wall was chosen. This size is as large as will fit in the tail of a large transport model; however, even this size sting has calculated stresses slightly over the allowable 40,000 psi (276 MPa) for the high lift load case. Smaller models will require a smaller sting; a suite of stings will most likely be required to accommodate all models anticipated.

The balance used in this analysis is a stainless steel unit with a maximum diameter of 6.5 in (16.5 cm). The second area moment for this shape is estimated to be between 45 and 87 in⁴ (1,870 and 3,620 cm⁴). Even at the maximum second moment, the calculated stress is approximately 74,000 psi (510 MPa)—beyond the material ultimate strength of approximately 70,000 psi (483 MPa). Accordingly, the cart will require a larger balance to accommodate the high lift case.

Transient Dynamic Analysis. A sinusoidal vertical displacement of 1 mm (0.039 in) was imposed on the model cart to simulate the effect of tunnel deflection between the pressure vessel stiffening rings. At Mach 0.3, the period of oscillation for this deflection is approximately 0.23 seconds, or 4.3 hertz (Hz). The model response indicates a pronounced resonant amplification of this driving function in the vertical direction at approximately 4.5 Hz. This amplification results in model position errors greater than allowables and must be analyzed in greater detail during future studies.

The peak high lift case loads were increased by 25% to accommodate general *dynamic loading*; the model was then statically analyzed. The results show the peak y-coordinate (upward) model deflection is 8.64 in (21.0 cm), 0.84 in (2.1 cm) (10%) more than the steady-state deflection of 7.8 in (19.8 cm).

Impulse loading response was examined by loading the end of the balance to 100% and then imposing a lifting force ramp function from 100% to 150% of static values over 1 second. These conditions were maintained for 1 second; the lifting force was then ramped back down to 100% over 1 second. This analysis was performed to determine the effects of sudden overload. The results indicate flutter in the steady-state portion of the ramped load at approximately 4.5 Hz. The induced boom stresses under these conditions are below 30,000 psi (207 MPa), which is acceptable.

The cart's responses to the 8 Hz driving function from the *linear synchronous motor (LSM)* were examined by applying a 1 mm amplitude wave at the base of the cart where the motors are located. The responses were as follows:

- Applied axially, the model's axial response occurred at approximately 14 Hz, slightly amplified. The transverse responses were at approximately 5 Hz, not amplified.
- Applied vertically, the driving function yielded a vertical response at approximately 6 Hz, not amplified. The axial and sideways responses were approximately 8 Hz and 5 Hz, respectively, also not amplified.
- Applied sideways, the driving function produced an axial model response at approximately 4.5 Hz, amplified, a vertical response at approximately 5 Hz also amplified, and a sideways response at approximately 4 Hz slightly amplified.

Modal Analyses. Modal analysis is useful for any application in which the natural frequencies of a structure are of interest. In this case, the natural frequencies of interest are those below 25 Hz. Frequencies between 0 and 25 Hz have been the range of driving frequencies in wind tunnel operations. By avoiding such natural frequencies, the catastrophic results of resonant amplification of the driving frequencies can be avoided.

Modal analysis is used to extract the natural frequencies and mode shapes of a structure. This is an important first step in many types of dynamic analysis because knowledge of the structure's fundamental mode shapes can help characterize its dynamic response.

The cart model for modal analysis is a structure composed of elastic beams and three-dimensional masses. For the cart, model, sting, and balance [24-in (61-cm) boom case], the first 10 modal frequencies and descriptions are summarized in Table 10. Examples of the visualization of mode shapes generated by the analysis software are given for Mode 5 in Figure 18 and Mode 8 in Figure 19.

Table 10. Modal Analysis Summary

#	Mode description	Frequency
1	Up/down bending, entire cart	4.69 Hz
2	Side/side bending, boom and supports	5.43 Hz
3	Fore/aft boom motion	7.92 Hz
4	Side/side bending, supports	8.23 Hz
5	Twisting, front boom supports	13.16 Hz
6	Fore/aft boom motion, transverse deck bending	15.80 Hz
7	Deck twisting amidships	20.25 Hz
8	Aft deck bending	22.56 Hz
9	Deck stringers side/side waves	24.09 Hz
10	Deck twist	32.18 Hz

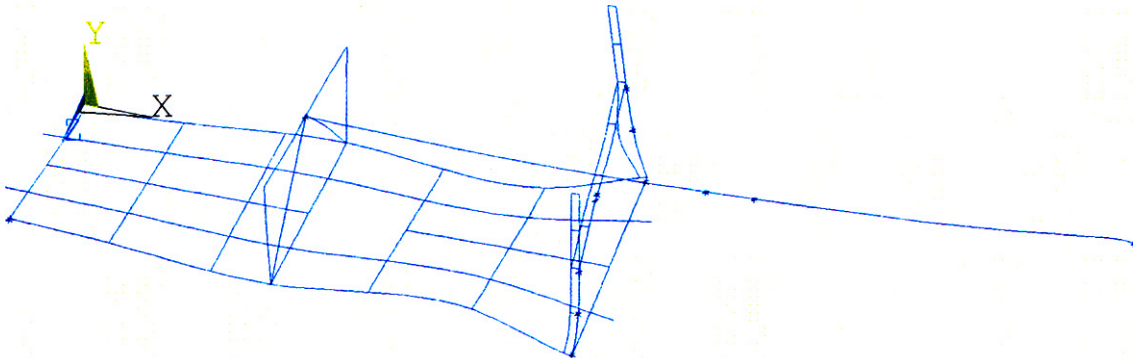


Figure 18. Visualization of mode shape for Mode 5.

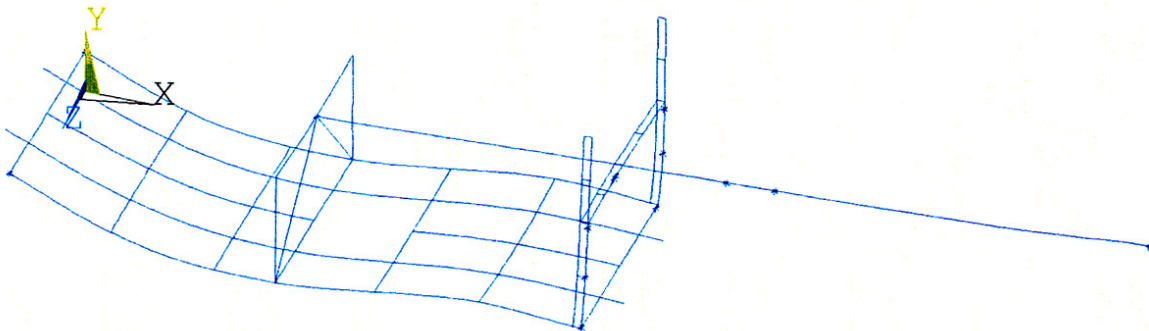


Figure 19. Visualization of mode shape for Mode 8.

Pedestal Mounted Model (Bipod Model Support)

The low resonant frequencies of the chosen model mounting method, combined with the high stresses on the sting, led to the consideration of another type of mounting. The most promising was the bipod mount, as shown in Figure 20 that is installed in the NASA Ames Research Center (NASA-Ames) 12 ft (3.7 m) pressure wind tunnel.

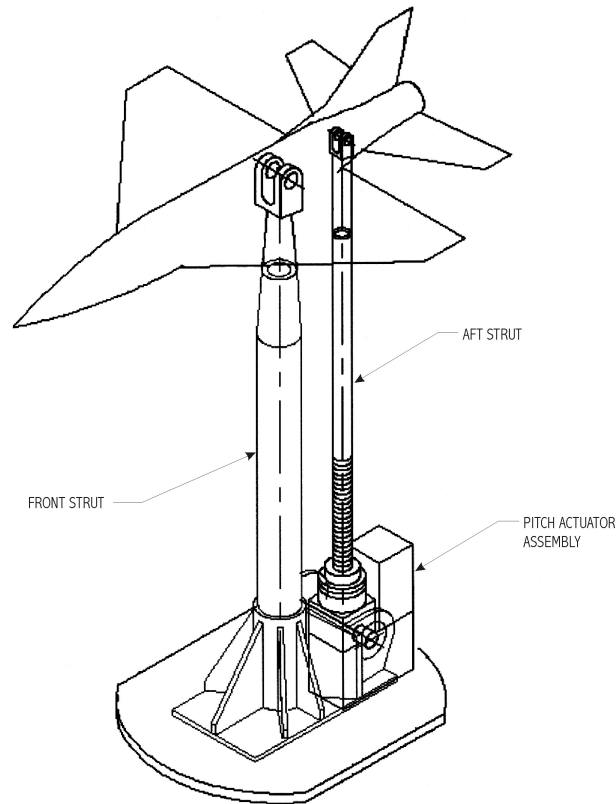


Figure 20. Bipod mount of the NASA-Ames 12-ft (3.7 m) pressure wind tunnel.

The bipod model support (BMS) consists of a static main post and articulating rear strut. The rear strut consists of a roller screw, driven by an electric motor, and a harmonic drive gear reduction. The rear strut controls the pitch of the model, and a turntable mounted on the base controls the yaw of the model. The balance would be external to the model, i.e., between the cart and the model supports.

In general, the BMS offers less stress on the structural members and higher modal and resonant frequencies. However, its drawbacks include: 1) more aerodynamic interference on the model and 2) requires a new external balance designed to withstand the loads imposed at the temperatures and pressures in the tunnel.

The BMS design is being strongly considered for adoption in the next design iteration.

Maglev System

System Options and Selection

A wide variety of technical options spanning a range of magnetic levitation, propulsion, and guidance options, and system configurations were examined (Refs. 2 and 3). The four main candidates identified were:

- An iron-core LIM using either single- or double-sided magnets with an attractive-force suspension system;
- An iron-core LSM used in combination with an attractive-force suspension system (the EMS option);
- An air-core LSM used in combination with a null-flex repulsive-force suspension system using superconducting magnet technology (the EDS option); or
- A permanent magnet, repulsive force system.

The LIM option was discarded for a variety of technical reasons including poor speed control and power factor (less efficient operation) leading to increased tunnel heating. The permanent magnet option was added late in the selection process but was discarded since it is not fully developed and there were too many developmental risks. Therefore, the choice was between the EMS and the EDS options.

In this design, the greatest emphasis was placed on the more practical issues such as minimizing technical risk and satisfying the stringent magnet position control requirements. The EMS system had the advantage since it required magnet air gap control for normal operation. Therefore, the need to meet specific HiLiFT project control requirements was more of a refinement step than the development of a new technology. The EDS system does not normally require control of the magnets to maintain the air gap clearances, and therefore, to meet specific control requirements meant developing a new control technology for superconducting magnets.

However, the EDS option is being kept as an alternative in the event the EMS option proves unworkable. Among the technical challenges associated with the EMS options was that until recently the technology had been developed for a large lifting force and small axial acceleration. This is the opposite of the requirements for HiLiFT, although it became clear later in the project that a high lifting force would also be required to balance very large applied moments.

System Description

Separate magnets were designed for use as lift, guidance, and thrust magnets. A total of two thrust magnets were required, along with two guidance and four lift magnets, as shown in Figure 21.

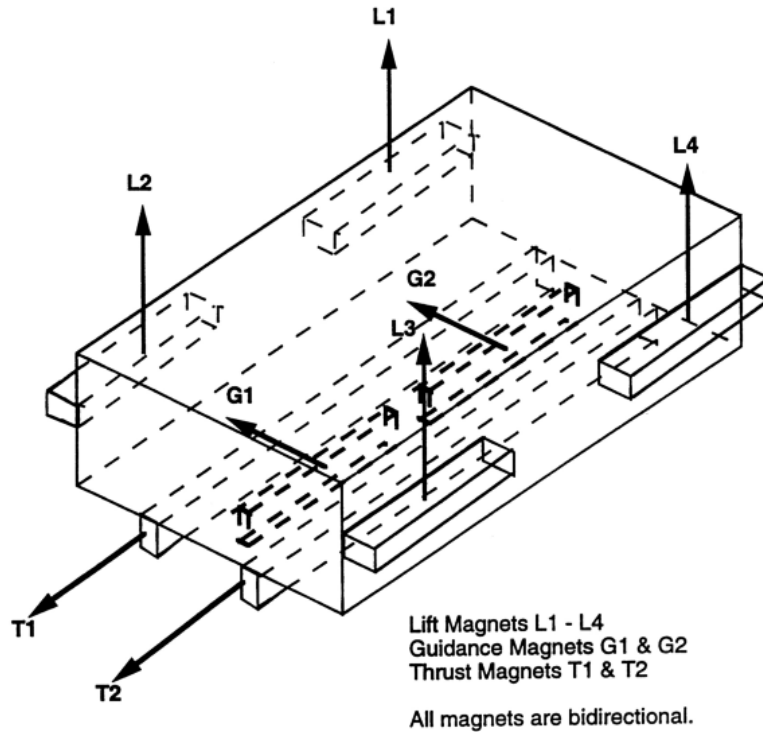


Figure 21. Cart magnet placement.

Thrust. The thrust motors are LSMs and are used to accelerate and decelerate the cart. The thrust magnets are along the bottom of the cart, on either side of the centerline. Each magnet is 32.5-ft (9.92-m) long, 1.2-ft (0.36-m) wide, and 3.15-in (0.08-m) thick. The LSM stators are mounted along the length of the tunnel and are divided into 164-ft (50-m) section lengths. The thrust motors are double sided and are driven with a three-phase power supply capable of variable voltage and frequency operation. Energizing the three-phase winding gives rise to alternating north and south magnetic poles that travel smoothly in the direction of cart travel and pull/push on the mating poles of the cart thrust magnets. In the braking mode, the LSM becomes a generator with the power generated being dissipated in a resistor bank.

A 12.5 kilovolt (kV), 3.4 kiloampere (kA), three-phase utility connection is required for each of two power supplies to supply sufficient power for peak accelerations. Each LSM power supply will be a two-stage power converter consisting of a phase-controlled rectifier feeding a variable frequency, variable voltage inverter, via a dc link. The dc link/inverter combination is called a voltage source inverter and is commonly used in large motor drives and electric locomotives. This is shown schematically in Figure 22.

The entire LSM cannot be placed on line at the converter output because the leakage reactance of the LSM would then be so large that an enormous stator power supply voltage would be required. For this reason, it is sectionalized or divided into 164-ft (50-m) sections. Only the section under the HiLiFT cart must be energized to provide propulsion force. Sections are switched onto the power supply as needed. Since switching from one LSM section to the next as the cart moves cannot be done instantaneously, two LSM sections are always energized during a run from separate power supplies. One section (i.e., the “active” section) is under the cart and provides propulsion power for the cart. The section just ahead of the “active” section (i.e., the “ready” section) must be energized so that when the cart reaches it, LSM

operation will continue smoothly. When a “ready” section becomes the new “active” section by way of cart travel, the old “active” section is switched off, and the section ahead of the present “active” section is energized to make it the new “ready” section. The old and new ready sections leapfrog the cart to provide continuity of LSM operation.

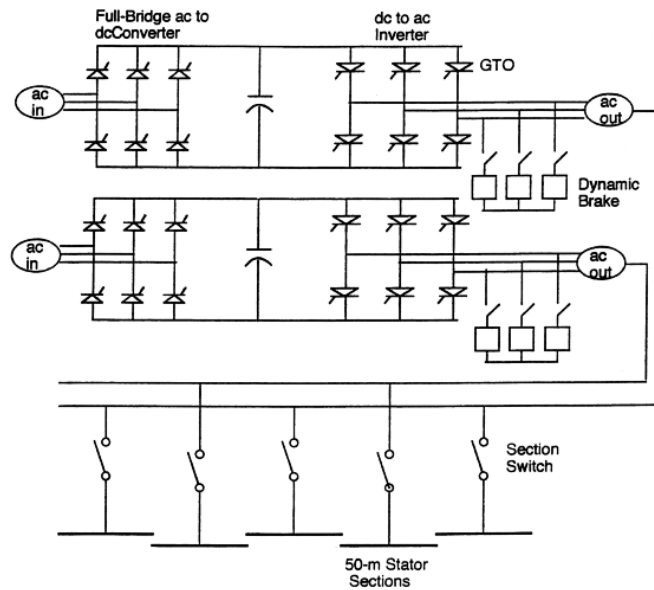


Figure 22. Power circuit and sectionalizing.

Under normal operations, dynamic braking will be used to bring the cart to rest. For this, the power source is disconnected from the stator, and the stator terminals are connected to resistor banks to dissipate the energy. To provide control of the braking rate, the resistor banks can be connected to the dc bus inside the power converter.

An analysis was performed on the amount of “swing” expected in the LSM. The term “swing” originates from rotary synchronous motor design, where it refers to cyclical perturbations around the synchronous frequency. The physical source of these perturbations is the lightly damped “spring” consisting of the two magnetic fields pulling on each other. “Swing” for a LSM shows up as small perturbations around the linear velocity. Analysis showed that the swing was so lightly damped that large oscillations could build up and affect the data accuracy of the aerodynamic measurements, see Figure 23. Fortunately, using feedback through the LSM controllers was quite effective in adding significant damping so that the oscillations will not build up, as shown in Figure 24.

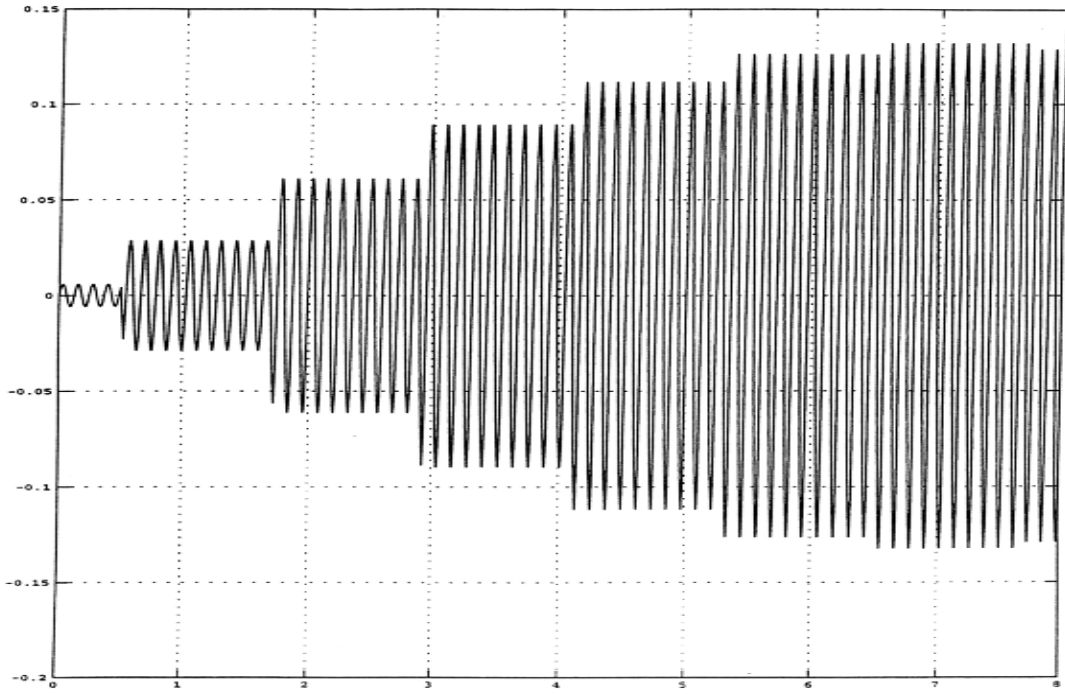


Figure 23. Effect of a sequence of -8kN pulses of period 1.2 s and width 0.02 s on the oscillations of the relative velocity. The sequence is started at 0.5 s.

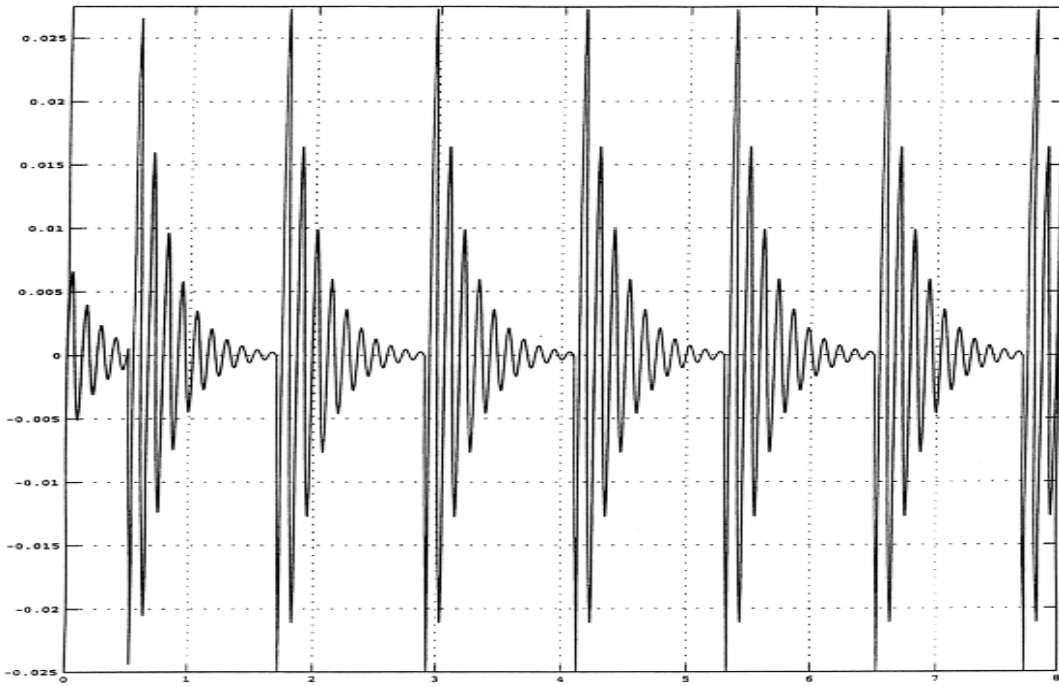


Figure 24. Feedback control gain=1,000 V/m/s. Impact on response to the same sequence of pulses used in Figure 23.

Lift and Guidance. The lift and guidance magnets are of the same basic design and operation except that the lift magnets must be energized at all times the cart is moving to counteract gravity as well as vertical disturbances, while the guidance magnets only counteract horizontal disturbances. The lift and guidance magnets are a double gap design, where only one gap is energized at a time. This allows bidirectional control with a single magnet set. There are a total of four lift magnets arranged along the sides of the cart at the four corners. There are also two guidance magnets underneath and along the length of the cart that are slightly offset from the centerline. The reaction rails are attached to the tunnel. Each lift and guidance magnet is 16.4-ft (5-m) long, 3.94-in (0.1-m) wide, and 3.15-in (0.08-m) thick. See Figure 25 for a sketch of the proposed LGM.

The electric power required on the cart will be provided by batteries. This power is used for LSM thrust magnets, lift and guidance magnets, heating electronics and battery compartments, and running control and communications electronics. Analysis showed that the most important battery parameter is specific power (power per unit weight) due to the large power demands during the short acceleration/ decelerations runs. The specific energy (energy per unit weight) of the batteries determines the number of runs that can be made before recharging. The maximum power demand (for less than a second) is expected to be just over 3 megawatts (MW). To supply this power, lithium ion batteries weighing approximately 5,573 lb (2,528 kg) and occupying approximately 100 cubic feet (ft³) [2.83 cubic meters (m³)] were selected. Each cart magnet would have its own controller and feedback sensors. The power conditioning and instrumentation systems are expected to occupy approximately 33 ft³ (0.934 m³) and 1 ft³ (0.0283 m³) of space, respectively. The batteries must be kept in a temperature-controlled compartment to protect them from freezing and to maximize the system performance. The electrolytes are in gel form and will not be affected by the high accelerations experienced.

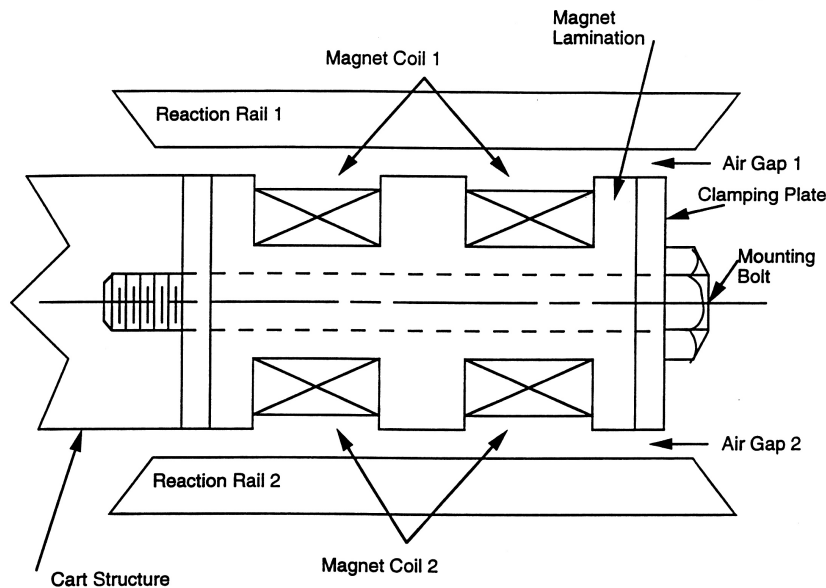


Figure 25. Lift/guidance magnet (laminations parallel to plane of page).

Emergency Braking. Under emergency conditions (e.g., the loss of a stator or dynamic braking circuit), an alternate braking scheme must be used. There are several options including both electrical and mechanical braking schemes. An electrical eddy current brake might operate as a suspended conducting plate as it passed between permanent magnets at the end of the tunnel; this would involve high deceleration forces. Another alternative would be to place a wire coil so that it passes through the permanent magnets. The coil would be open-circuited and have no effect under normal operations but would default to a fail-safe closed position if any anomalies are detected.

Thermal Considerations. The maglev system will generate significant heat that must be removed from inside the tunnel by injection of cryogenic nitrogen. Heat is generated by the stator, thrust magnets, and lift and guidance magnets. Some of the thermal input will be distributed along the tunnel; the rest will be deposited at the cart parking location between runs. The maglev system design calls for the maximum temperature rise of 45 °F [25 Kelvin (K)]. Most temperature rises will be less than this. For example, assuming no heat transfer out of the first stator section until the cart is past, the maximum temperature rise would be 0.322 °F (0.179 K). The performance of the system will be derated for operation at ambient temperature to limit the temperature rise in the cart components. The temperature rise will be greater at ambient temperature because the copper windings will be more resistive (less efficient) at warmer temperatures.

Control Systems

The magnet control system performs the following functions:

- Maintains the air gaps to a predetermined tolerance – this prevents the magnet surfaces from coming into contact with the guideway surfaces and maintains the required limits on cart orientation.
- Adjusts the magnet currents (forces) to compensate for changes in load as a function of time.

These two functions are closely related, since preservation of the air gap requires making adjustments in the magnet current to compensate for changes in applied or disturbance forces. In addition to compensating for applied or disturbance forces, the control system must also make adjustments to compensate for any irregularities in the critical guideway surfaces caused by static or dynamic loads or temperature changes.

The overall design philosophy adopted for this work involved two independent approaches. In the first approach, it was assumed that precise control of the air gaps of each individual magnet was sufficient to control the entire cart orientation. That is, the maintenance of each air gap could be conducted without adversely affecting the control of the other air gaps. On this basis, the allowed changes in attitude, yaw, and roll could be precisely determined in terms of the tolerances on the variation of each air gap. For example, by maintaining the vertical air gaps at each corner of the cart within certain tolerances, its attitude and roll could be maintained within the corresponding tolerances. A sample control system is shown in Figure 26 with a sample output shown in Figure 27. A critical assumption of this approach is that the adjustments called for by the control system would not exceed the capacities of the magnets and their power supplies.

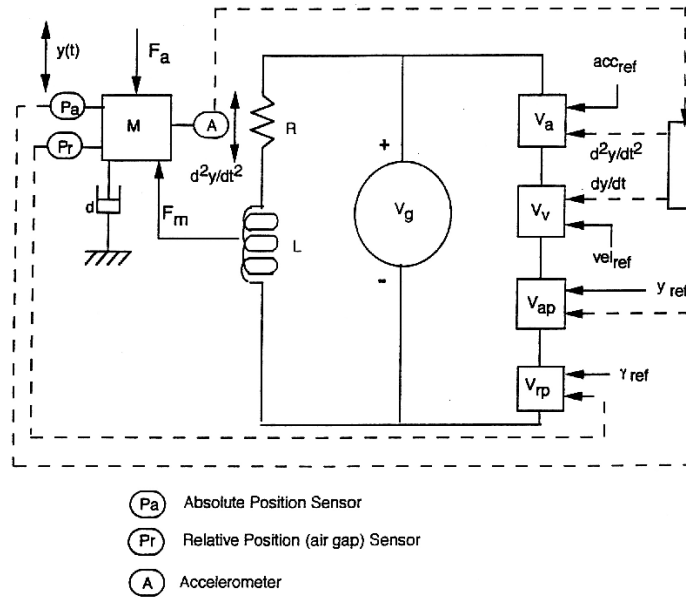


Figure 26. Magnet control system.

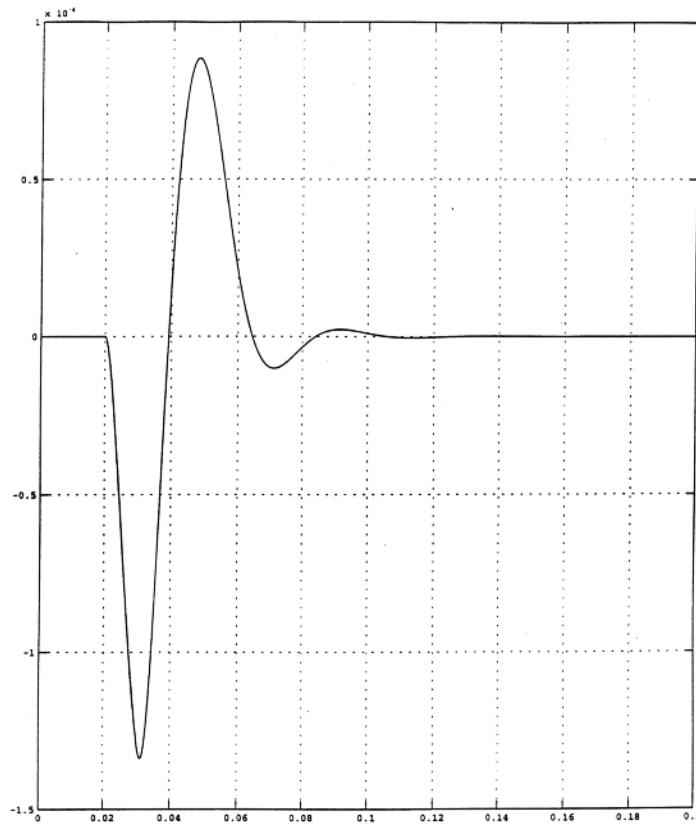


Figure 27. Response of the air gap to the input impulse to $\Delta f_a(t)$. The impulse is started at 0.02 s, its amplitude is 20 kN, and its width is 0.01 s.

In the second approach, i.e., the force/torque balance approach, it was assumed that the forces required to balance any combination of applied forces and torques could be generated by the appropriate selection of magnet forces, recognizing that each magnet on the cart could produce forces in only two complimentary directions (up/down, fore/aft, left/right, etc.). In order to correctly apply this approach, it is necessary to devise an algorithm that apportions the required forces to the optimal subset of magnets. For example, if the applied forces result in a pitching moment on the cart, only the fore and aft lift magnets should be required to balance that moment. The apportionment algorithm used also minimizes the sum of the squares of the ratios of the force required by each magnet to the capacity of that magnet. This apportionment method distributes the burden to the relevant magnets as uniformly as possible without overstressing any particular magnet while minimizing I^2R energy losses. The force/torque balance approach does not involve system dynamics (i.e., no response time is built in, but it provides a means of determining if the masses, capacities, and energy losses of all the magnets are consistent with the expected loads). It assumes that some means exists to control each magnet so that it produces the precise force that is required for the force and torque balance. This approach also provides a convenient way to generate the forces and heat inputs needed in the system simulation model.

The system simulation model simulates system kinematics and was constructed using MATLAB® with the Simulink® toolbox. A block diagram of this model is shown in Figure 28. It was used to produce several important pieces of information for the overall system design including the temperature profiles of the magnet windings, the power input profiles to the cart and stator windings, the energy loss profiles, and the heat input to the tunnel as a function of time and position. It does not simulate system dynamics, which would require incorporation of the individual air gap control model; there was insufficient time and resources to complete these in this feasibility study.

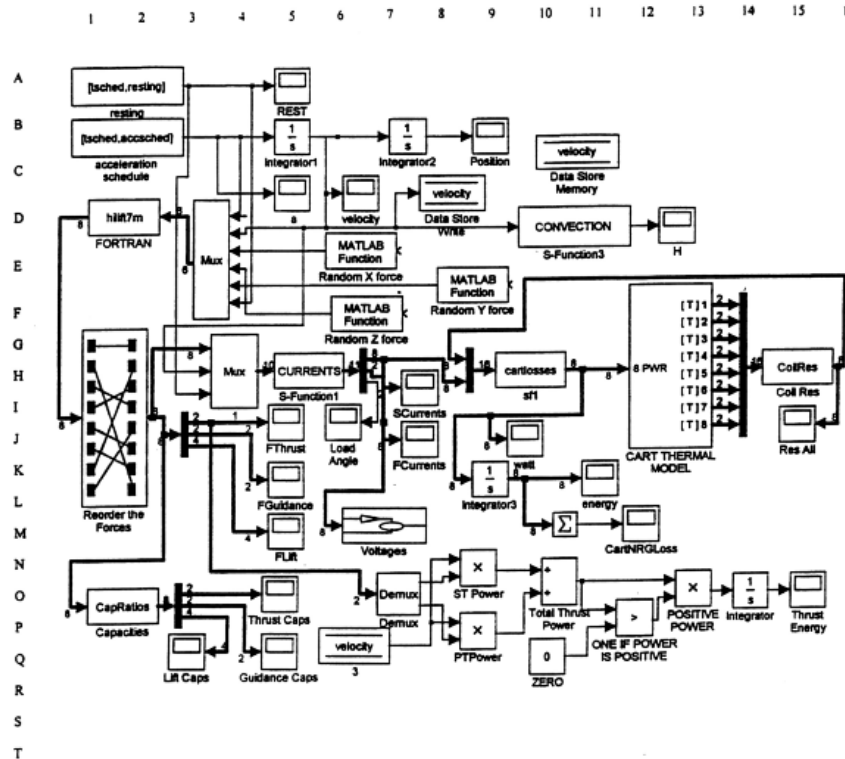


Figure 28. Tunnel run simulation block diagram.

Aerodynamic Analyses

Influence of the Cart and Model Support System

The cart and model support system induce unwanted disturbances on the model. In order to minimize this effect, the model support system must be carefully designed, and the model must be separated from the cart by an appreciable distance. This section summarizes the aerodynamic analysis and results that were used to guide the model support design and to set the cart/model separation distance.

Method of Analysis. The interference created by the cart and model support system were studied through use of a panel method. This was done in a three-step procedure where the influence of the cart alone was first considered. This was followed by the influence of the model support by itself and then by the combined influence of the two.

The disturbance velocities computed by the panel method were converted into lift and drag deviations by considering two separate effects: 1) changes to the free-stream speed due to the blockage created by the model support and cart; and 2) effective changes to the angle of attack due to a vertical flow component (flow-induced effective twist). Since both lift and drag depend quadratically on the flow velocity, a given small percentage deviation in free-stream velocity results in twice that percentage deviation in lift or drag. This rule was used for the blockage errors. In order to analyze the effects of induced twist, a lifting-line model was used to compute the lift and drag distributions on a wing with an effective twist distribution generated by the predicted vertical velocity component. These values of lift and drag were then compared with those of an untwisted wing in order to obtain relative errors. In this analysis, the angle of attack was fixed at 2 degrees.

Results

Influence of the Cart. The cart produces disturbances that fall off rapidly at first, but then transition to an asymptotic slow approach to quiescent conditions with increasing distance from the cart. This behavior is expected since the tunnel walls only allow the disturbances to spread in a single direction for distances of about a tunnel diameter or more. The computed results showed that although the disturbances would generate less than 0.4% errors in lift or drag at a separation of 16 ft (4.9 m) between the model wing and the cart, a separation distance of 28 ft (8.5 m) was required to drop the errors to 0.2%. Thus, in order to meet the error requirement, the cart/model separation distance was set at 28 ft (8.5 m).

While 28 ft (8.5 m) seems like a rather long separation distance, it should be noted that the length required for the boom that supports the model will be less than the 28 ft (8.5 m) since the wing is displaced a considerable distance from the aft end of the model. As an example, a 1:19 scale model of a 747 has roughly 10 ft (3.0 m) between the center of pressure of the wing and the tail end. Thus, a boom of approximately 18 ft (5.5 m) will provide the required 28-ft (8.5-m) separation.

Influence of the Model Support System. The model support system consists of an articulated boom that extends 18 ft (5.5 m) in front of the cart. Much of the boom design is constrained by structural considerations, and the main objective was to determine the influence for a few permissible cross-sectional diameters. Diameters of 24, 30, and 36 in (61, 76, and 91 cm) were analyzed but only the 24-in (61 cm) boom could meet the lift and drag error requirements. Thus, the diameter was fixed at 24 in (61 cm).

Influence of the Combined Cart/Model Support System. The combined influence of the cart and model support system was calculated by including both of these objects in the panel solution simultaneously. The model support system described above with the 24-in (61 cm) boom was considered, and the influence was computed at the assumed wing position of 28 ft (8.5 m) ahead of the cart. Results from these simulations are shown in Figure 29. The blockage error meets the 0.002 requirement over the entire angle-of-attack range, but the twist error exceeds the requirement for angles of attack less than approximately 4 degrees. This problem is nearly unavoidable since the relative error will be large for even a small amount of twist near the zero lift condition ($\alpha=0$). By increasing the cart/model separation distance or by reducing the boom diameter, the twist error can be reduced, but this will only have the effect of moving the error-violating angle of attack from 4 degrees to a slightly smaller angle. Based on this observation, along with the structural problems that would arise by undertaking either of these two options, one is motivated to leave the design as stated above.

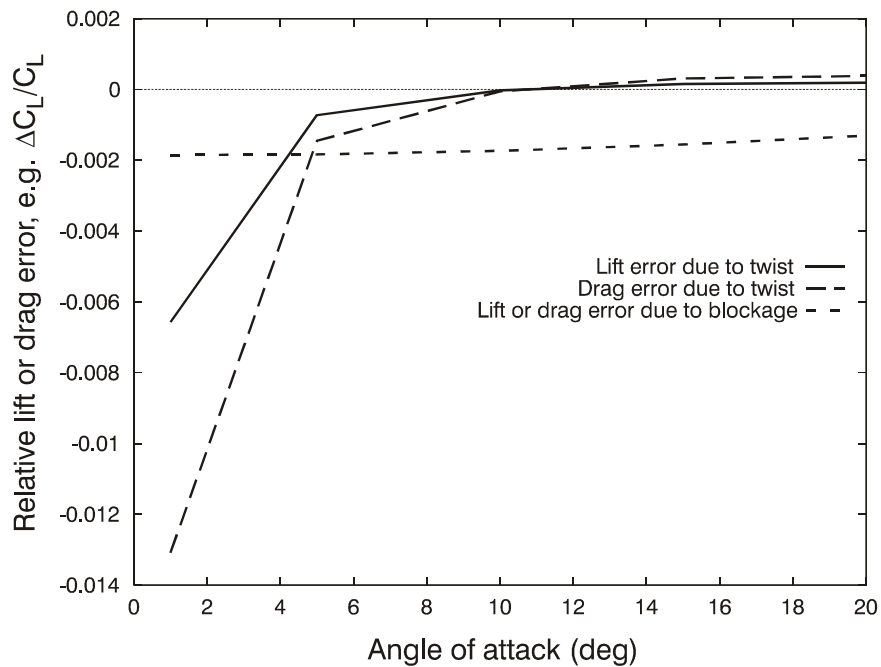


Figure 29. Combined influence of the cart and model support system on the model.

Possible Design Modifications. The design of the model support system involves several compromises between structural and aerodynamic considerations. The structural concerns are yield strength, static deflection, and natural frequency, all of which become problematic as the boom length is increased and as its diameter is decreased. The aerodynamic considerations are exactly opposite where a long, slender boom is desirable. There is little that can be done to improve the structural behavior since the design already calls for very high-strength composite materials. It may be easier to reach a compromise on the aerodynamic side through the use of data correction schemes (Ref. 4). As mentioned above, the interference due to the cart begins to flatten out at approximately a 16-ft (4.9 m) separation distance. Thus, if data correction schemes could be devised to remove half of the error or more, it may be possible to reduce the boom length by as much as 12 ft (3.7 m). Similarly modest increases in the boom diameter do not lead to enormous error and the excess due to this source could also be reduced through the use of a data correction scheme.

Effects of Acoustic Waves

As the model accelerates, it exerts a time-dependent pressure force on the surrounding fluid. This unsteady force acts as the source for acoustic waves, which then propagate away from the model at the speed of sound. These waves will reflect off the tunnel side and end walls and impinge on the model, thereby introducing unwanted disturbances. Most of the analysis presented here focuses on the components of the wave that travel longitudinally and reflect off the tunnel end walls. The waves that reflect squarely from the side walls are not expected to be as important since their direction of travel is perpendicular to the motion of the model. These transverse waves are therefore left behind and do not contact the model at a later time. Some reflections with the side walls will occur at an oblique angle so the disturbances they create will decrease with time as the waves spread. In addition, acoustic wedges affixed to the tunnel walls will further reduce the amplitude of these oblique waves.

Model/Longitudinal Acoustic Wave Interactions. Interactions between the model and longitudinally traveling acoustic waves were predicted by writing the equations for the position of the waves as a function of time and then solving these equations simultaneously with those for the position of the model.

Figures 30 and 31 show typical interactions with the compression and expansion waves, respectively, on x-t diagrams. The test conditions are $M=0.35$ and $T=-250$ °F (-157 °C).

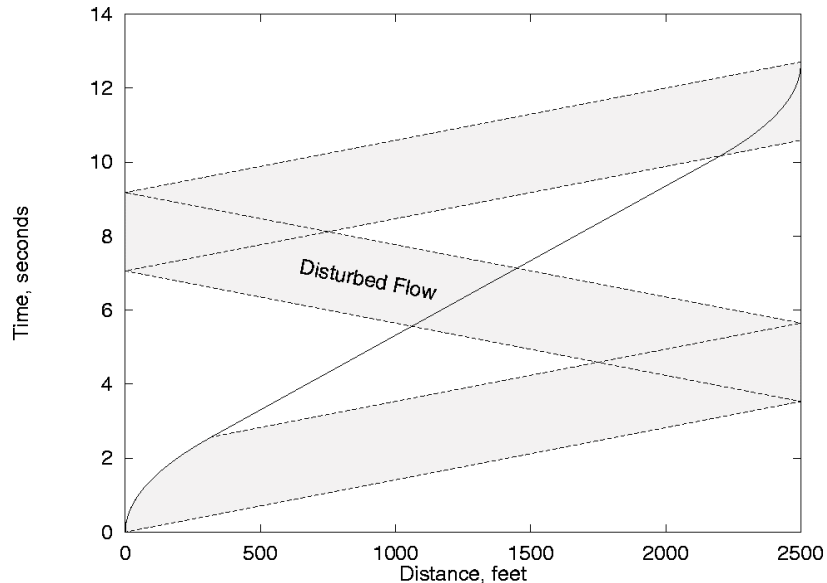


Figure 30. Typical interactions with the compression wave. The solid line is the model trajectory, whereas the shaded band shows the envelope of the acoustic waves. The test conditions are $M=0.35$, $T=-250$ °F (-157 °C), $a=3g$ (29.3 m/s²), and $L_T=2,500$ ft (762 m).

In this case, the compression wave impacts the model once during the constant-speed portion of the test and a second time during the deceleration phase. Prior to the first impact (for about one-third of the test time), the model is not influenced by the compression wave. Interactions with the expansion wave are similar. The head of the wave moves on a trajectory that is essentially the same as the compression wave since the reflection of the near tunnel end wall occurs within a negligibly short time after the model is set

into motion. The tail of the expansion wave moves on a somewhat different trajectory, since it must first travel opposite the model for a distance of x_1 before reflecting off the near end wall. This effect causes the expansion wave pulse to be wider than the compression pulse. In addition, the model is influenced by the expansion waves during the entire acceleration phase, as well as for a short time afterward. Thus, in the case illustrated in Figure 31, the expansion wave contacts the model twice during the constant-speed portion of the test; once from the beginning of the test to a short time afterward and again near the middle of the test.

Several possibilities exist for the number of interactions and when they occur. However, there will always be at least two interactions, and at least a portion of one of these will fall within the constant-speed portion of the test. Generally, the number of interactions increases as the Mach number decreases. In addition, the duration of the interactions relative to the test time decreases as the Mach number is decreased.

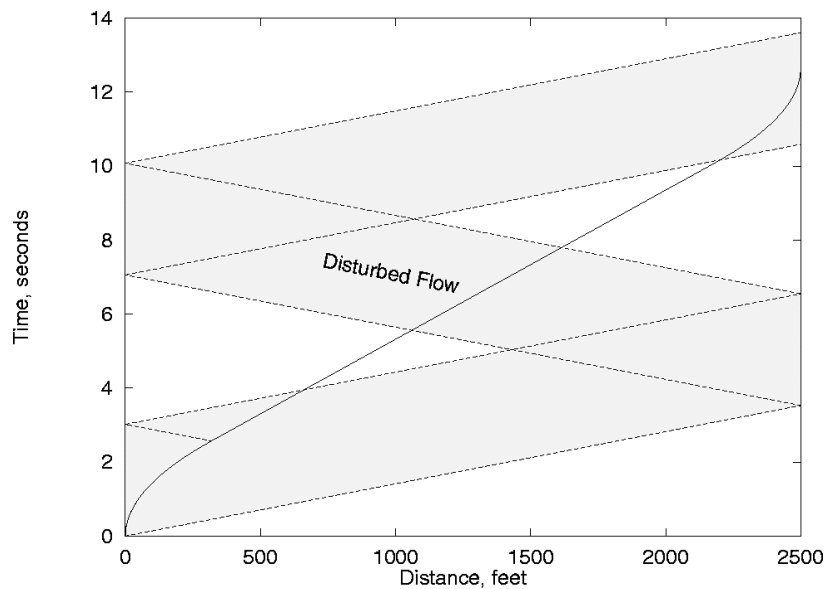


Figure 31. Typical interactions with the expansion wave. The solid line is the model trajectory whereas the shaded band shows the envelope of the acoustic waves. The test conditions are $M=0.35$, $T=-250$ °F (-157 °C), $a=3g$ (29.3 m/s²), and $L_T=2,500$ ft (762 m).

Strength of the Acoustic Waves. The longitudinal acoustic wave strength is estimated in a two-step procedure. In the first step, an incompressible control volume analysis is used to make a preliminary estimate for the wave strength and wave form. In the second step, corrections are applied for the effects of compressibility as well as for nonlinear wave steepening.

The incompressible analysis is based on a control volume analysis that ensures conservation of momentum and kinetic energy. When the model passes through the tunnel, fluid particles that lie in its path must move out of the way. These particles circulate around the body and ultimately fill space behind it. A certain amount of kinetic energy is associated with the circulatory flow, and work must be done on the fluid in order to create it. This work shows up as a “drag” force during the acceleration phase (since it is then that the kinetic energy is changing with time). The force is computed by relating the kinetic energy

at time t to the work done from $t=0$ to t . In turn, this force will produce a change in the momentum of the fluid in accordance with Newton's second law. Part of this momentum stays in the near field, while the remainder propagates away in the form of acoustic waves. A control volume analysis was used to estimate the wave strength by assuming the waves become one-dimensional as they propagate down the tunnel. The result of this analysis is:

$$\frac{\Delta u_0}{U} = \frac{1}{2}MA \left(K^* - \frac{1}{2}J^* \right) = \frac{1}{M} \left(K^* - \frac{1}{2}J^* \right) \left(\frac{al}{\gamma RT} \right) \quad (1)$$

where Δu_0 is the disturbance velocity, U is the steady state model velocity, M is the Mach number, a is the acceleration rate, l is the model length scale γ is the specific heat ratio, R is the gas constant, and T is the temperature. The quantities A , K^* , and J^* are the acceleration parameter and near-field kinetic energy and momentum, respectively, which are defined as:

$$A = \frac{2al}{U^2} \quad (2)$$

$$K^* = \frac{1}{\pi R_t^2 l} \int_V \frac{1}{2} \left(\frac{\vec{u} \cdot \vec{u}}{v_m^2} \right) dV \quad (3)$$

$$J^* = \frac{1}{\pi R_t^2 l} \int_{n.f.} \left(\frac{u}{v_m} \right) dV \quad (4)$$

Where R_t is the tunnel radius, u is the near-field disturbance velocity, v_m is the time-dependent model velocity, V is the integration volume, ρ is the density, and *n.f.* denotes an integration taken only over the near field.

The normalized kinetic energy and near-field momentum integrals, K^* and J^* , depend on the geometry of the collection of moving parts within the tunnel (i.e., drive cart, model support, and model). The disturbance kinetic energy and momentum associated with the current HiLiFT drive system were estimated using a three-dimensional panel method with the results $K^*=0.15$, $J^*=-0.30$.

The effects of compressibility act to increase the wave strength by a Mach number dependent factor. Regression of data from numerical simulations of the accelerating cart was used to determine the required multiplying factor with the result:

$$\frac{\Delta u}{\Delta u_0} = \frac{1 + 1.5M + 11.0M^{2.5} + 12.75M^{3.5}}{1 - M} \quad (5)$$

The nonlinear steepening of the wave as it propagates changes its waveform but not its maximum perturbation velocity. Thus, the above expression is sufficient to characterize the maximum wave strength. The effects of wave steepening will be discussed in the following subsection where a wave damping mechanism is proposed.

Figure 32 shows the result of Eq. (5) with the above quoted values of K^* and J^* . If Eqs. (1) and (5) are combined, it is apparent that the wave strength is composed of two terms, one proportional to $1/M$ and the

other to M . The first term arises from the incompressible analysis and the $1/M$ scaling is a result of using the model speed (U) as a normalizing velocity. The second term is due to the effects of compressibility. For low Mach numbers, the first term will dominate and the relative wave strength is fairly large, reaching 0.22% at $M=0.05$. As the Mach number is increased, the relative wave strength falls to a minimum where the second term starts to become important. The minimum occurs at $M=0.2$, where the relative wave strength is about 0.1%. Further increases in the Mach number result in a steady increase in the relative wave strength, and a value of approximately 0.19% is achieved at $M=0.5$.

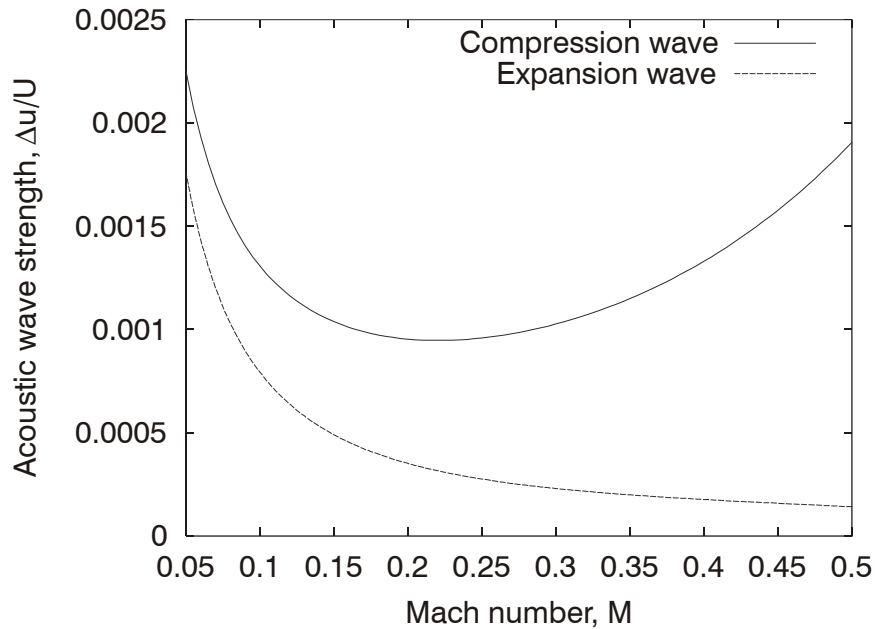


Figure 32. Relative strength of the reflected longitudinal acoustic wave. Test conditions are $T=-250$ °F (-157 °C), $a=3g$ (29.3 m/s²), $l=1.65$ ft (0.50 m).

Since lift and drag depend quadratically on speed, the expected deviations in these quantities will be approximately double the acoustic wave strength, or within the range 0.20%–0.44%. These errors are outside the 0.2% error limit, and thus, an end wall damping mechanism is required in order to reduce the reflected wave strength. The damping system must be rather effective since a maximum attenuation factor of $1-(0.2/0.44)=0.55$ is needed. A damping system meeting this requirement is discussed in the following subsection.

End Wall Damping System. Prior to discussing the end wall damping system, it is first necessary to characterize the waveform of the longitudinal acoustic wave. The analysis of the previous section was used as the input to a method of characteristics calculation where the nonlinear steepening of the wave was accounted for. The result of such a calculation for $M=0.3$ is shown in Figure 33.

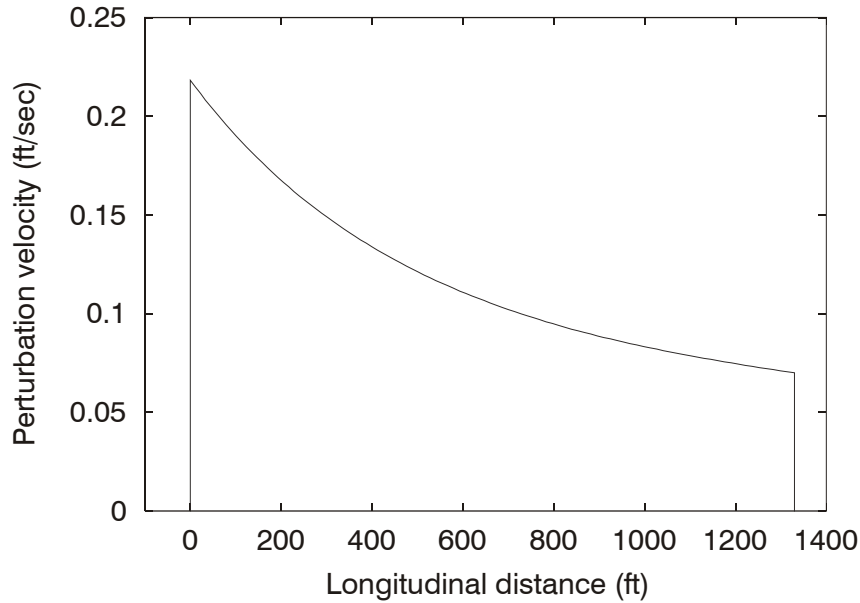


Figure 33. Longitudinal acoustic wave shape. Test conditions are $M=0.3$, $T=-250\text{ }^{\circ}\text{F}$ ($-157\text{ }^{\circ}\text{C}$).

The waveform can be decomposed into two parts—a square wave and an algebraic ramp. The square wave results from the assumed square wave acceleration profile in connection with the incompressible part of the analysis presented in the previous section. The algebraic ramp is due to the effects of compressibility and wave steepening. In absolute terms, the disturbance velocity within the wave is fairly modest, ranging from about 0.07 ft/s (0.021 m/s) at the leading edge to about 0.22 ft/s (0.067 m/s) at the trailing edge. The wave is seen to cover slightly more than half the length of the tunnel in this case. The waveform on a time axis is identical as can be seen from the transformation $t=x/c$, where c is the sound speed. At $-250\text{ }^{\circ}\text{F}$ ($-157\text{ }^{\circ}\text{C}$), $c=709\text{ ft/s}$ (216 m/s); thus, the pulse width is $1,330/709=1.9\text{ s}$. Waveforms for other Mach numbers are similar. The pulse widths vary from 0.36 s at $M=0.05$ to 2.8 s at $M=0.5$.

Several different end wall damping mechanisms were considered. Although passive systems such as baffles or acoustic cones are attractive due to their simplicity, no system could be found where attenuations in the 55% range could be achieved for waves with pulse widths in the 0.36–2.8 s range (0.36–2.8 Hz). As a result of this, effort was focused on active damping systems.

The chosen active damping system is shown in Figure 34 and consists of a movable diaphragm located 2 ft (0.6 m) upstream of the tunnel end wall. Prior to the incident acoustic wave reaching the tunnel end, the diaphragm is moved forward in order to launch an expansion wave at the oncoming compression wave. If the diaphragm velocity exactly matches the oncoming wave perturbation velocity (as shown in Figure 33), then the compression wave will be canceled and no reflection will occur. The required diaphragm velocity is quite low, reaching only 0.22 ft/s (0.067 m/s) for a $M=0.3$ test. The motion lasts for about 1.9 s, which results in a diaphragm displacement of approximately 2.6 in (6.7 cm). For $M=0.5$, a maximum velocity of approximately 0.7 ft/s (0.21 m/s) is required. The motion lasts for approximately 2.8 s, and a displacement of about 6.6 in (16.8 cm) results.

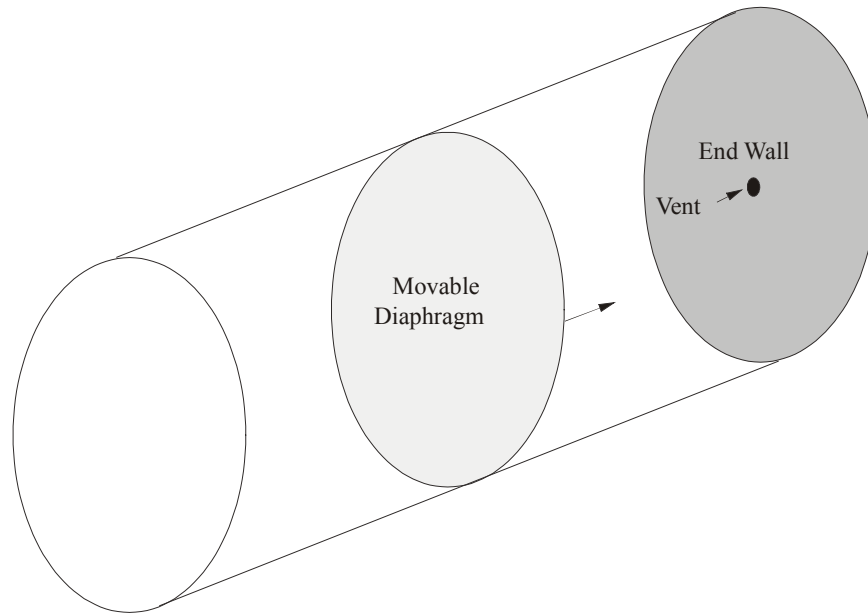


Figure 34. Proposed end wall damping system. The diaphragm moves forward in order to launch an expansion wave that nearly cancels the incident compression wave. Diaphragm velocity is at most a few feet per second.

The success of the active control system hinges on the ability to replicate the oncoming wave perturbation velocity with the diaphragm motion. Any errors in the diaphragm velocity will result in residual waves that will reflect and contact the model. Thus, in order to achieve attenuation rates in the 50% range, it is necessary to control the diaphragm to within approximately 50% of the target speed. This rather modest requirement appears feasible, especially given the low velocities involved.

A rather simple pneumatic drive mechanism can be arranged by placing a controllable valve (vented to the atmosphere) on the tunnel end wall. By opening the valve, the pressure in the volume between the diaphragm and the tunnel end wall is reduced, and the diaphragm will move toward the end wall. By correct scheduling of the valve, any desired diaphragm motion can be achieved. The only limitations of this system are the lags associated with mechanically opening the valve, the propagation of the pressure wave within the diaphragm chamber, and the inertia of the diaphragm itself. Once these lags are understood, they can be incorporated in a computer controller, which actuates the valve. Such a control system could also receive information about the oncoming wave from pressure sensors mounted along the tunnel length. This would allow the exact waveform to be known and limit the sources of error to the finite rise time of the combined mechanical system.

Although the far tunnel end wall is of primary concern, the near end wall could also have an active damping system in order to limit the reflection of expansion waves. A nearly identical system would be used on the near end wall, with the modification that the diaphragm must move away from the end wall in this case. This difference would of course require high pressure nitrogen to be injected through the valve in order to move the diaphragm.

Oblique Acoustic Waves. In addition to the longitudinal wave that reflects off the tunnel end wall, the model will also be affected by transverse and oblique waves that reflect off the tunnel side walls. Unlike the one-dimensional longitudinal waves that conserve their energy density, the oblique waves are three-

dimensional waves where the energy density reduces with time as the waves spread. This mechanism leads to a natural attenuation of the wave strength. The natural attenuation is complemented by acoustic wedges mounted on the tunnel side walls. The combination of the two damping mechanisms is quite effective at damping the oblique waves.

The transverse and oblique waves will have characteristic frequencies that can be estimated from the speed of sound and the tunnel diameter.

For the $-250\text{ }^{\circ}\text{F}$ ($-157\text{ }^{\circ}\text{C}$) condition and 20-ft (6.1-m)- diameter tunnel, the frequency is 35 Hz. For warmer temperatures, the frequency rises, reaching approximately 55 Hz for $70\text{ }^{\circ}\text{F}$ ($21\text{ }^{\circ}\text{C}$). The acoustic wedges are more effective at higher frequencies, and thus, the damping is greater at higher temperatures. Since residual acoustic noise is expected to be greatest in the $-250\text{ }^{\circ}\text{F}$ ($-157\text{ }^{\circ}\text{C}$) condition, this temperature was selected.

Over each oscillation cycle, the waves reflect off tunnel side walls once, and by virtue of the acoustic wedges, lose a fraction of their energy. This loss factor is denoted as C_a . In terms of the reflected energy, a factor of $1-C_a$ of the incident energy is left upon reflection. Since each subsequent reflection again removes this fraction of the wave energy, the energy left after n reflections is simply $(1-C_a)^n$.

The number n is related to the time and frequency via $n=ft$. Thus, the damping in time due to the acoustic wedges will be of the form $E(t)=E_0(1-C_a)^{ft}$, where $E(t)$ is the wave energy and $E_0=E(t=0)$.

The attenuation due to wave spreading can be determined through a conservation of energy argument. Assume that the energy is initially distributed over a volume l_0A_{cs} , where l_0 is a distance measured along the tunnel axis (i.e., size of the accelerating object) and A_{cs} is the tunnel cross-sectional area. As time increases, the waves spread in the longitudinal direction at the speed of sound, c . Thus, the volume increases according to $(l_0+ct)A_{cs}$. If the energy within the wave is fixed, the energy density then decreases in time with the volume ratio (i.e., $E(t)=E_0[l_0/(l_0+ct)]$).

Combining the two forms of damping and noting that wave disturbance velocity is proportional to the square root of its energy, gives:

$$\Delta u(t) = \Delta u_0 \left[\frac{(1-C_a)^{ft}}{1 + \frac{ct}{l_0}} \right]^{\frac{1}{2}} \quad (6)$$

The initial amplitude Δu_0 can be estimated using the longitudinal wave strength determined in the previous subsection. The noise-generating length scale l_0 can be assumed to be the overall length of the cart, model support, and model, or approximately 60 ft (18.3 m). Finally, the absorption coefficient for the acoustic wedged at 35 Hz is quoted by the manufacturer as $C_a=0.136$.

The above relation is used to generate the time history of the expected oblique acoustic wave disturbance for $M=0.3$, as shown in Figure 35. The figure shows that significant attenuation is achieved after 1 s. When compared with the available test time, it was found that oblique wave amplitudes are damped below the $(2 \times 10^{-3})U$ level within 1% of the test time for all Mach numbers.

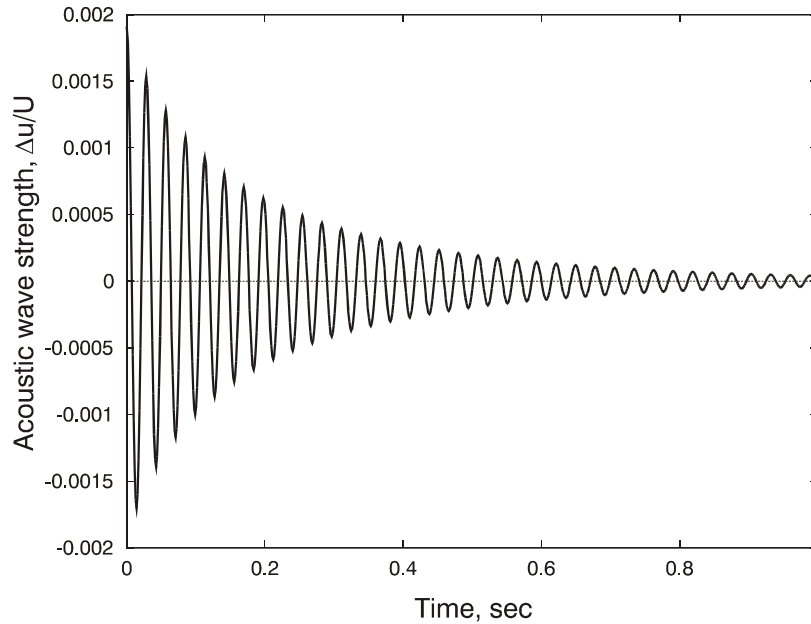


Figure 35. Time history of the relative strength of the reflected oblique acoustic waves. Test conditions are $a=3\text{ g}$ (29.3 m/s^2), $T=-250\text{ }^\circ\text{F}$ ($-157\text{ }^\circ\text{C}$), $l=1.65\text{ ft}$ (0.50 m), $l_0=60\text{ ft}$ (18.3 m), $C_a=0.136$.

Aerodynamic Loads

Steady-State Cart/Model Support Loads. Aerodynamic loads on the cart and model support were estimated by adding together a weighted average of force coefficients for each member of the cart/model support system. Individual force coefficients were obtained using standard aerodynamic drag tables (Ref. 5). Summation weights were based on the fraction of total frontal area. Force centroids were also computed in order to provide information for reacting the resulting pitching moments. The composite cart/model support drag coefficient was found to vary between $C_D=0.313$ and $C_D=0.324$, as the angle of attack varies from 0 to 20 degrees. Over the same angle-of-attack range, the composite lift coefficient varies between 0 and $-7.62 \cdot 10^{-3}$. The effective frontal area used in the composite force coefficients is 42.3 ft^2 (3.93 m^2).

The predicted lift load is rather modest, being exactly zero for $\alpha=0$ and increasing to only -900 lb -4 kN for $\alpha=20$ degrees and $M=0.5$. The dependence is approximately linear with angle of attack and is quadratic with the Mach number. The drag force is much greater, increasing to more than $38,000\text{ lb}$ (169 kN) for the $\alpha=20$ degrees, $M=0.5$ condition. The drag force is almost independent of angle of attack but varies quadratically with Mach number.

The cart is responsible for the bulk of the drag force due to its large wetted area. Streamlining of the vertical model support columns as well as the cart nose and tail was already assumed in the above estimates. Aside from this, there is not much additional opportunity to significantly reduce the drag.

Flow Establishment Time

Relaxation from Acceleration–Lifting Models. Due to the rapid acceleration as the model is brought up to test speed, the flow is displaced from equilibrium, and a relaxation period is required for the flow to become fully developed once the desired model speed is reached. This so-called “flow establishment time” delay must be estimated carefully in order to avoid taking measurements in a transient environment. This information is also important for the design of the facility since it effectively reduces the time interval over which data can be sampled. A related relaxation process exists if the model orientation is changed during the course of the run. In order to increase the productivity of the facility, it may be advantageous to change the model attitude and/or speed, either discretely or continuously, during the test. In this case, it is necessary to know how much of a delay to allow before sampling data after discrete changes; or alternatively, what the maximum acceleration rate for continuous changes is that leaves the flow in a quasi-steady state.

As a lifting model is accelerated, lift builds with time, thereby requiring an increasing circulation around the body. According to Kelvin’s law (Ref. 6), this increase in circulation must be matched by an equal and opposite amount of circulation added to the wake. This circulation is usually referred to as the “starting vortex,” although it is actually a distributed vortex sheet. The starting vortex sheet induces a downwash on the wing that lowers the effective angle of attack and thus lowers the lift. The starting vortex sheet more or less remains where it was created, and thus, the wing is able to move away from its influence as time increases. The downwash falls off inversely with distance or equivalently inversely with time when the model is moving at constant speed.

An analysis of the flow establishment time was conducted using a combination of two- and three-dimensional simulations as well as two- and three-dimensional unsteady potential flow models. The simulations account fully for compressibility effects and are highly resolved in both space and time. Due to their relative complexity and high resolution, they are computationally intensive, especially in three dimensions. For this reason, the simulations were used mainly to validate the simplified potential flow models. These models are highly efficient, rarely requiring more than a minute of computer time per run.

The bulk of the results discussed in this section were generated with an unsteady potential flow model consisting of a panel method for the wing and a collection of discrete vortices for the wake (Ref. 7).

Results from a typical simulation are shown in Figure 36. It is seen that, except for a brief period near the start of the acceleration, the development of lift lags behind the quasi-steady value. The transient persists long after the model reaches constant speed and is not nearly complete by the time it takes the model to travel 30 characteristic lengths.

The relaxation to steady state is an asymptotic process that can be visualized more readily by plotting the lift deficit $(1-L/L_\infty)$ as a function of time. Such a plot is shown in Figure 37.

It is evident that the approach to steady state is a slow process, with more than 50 time units required to bring the lift to within 1% of the steady-state value. Figure 37 also demonstrates that the final approach to steady state is proportional to $1/(t-t_1)$. This result is expected since the downwash created by the starting vortex falls off inversely with separation distance, a quantity that is proportional to $t-t_1$.

Given the slow approach to steady state, one has two choices in treating the experimental data: 1) allow a sufficient delay so that the unsteady lift error is within the measurement tolerance, or 2) make use of the $1/(t-t_1)$ behavior and correct for the residual lift variation. In order to illustrate these two alternative

approaches, a scenario in which the lift must be measured to within 0.2% (as indicated by the dashed horizontal line in Figure 37) is considered.

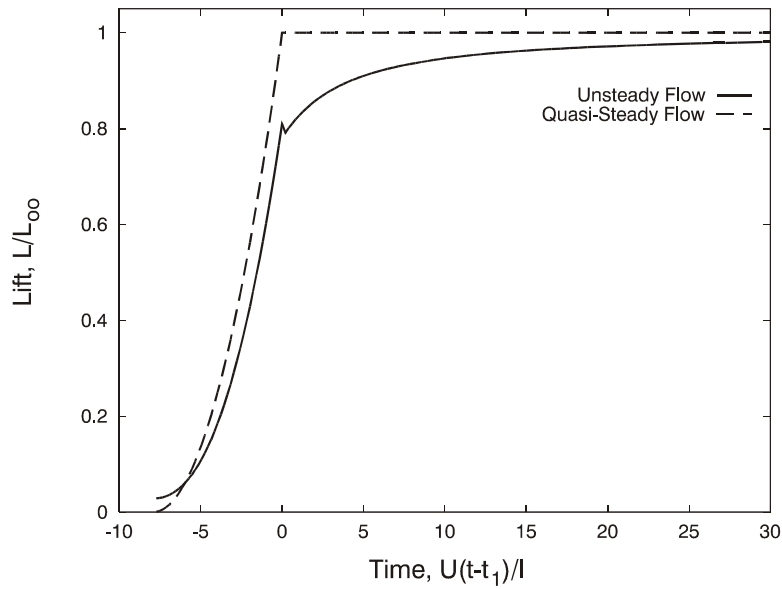


Figure 36. Lift history for the unsteady wing motion. Acceleration ends at $t=t_1$. Acceleration parameter $A=0.25$, which corresponds to $M=0.05$, $a=3\text{ g}$ (29.3 m/s^2), $l=1.64\text{ ft}$ (0.50 m), $T=-250\text{ }^\circ\text{F}$ ($-157\text{ }^\circ\text{C}$).

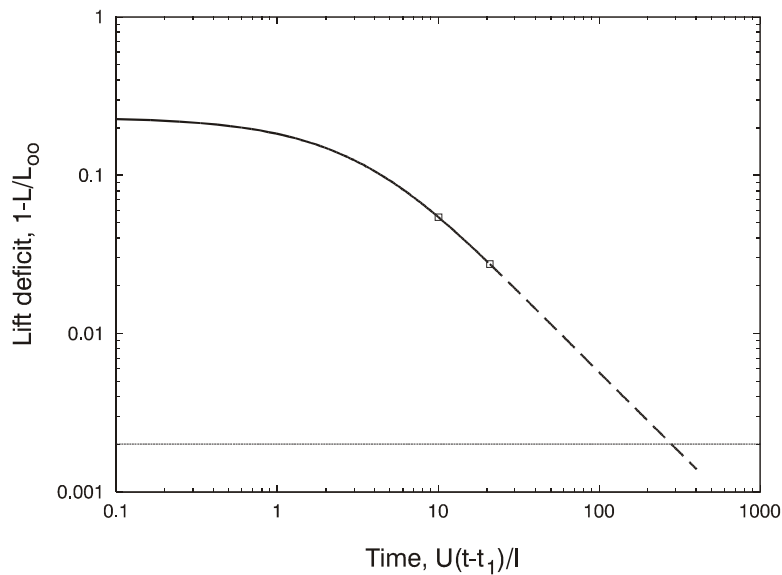


Figure 37. Approach to steady state as characterized by the lift deficit. Acceleration ends at $t=t_1$. Acceleration parameter $A=0.25$, which corresponds to $M=0.05$, $a=3\text{ g}$ (29.3 m/s^2), $l=1.64\text{ ft}$ (0.50 m), $T=-250\text{ }^\circ\text{F}$ ($-157\text{ }^\circ\text{C}$).

If the direct measurement approach is used, a delay of roughly 300 time units must be allowed in this case. While this seems to be a rather long period, one should compare this delay with the available test time (time that the model is moving at constant speed). The latter is given by:

$$\Delta t_{test} = \frac{l}{U} \left(\frac{L_T}{l} - \frac{2}{A} \right) \quad (7)$$

where L_T is the overall tunnel length.

A comparison of the flow establishment time (Δt_{ss}) to the available test time as a function of Mach number is shown in Figure 38. The data show that a delay roughly between 10% and 20% of the available test time must be allowed if the raw lift data is to be accurate to within 0.2% of the true steady-state value. Although the test time decreases with Mach number, the flow establishment time also decreases due to the M^{-2} dependence on acceleration parameter A . The net effect is a relative decrease in delay with increasing Mach number.

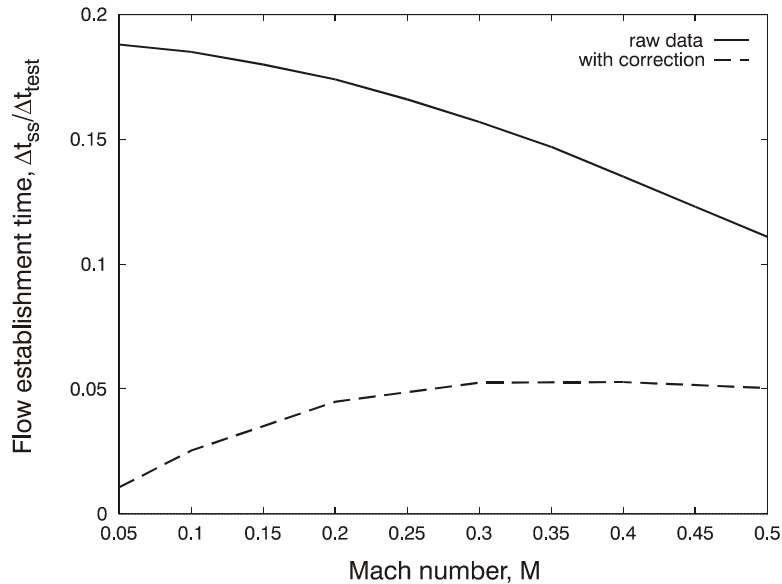


Figure 38. Flow establishment time as a fraction of available test time, plotted as a function of Mach number. Residual unsteady lift error is set at 0.2%. Other parameters are $a=3g$ (29.3 m/s^2), $l=1.64 \text{ ft}$ (0.50 m), $T=-250 \text{ }^\circ\text{F}$ ($-157 \text{ }^\circ\text{C}$), $L_T=2,500 \text{ ft}$ (762 m).

The required delay can be reduced by making use of a data correction scheme where extrapolation is used to estimate the steady-state lift value from two or more data points taken in the unsteady regime. The basic procedure is illustrated in Figure 37, where the two represent a pair of measurements taken when the flow is still rather far from equilibrium. If these measurements are within the $1/(t-t_1)$ asymptotic regime, the following extrapolation scheme can be used to estimate the steady-state lift value:

$$L_\infty \approx L_3 + \frac{(L_3 - L_2)}{t_3 - t_2} t_3 \quad (8)$$

where L_2 and L_3 are two independent lift measurements taken at times t_2 and t_3 , respectively. Note that this approach is self-calibrating and only requires that the two measurements be made in the $1/(t-t_1)$ asymptotic regime. In order to determine the earliest time when the correction procedure can be used, the extrapolation scheme was applied to the simulation data, and estimates of the steady state lift were compared to the true value. The time where the residual error dropped below 0.2% was noted; this information is shown in Figure 38. The correction scheme results in a sizable reduction in the required measurement delay, limiting it to approximately 5% of the available test time.

Nonequilibrium due to Continuous Pitch Change. In order to enhance the productivity of the HiLiFT, it may be desirable to vary the model attitude during the course of the test. Multiple measurements could be taken during the course of the attitude variation so that several data points are collected during a single run. A scenario where the angle of attack is varied continuously for the duration of the constant-speed portion of the test is considered in hopes of obtaining a complete drag polar in a single run. A variation of this type again results in a nonequilibrium flow due to the induction caused by the starting vortices shed into the wake as the lift increases with increasing angle of attack. Ideally, one would like to sample data at any angle of attack during the pitch change and have the measured lift and drag values agree with those steady state conditions.

The continuous pitch process is governed by a third parameter, namely the reduced frequency, given by:

$$\dot{\alpha}_r = \frac{d\alpha}{dt} \left(\frac{l}{U} \right) \quad (9)$$

If it is assumed that an angle of attack variation of $\Delta\alpha$ is to be made over the course of the constant-speed portion of the test, the pitch change rate will be $d\alpha/dt = \Delta\alpha/\Delta t_{ss}$. Making use of this result, Eq. (9) can be written as:

$$\dot{\alpha}_r = \frac{\Delta\alpha}{\frac{L_T}{l} - \frac{2}{A}} = \frac{\Delta\alpha}{\frac{L_T}{l} M^2 \left(\frac{\gamma RT}{al} \right)} \quad (10)$$

where $\Delta t_{ss} = L_T/U - U/a$ has been used. This relation is interesting since it demonstrates that the reduced frequency depends only weakly on the Mach number. The reduced frequency is nearly fixed at $\Delta\alpha/(l/L_T)$ for Mach numbers up to approximately 0.2. Even at $M=0.5$, the reduced frequency is only slightly more than twice this value. These observations indicate that the continuous pitch response will be rather similar across the full Mach number range.

The importance of nonequilibrium effects during continuous pitch change was analyzed using the same potential flow model discussed earlier. Simulations were conducted where the initial angle of attack, as well as the number of degrees of variation were specified. The angle-of-attack variation was assumed to consume the entire constant speed portion of the test. The results were reduced by comparing the computed unsteady lift with quasi-steady values obtained by assuming steady flow at any given instant. Results for angle of attack sweeps of 0–10 and 10–20 degrees for $M=0.3$ are shown in Figure 39. For a constant pitch rate and constant model speed, circulation is added to the wake at a constant rate. This circulation distribution leads to a downwash that increases rather slowly with time. Consequently, the lift error is approximately constant over the angle of attack variation. This means that for a fixed number of degrees of pitch change the relative lift error will be greater when the angle of attack (and hence lift) is low. This effect is clearly visible in Figure 39 where the relative error for the 0-10 degree sweep is much

greater than that for the 10–20 degree sweep. These results also show that the 0.2% lift accuracy requirement could be obtained throughout the 10 degree pitch change maneuver, provided that the initial angle of attack is 10 degrees. Conversely, the 0.2% lift accuracy is exceeded over the entire course of the same 10 degree variation if the starting angle of attack is zero.

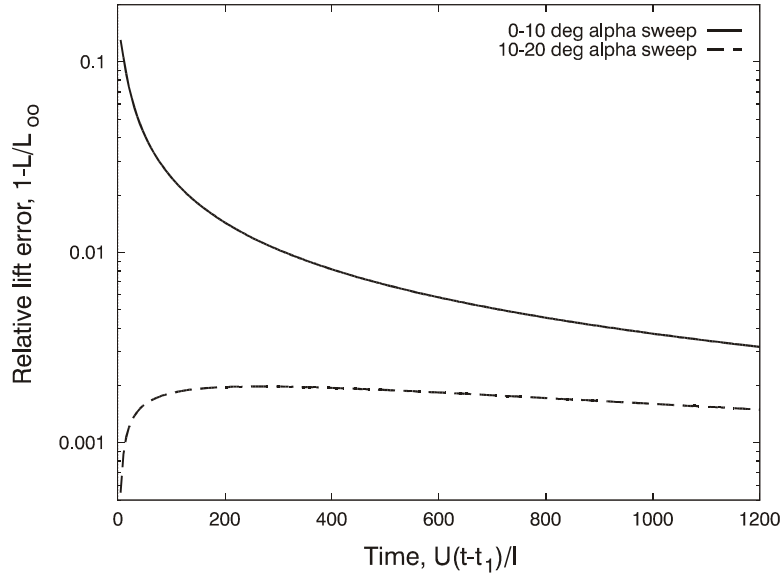


Figure 39. Typical lift error due to nonequilibrium flow during a continuous pitch change maneuver. Test conditions are $M=0.3$, $a=3g$ (29.3 m/s^2), $l=1.64 \text{ ft}$ (0.50 m), $T=-250 \text{ }^\circ\text{F}$ ($-157 \text{ }^\circ\text{C}$), $L_T=2,500 \text{ ft}$ (762 m).

Given that the rate of increase of circulation in the wake is known, it is possible to derive a simple data correction scheme where this information is used to estimate the downwash on the wing at any instant. The downwash can then be translated into lift and drag corrections that are added to the measured values in order to obtain close estimates for the steady-state forces. The lift correction is:

$$\Delta C_L = m \left(\frac{1}{2} \left(\frac{m}{2\pi} \right) \dot{\alpha}_r \right) \log \left(\frac{\chi - \chi_1}{0.75l} + 1 \right) \quad (11)$$

where C_L is the lift coefficient, $m=dC_L/d\alpha$ is the lift curve slope, $[\dot{\alpha}_r]$ is the reduced frequency, x_1 is the longitudinal position where the angle of attack sweep is begun, and the factor 0.75 is the fraction of the wing chord ahead of the trailing edge where the downwash is assumed to act (here the length scale l is associated with the wing chord). The logarithmic term arises from the integration of the induction caused by the uniform circulation distribution in the wake (proportional to $1/((x-x_1)/l+0.75)$).

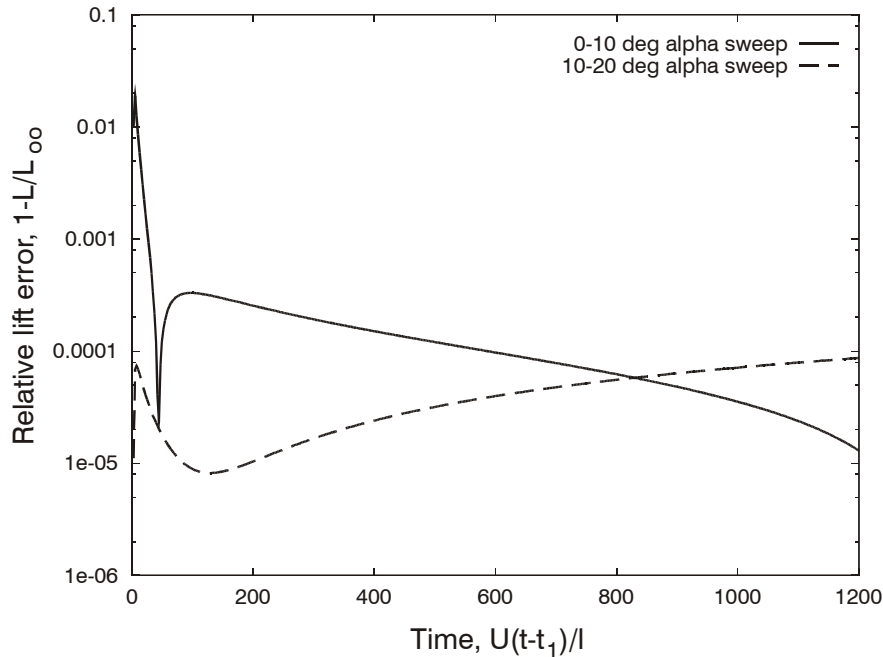


Figure 40. Residual lift error from corrected measurement values obtained during a continuous pitch change maneuver. Test conditions are $M=0.3$, $a=3g$ (29.3 m/s^2), $l=1.64 \text{ ft}$ (0.50 m), $T=-250 \text{ }^\circ\text{F}$ ($-157 \text{ }^\circ\text{C}$), $L_T=2,500 \text{ ft}$ (762 m).

The lift correction scheme is applied to the data in Figure 39, and the residual error is plotted in Figure 40. In comparing Figures 39 and 40, it is evident that the error is reduced by one to two orders of magnitude when the correction scheme is employed. It is also clear that the 0.2% lift error requirement is met everywhere except for a small region near $\alpha \cong 0$ on the 0–10 degree sweep. It is virtually impossible to meet the relative lift error accuracy requirement near the zero lift condition since the error is normalized by the expected lift value, the latter of which is vanishingly small. As a matter of curiosity, the dip in error for 0–10 degree sweep near $U(t-t_1)/l \cong 50$ is caused by a change in sign of the error, which translates into a dip when the absolute value is taken in order to fit the data on a log scale.

Nonequilibrium due to Continuous Pitch Change—Partially Stalled Wings. In certain cases, the angle of attack may exceed the stall limit during a continuous pitch change maneuver. It is of interest to investigate whether the presence of separated flow has an effect on the flow establishment time. An attempt was made to investigate this issue via numerical simulations of a pitching three-dimensional wing. This proved to be a very difficult computational problem due to the rather low reduced frequencies under consideration here. The low reduced frequency implies that the wake is distributed over several hundred airfoil chord lengths, thus requiring a very large computational domain. In order to contain the cost of the simulation, attempts were made with meshes containing no more than half a million mesh points. This mesh number requirement, coupled with the lengthy computational domain, resulted in a streamwise mesh spacing that proved to be too coarse, especially in the regions of the intermediate to far wake. Numerical dissipation on the coarse mesh resulted in a loss in circulation in the wake, which is in violation of Kelvin’s law. Loss of circulation also incorrectly removed the influence of the wake on the lift and drag, which rendered the calculations of limited value. Gridpoint estimates for an adequate mesh were in the neighborhood of 4 million, which could not be accomplished in a reasonable amount of time.

In order to provide an indication of the behavior of partially stalled wings, a literature survey on experimental measurements was conducted. While much of the literature is for relatively high reduced frequencies, one reference was found where measurements of pitching, stalled, and unstalled wings at a variety of reduced frequencies was reported (Ref. 8). In this work, Aihara *et al.* report a general trend where the flow is increasingly displaced from equilibrium as the reduced frequency is increased. At the higher reduced frequencies, and especially for angles of attack exceeding stall, the flow was far from equilibrium at the end of the pitch change maneuver and required a relaxation period equal to the time required for the airfoil to travel 10–20 chord lengths in order to reach steady state. At low reduced frequencies, the behavior was found to be rather different with the lift and drag remaining close to their quasi-steady values throughout the pitch change maneuver, irrespective of whether the wing experiences stall. In these cases, there is almost no visible relaxation period, and Aihara *et al.* consider the flow to be quasi-steady for reduced frequencies below approximately $1.0 \cdot 10^{-2}$. Equation (9) indicates that a model with a 1.65 ft (0.50 m) chord traveling at Mach 0.2 and pitched through 20 degrees will result in a reduced frequency of $2.5 \cdot 10^{-4}$ or a factor of 40 less than what Aihara *et al.* report is required for quasi-steady flow. Based on these findings, it is expected that the presence of stall in the angle of attack sweep will not result in a significant deviation from the data reported in Figures 39 and 40.

Background Disturbance Levels

At the conclusion of a test, the tunnel will be filled with turbulence generated by the wake of the model, support system, and cart. In addition, starting, stopping, and wing-tip vortices will be present in the tunnel. The vortices are expected to remain intact for approximately 1 minute before they breakdown into additional turbulence. The turbulence will decay in time under the action of viscosity and a “hold period” must be imposed in order to allow the turbulence to subside to acceptable levels prior to initiating another run. If the hold period is greater than the time required to recool the tunnel, recharge the batteries, and reset the instrumentation, the productivity of the facility is compromised.

Vortex Break-Up Time. The lifespan of aircraft-generated trailing vortices in free air has been studied extensively in the past. In the absence of strong atmospheric turbulence or other external forcing mechanisms, the vortex pair remains intact for a short period before a weak, naturally occurring instability leads to its breakdown. Both analysis and observations suggest that this time is between 1 and 2 minutes in most cases (Ref. 9). It shall be assumed that the vortices undergo a similar instability in the tunnel and last up to 2 minutes before breaking down into turbulence.

Decay of the Residual Turbulence. Aside from the regions close to the wind tunnel walls, the turbulence in the HiLiFT facility will be nearly homogeneous. The decay of homogeneous turbulence has been studied rather extensively, and the process is reasonably well understood. According to Hinze (Ref. 10), the decay is governed by the following power law:

$$\frac{u'}{u'_0} = \left(\frac{1}{1 + k \left(\frac{u'_0 t}{D} \right)} \right)^{n/2} \quad (12)$$

where the constant k is close to 2 and the exponent n can be taken as 1.4. The initial turbulence level u'_0 was estimated by assuming that the work done on the fluid by the drag force is converted entirely into turbulent kinetic energy. The drag coefficient for the cart and model support system was estimated to be

0.324 based on an area $S=42.3 \text{ ft}^2$ (3.93 m^2). This drag coefficient gives the initial turbulence level as $u'_0=0.242U$.

The above initial value for the turbulent velocity fluctuation is used in Eq. (11) together with $k=2$ and $n=1.4$ to generate the data in Figure 41. The relative turbulence levels are higher in the $M=0.05$ case since the model speed used as the normalizing velocity scale is lower. For the $M=0.05$ case, the residual turbulence is below 1% of the free-stream value after 2 minutes. From that point, the decay is rather slow; approximately one hour is required to reduce the level to 0.1%, and nearly one day is required to lower it to 0.01%. The 0.005% level specified in the HiLiFT Requirements Document is achieved after approximately 2.5 days. The $M=0.5$ case is better, with the 1%, 0.1%, and 0.01% turbulence levels occurring at less than 1 minute, 5 minutes, and 2 hours, respectively. The required 0.005% level is achieved after approximately 6 hours.

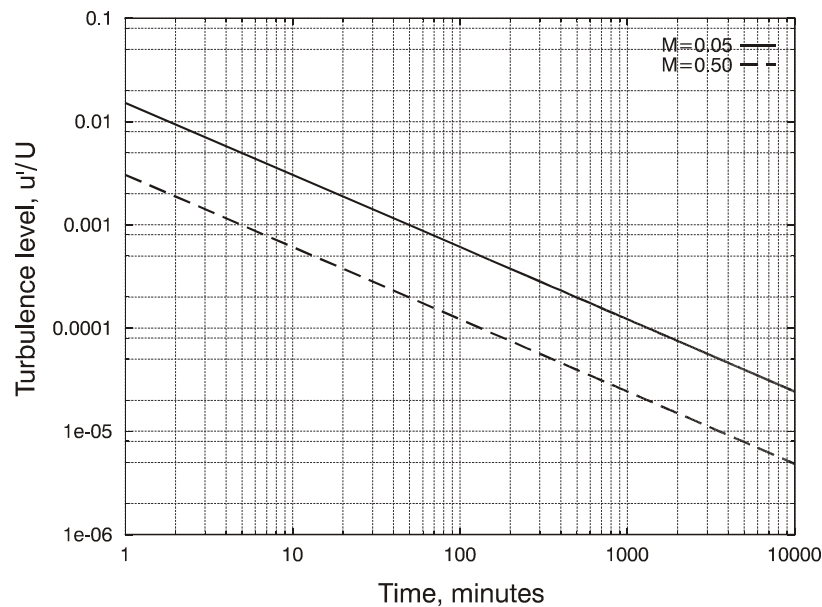


Figure 41. Decay of residual turbulence between runs.

While the initial decay is quite fast, the asymptotic approach to quiescent conditions is rather slow. Since it appears impractical to meet the specified 0.005% turbulence level, it is reasonable to question whether this is a realistic requirement. For the $M=0.05$ case, a 0.005% turbulence level translates into a velocity fluctuation of approximately 1 in per minute (2.54 cm/min). It is likely that convection currents set up by temperature nonuniformities in the tunnel will be much larger than this. One can also compare the 0.005% turbulence requirement with the disturbances found in the atmosphere. Turbulent gusts near the earth's surface can easily produce velocity variations of 2 mi/hr (0.89 m/s). For an aircraft traveling at 200 mi/hr (89 m/s), this gives a relative turbulence level of 1%. For the same 200 mi/hr (89 m/s) aircraft speed, a disturbance velocity of just 0.18 in/s (0.46 cm/s) exceeds the 0.005% disturbance level. Again, buoyant convection currents are expected to exceed this value even for flight outside the planetary boundary layer.

If one adopts a perhaps more realistic 0.5% turbulence level, the situation looks much better. The $M=0.5$ case will require about a minute of settling time, whereas the $M=0.05$ case will take approximately

5 minutes. For a 0.1% turbulence level, the times increase to 5 and 50 minutes respectively. In order to avoid long hold times for the low Mach number runs, it is possible to schedule a sequence of runs with increasing Mach number. In this way, the normalizing velocity increases with each run, which effectively reduces the time that one must wait for the turbulence to decay to the desired level.

Thermal Analyses

Selection of Insulation

Various insulation types were investigated as to advantages and disadvantages for the proposed application. Nonvacuum and vacuum-type insulations were considered. Nonvacuum insulations, which include expanded foams (either open-cell or closed-cell) and other materials such as powders or fibrous materials, operate at ambient pressure. Vacuum insulations operate at reduced pressure and require a void be maintained to minimize conductive/convective heat transfer; the void can be filled with powder/fibrous materials or with multiple layers of reflective material to provide improved insulating value. Vacuum insulations are capable of much higher performance than nonvacuum types, though at much increased complexity and cost.

It was determined that foam would be the best choice because it is simple, reliable, robust, and inexpensive. A vacuum-type insulation, which would be extremely costly for such a large vessel, is unnecessary. A decision was made to use Foamglas (a closed-cell foam insulation) because it is impervious to moisture (unlike other foams such as polyurethane) and has a coefficient of thermal expansion close to that of stainless steel. The main disadvantage of Foamglas is that it is fairly dense compared to other foams [8 lb/ft³ (128 kg/m³) vs. 2-to-5 lb/ft³ (32-to-80 kg/m³)]; however, it was thought that the simplicity, durability, and overall robustness of the Foamglas made it preferable.

A simple analysis was performed to trade off the capital cost of foam insulation vs. liquid nitrogen consumption as a function of insulation thickness from 0.5 to 10 ft (0.15 to 3.0 m) for various tunnel diameters. The assumptions made for this analysis were 1) capital cost of the insulation of \$11.60/ft³ (\$409.65/m³); 2) liquid nitrogen cost of \$0.50/gallon (\$0.13/liter); 3) inner temperature -250 °F (-157 °C), outer temperature 100 °F (38 °C); and 4) the tunnel was maintained at -250 °F (-157 °C) for 50% of its operating life of 20 years. The total cost was simply the sum of capital cost of the insulation plus the nitrogen cost over 20 years. No other component, such as maintenance, was included, and no time value of money factors were considered. The results are shown in Figure 42. The minimum overall cost exists at an insulation thickness of between 4 and 6 ft (1.2 and 1.8 m). After considering other issues, particularly ease of installation and uncertainty of operational time at low temperature, a design thickness of 3 ft (0.9 m) was chosen. Three ft (0.9 m) is just beyond the “knee in the curve” and using thicker insulation would not result in a significant reduction in heat load.

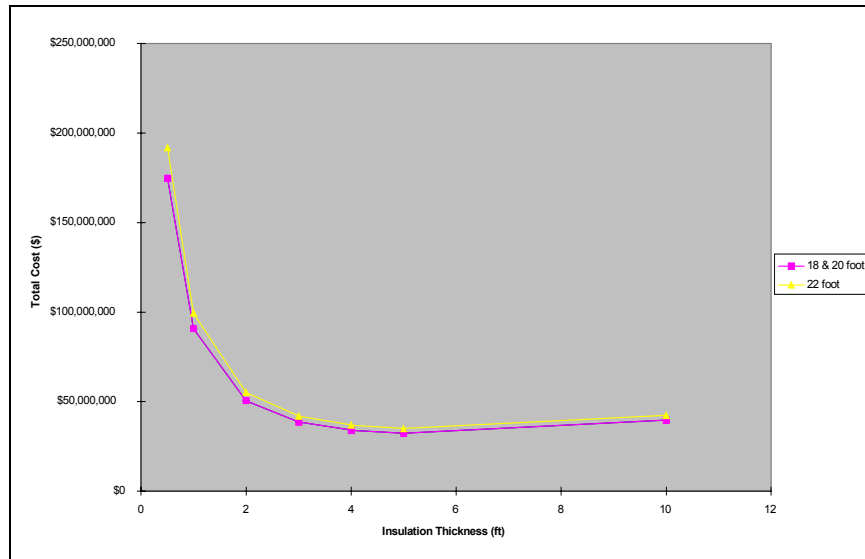


Figure 42. Total insulation capital cost plus nitrogen consumption costs for 20-year HiLiFT tunnel life (multiple tunnel diameters).

Free Convection

Computational fluid dynamics (CFD) simulations of the free convection flowfield, as well as temperature distribution at a cross-section of the tunnel using boundary conditions generated by heat transfer simulations of the overall tunnel and insulation, were completed. The heat transfer simulations were performed at steady-state conditions to estimate the circumferential temperature gradient set up in the tunnel wall for various insulation thicknesses and thermal conductivities, with the internal bulk gas temperature constrained to $-250\text{ }^{\circ}\text{F}$ ($-157\text{ }^{\circ}\text{C}$). If the gas within the tunnel is not mixed periodically, circumferential temperature gradients would arise over time due to the effect of geometry on free convection heat transfer. The steady-state temperature gradients produced by the thermal analyses were then imposed as temperature boundary conditions to the CFD analyses. For information, the predicted temperatures used as boundary conditions were approximately $-250\text{ }^{\circ}\text{F}$ ($-157\text{ }^{\circ}\text{C}$) for the sides and bottom surfaces of the tunnel and $-244.6\text{ }^{\circ}\text{F}$ for the tunnel top surface.

Figure 43 shows a steady-state CFD simulation for a 30-ft (9.1 m) diameter tunnel with 3 ft (0.91 m) of foam insulation at 5 atm pressure, with the temperature boundary conditions from thermal analyses imposed on the tunnel wall. These simulations showed a maximum transverse velocity in the core of the tunnel of 0.51 ft/s (0.16 m/s) and a maximum temperature nonuniformity in the core of the tunnel of $0.25\text{ }^{\circ}\text{F}$ ($0.14\text{ }^{\circ}\text{C}$). A maximum transverse velocity of 0.51 ft/s (0.16 m/s) is greater than the allowable value since it would cause angle of attack errors greater than 0.01 degree. However, such a low transverse velocity is at or beyond the capability of CFD to predict reliably, especially for such a low-viscosity fluid. In addition, the assumption of steady state conditions is probably not met. This analysis was performed when the baseline tunnel design was a 30-ft (9.1 m) diameter with a maximum design pressure of 5 atm (0.50 MPa). While the final tunnel design included a 20-ft (6.1-m)- diameter tunnel with a maximum pressure of 7.5 atm (.76 MPa), this analysis was not repeated for those conditions because the result was not expected to change noticeably.

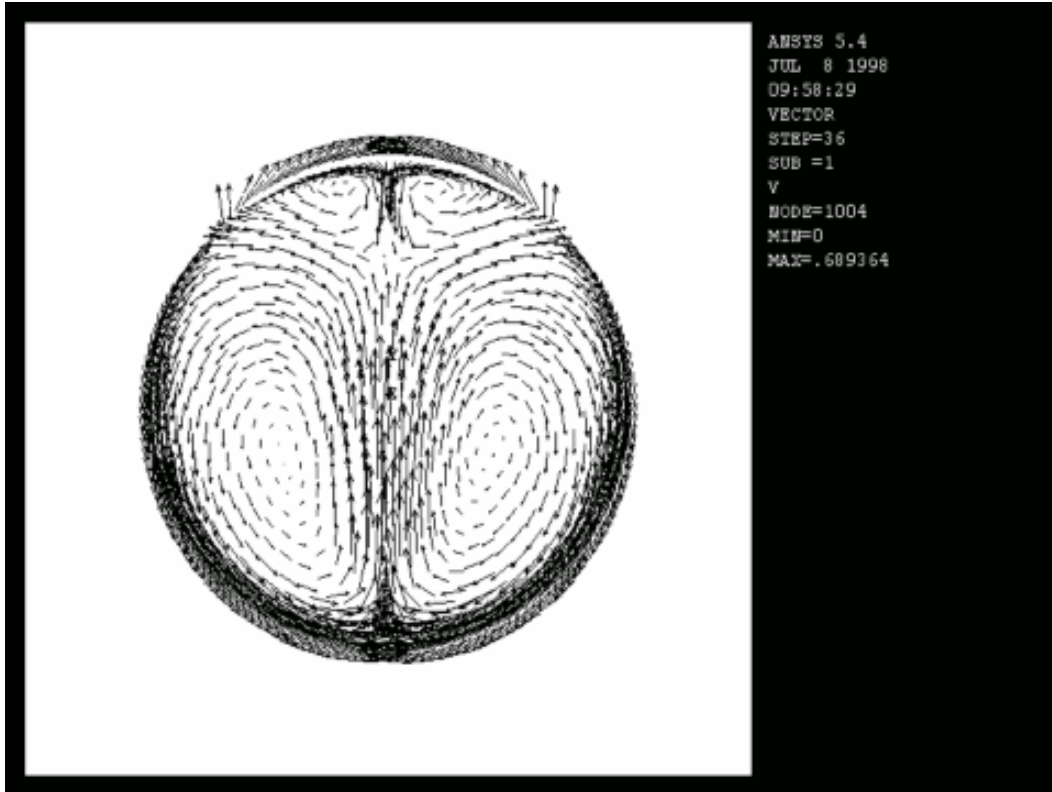


Figure 43. Equilibrium free convection velocity distribution for HiLiFT tunnel, 3 ft (0.91 m) of foam insulation [maximum velocity is 0.69 ft/s (0.21 m/s), max velocity in middle 80% of tunnel is 0.51ft/s (0.16 m/s)].

Free convection heat transfer is produced by having a relatively still environment with the convection currents generated by the effects of gravity and geometry on the density gradients set up in the fluid. When actual operation of the tunnel is considered, several things become apparent. First, the tunnel will never be at true steady-state conditions. The nitrogen conditioning system will be injecting nitrogen as required to maintain the temperature set point, which will serve to stir up the tunnel internal environment. Second, when testing is underway (which is the only time that temperature uniformity and transverse velocities matter), the internal environment will be thoroughly mixed every time the test model is sent down the tunnel. The effect of these will be to provide a fairly well-mixed gas environment inside the tunnel that will prevent a significant circumferential temperature gradient in the tunnel shell from being set up. A circumferential gradient is needed to set up a free convection flowfield.

Transient modeling of the flowfield in the tunnel during operation is extremely difficult. The flows set up by injection of nitrogen into the tunnel is complicated by the boiling of liquid nitrogen into the gaseous phase, and the stirring up and turbulence decay of the tunnel due to model passage is also extremely complicated. Efforts were made to quantify the transient development of free convection currents from an initial condition of no circumferential gradient using the CFD FLOTRAN module of ANSYS®. These efforts were unsuccessful due to the extremely low viscosity and high density of the tunnel medium.

A transient heat transfer simulation of the tunnel shell from an initial condition of total uniformity (i.e., no circumferential temperature gradient) was performed. Figure 44 shows the length of time it takes for a

circumferential gradient to appear with no mixing due to nitrogen injection or model passage. It should be noted that this only predicts how long it takes for a temperature gradient to appear; it would be some time afterward that a well-developed free convection pattern develops.

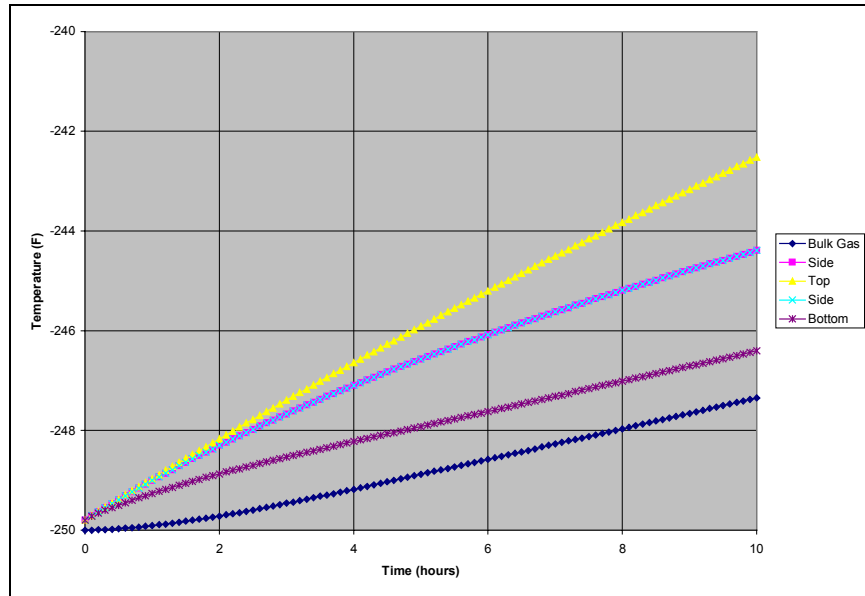


Figure 44. Predicted temperatures of bulk gas and tunnel top/sides/bottom from uniform initial condition of $-250\text{ }^{\circ}\text{F}$ ($-157\text{ }^{\circ}\text{C}$).

Cooldown Simulations

Originally, it was assumed that a gaseous nitrogen injection system would be necessary to provide the required uniformity and temperature control of the tunnel. In this system, the gaseous nitrogen would be recycled to a heat exchange system, where the gaseous nitrogen would be cooled to the desired delivery system by heat exchange with liquid nitrogen. Later analysis indicated that the heat exchange systems would be expensive and that direct injection of small amounts of liquid nitrogen (LN_2) would be preferable. This revised system was evaluated in light of having acoustic-damping material on the inner surface of the tunnel, which acts as a thermal insulator.

Initially, a scheme where liquid nitrogen is injected directly into the bulk tunnel cavity was evaluated. Large temperature gradients in the tunnel shell were set up between the bottom and top areas of the tunnel with gradients as large as $300\text{ }^{\circ}\text{F}$ ($167\text{ }^{\circ}\text{C}$) predicted, as shown in Figure 45. The exposed bottom area of the tunnel responded very quickly; however, the surfaces behind the acoustic insulation responded more slowly with the top responding the slowest. Flow rate was not a significant effect due to most of the tunnel being behind the acoustic insulation. The stresses induced by the large circumferential temperature gradients were evaluated and found to be excessive, and this conditioning approach was abandoned.

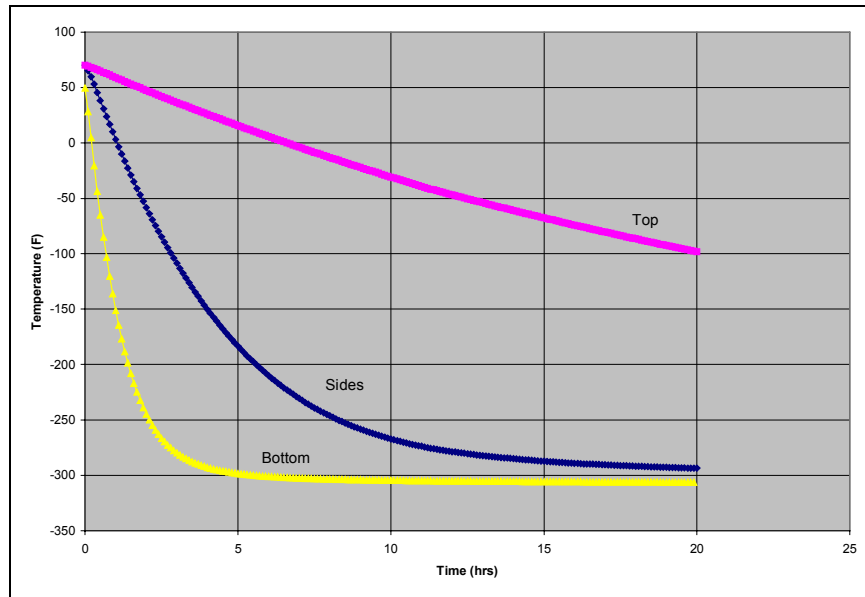


Figure 45. Tunnel shell components cooldown, LN₂ injection into bulk tunnel gas, 950,000 lb/hr (430,000 kg/hr), 2 atm (0.2 MPa) pressure.

The next approach evaluated was the injection of liquid nitrogen behind the acoustic insulation. This would provide direct conditioning of the tunnel shell that would allow more uniform and rapid cooldown of the entire tunnel. A thermal model was constructed for this scenario in which liquid nitrogen was injected between the acoustic insulation and tunnel shell at distributed intervals along the tunnel length. Based upon results from the previous section of this report, it is apparent that injection of the liquid nitrogen should be at least somewhat circumferentially distributed to keep temperature gradients manageable (i.e., injecting liquid nitrogen at only one circumferential location would “quench” the local area, while the remainder of the tunnel area would lag far behind in temperature).

The thermal model simulated injection of liquid nitrogen at the top of the tunnel and midway around both sides of the tunnel, distributed along the tunnel length with the bottom of the tunnel (being uncovered by acoustic insulation) conditioned by the nitrogen in the bulk tunnel cavity. The nitrogen injected into the tunnel flows lengthwise down the tunnel and exits at the tunnel end. The model was run for total nitrogen injection rates of 200,000 lb/hr (90,700 kg/hr) and 400,000 lb/hr (181,400 kg/hr), which correspond to total liquid nitrogen volumetric flow rates of 500 gallons per minute (gpm) (1,893 liter/min) and 1,000 gpm (3,785 liter/min), respectively.

The rail masses were the slowest-responding component of the system. At a total nitrogen flow rate of 200,000 lb/hr (90,700 kg/hr), the mass reaches $-250\text{ }^{\circ}\text{F}$ ($-157\text{ }^{\circ}\text{C}$) after approximately 11 hours (see Figure 46); while at the higher flow rate of 400,000 lb/hr (181,400 kg/hr), it takes approximately 7 hours (see Figure 47). The predicted circumferential temperature gradient halfway between the midpoint and end of the tunnel for the two flow rates is predicted to be fairly severe [on the order of $200\text{ }^{\circ}\text{F}$ ($111\text{ }^{\circ}\text{C}$) to $250\text{ }^{\circ}\text{F}$ ($-157\text{ }^{\circ}\text{C}$)]. This is partially due to the top and sides being “quenched” with liquid nitrogen, while the bottom receives no directed conditioning and partially due to how the system was modeled. The bottom of the tunnel (and the added mass of the rails and support rings) are modeled as convecting to the mixed bulk tunnel gas. In reality, buoyancy effects set up by injecting liquid (which boils to gas in cooling the tunnel) should cause the cold gas to rapidly sink to the bottom of the tunnel and remain there

with some potential stratification in the bulk tunnel gas. Therefore, the bottom of the tunnel should cool faster than shown since it will be convecting to colder gas than the bulk tunnel gas. If the HiLiFT tunnel concept is further developed, more detailed modeling is required to assess this effect. If at that time it appears that circumferential gradients will still be excessive, the problem can easily be solved by providing some directed conditioning to the bottom of the tunnel, as well as the sides and top. This would not require additional nitrogen; the distribution would simply be changed so that less is directed to the sides and top with the difference directed into the tunnel bottom area.

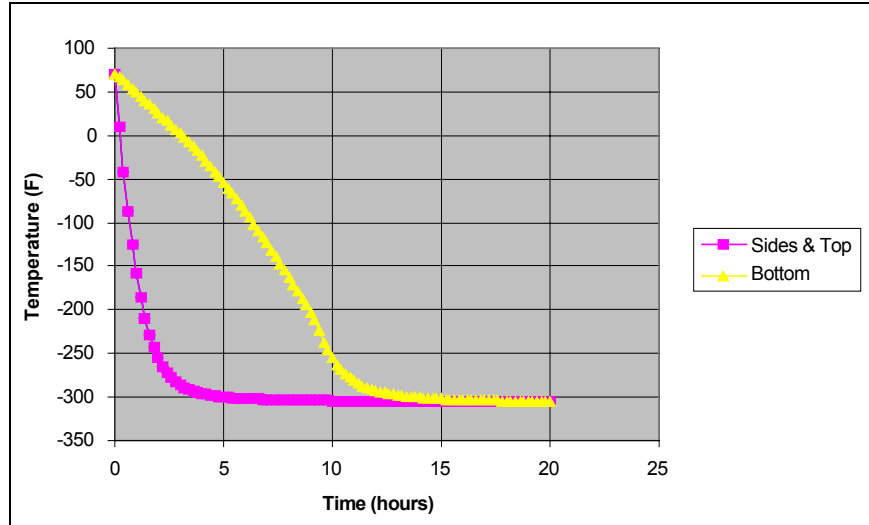


Figure 46. Predicted circumferential tunnel cooldown temperatures, LN₂ injected behind acoustic insulation, 200,000 lb/hr (90,700 kg/hr) total nitrogen flow.

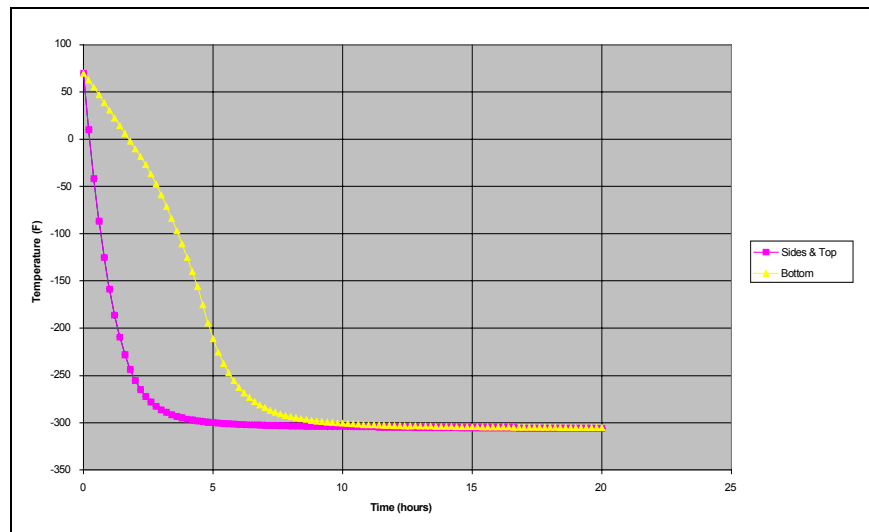


Figure 47. Predicted circumferential tunnel cooldown temperatures, LN₂ injected behind acoustic insulation, 400,000 lb/hr (181,400 kg/hr) total nitrogen flow.

Set Point Simulation

The previous sections have shown that the acoustic insulation is a major factor in controlling the tunnel gas and shell temperatures. It was shown that conditioning of the shell directly behind the acoustic insulation was required to rapidly and uniformly cool the tunnel. A different situation arises when the tunnel is at its set point, and the goal is simply to maintain the set point. In that situation, liquid nitrogen injection directly into the main tunnel volume is the best way to control the tunnel gas temperature. Injecting it behind the acoustic insulation would not provide adequate control of the tunnel gas environment.

A thermal model was not constructed because the tunnel temperature gradients were expected to be negligible. In addition, the sporadic nature of the injected nitrogen flow combined with the frequent violent mixing occurring in the tunnel due to model passage complicate the analytical approach. Sufficient amounts of nitrogen need only be injected to offset the small heat load conducting into the tunnel through the insulation system and to offset the heat generated by the propulsion system. A simple calculation shows that for a conductive heat gain by the tunnel of 435,000 British thermal unit (Btu)/hr [127 kilowatts (kW)] and saturated liquid nitrogen injected at 7.5 atm (0.76 MPa) pressure, a total flow rate of 4,600 lb/hr (2,090 kg/hr) [approximately 11.5 gpm (45.5 liter/min)] of nitrogen would be required, and this would be distributed evenly along the length of the tunnel. The heat generated by the model/cart propulsion system would be a function of the model/cart mass and the desired acceleration/ deceleration rate. This heat input has been estimated at approximately 25 megajoules (MJ) per run, and the desired frequency of testing has been set at 8 runs per hour. The amount of liquid nitrogen needed to offset this heat gain would be approximately 2,000 lb/hr (907 kg/hr) [approximately 5 gpm (19 liter/min)]. This nitrogen should be injected uniformly in the portions of the tunnel in which the heat is generated (i.e., where the model/cart are being accelerated/ decelerated). The nitrogen requirements to offset conductive heat gains at higher temperatures, lower model/cart masses, or lower acceleration/deceleration rates would be lower.

Structural Supports

The structural supports for the tunnel represent potentially large localized heat inputs to the system that could disrupt the gas environment due to localized free convection effects. This heat load would be eliminated by surrounding the supports in 6 in (15 cm) of polyurethane foam and delivering a small liquid nitrogen flow to each support. The total required flow would be approximately 900 lb/hr (408 kg/hr) when maintaining a set point at $-250\text{ }^{\circ}\text{F}$ ($-157\text{ }^{\circ}\text{C}$). This flow would be significantly increased when cooling to achieve a rapid cooldown rate.

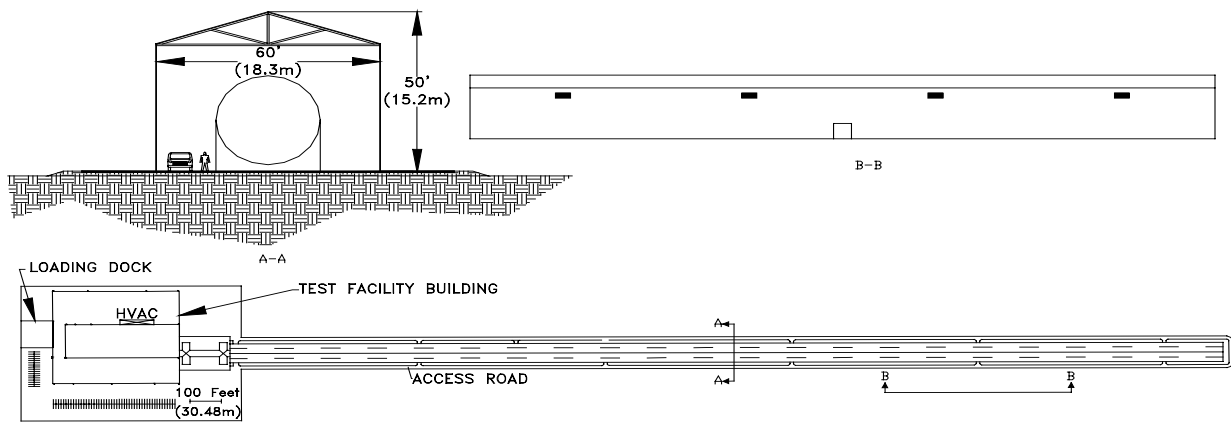
Infrastructure Design

Buildings and Grounds

The HiLiFT facility will consist of a 136,000-ft² (12,600-m²) first floor with a 45,000-ft² (4,200 m²) second floor for customer support. Various services will be available including a welding shop, machine shop, warehouse and shipping department, instrumentation and control (I&C) and calibration laboratory, and storage facilities. General office space, a control room, a lunchroom, and restrooms are available to support general operations and testing. A guardroom is present to allow controlled access and security.

Models will be assembled in customer model shops and attached to the cart sting. Each model bay has a roll-up door for access to the cart alley. There are three dedicated model shops with customer office space to provide customers with security.

Grounds will consist of a combination of paved lots, paved access roads, and landscaped areas. The area surrounding the facility will be paved for personnel parking, loading and unloading of shipping trucks, and outdoor storage. A building system to protect the tunnel from the weather is also included. This building will consist of sections of preengineered buildings connected to form a complete building system over the tunnel sections. The building system will have garage-type doors installed at intervals along its length to allow entrance for maintenance and inspection. Additionally, access roads for inspection and maintenance access to the tunnel are planned. An overview of the HiLiFT facility is shown in Figure 48.



MS TA, INC.
 ACAD# NAH60310
 REV: - 3/23/00
 DRAFTER: KJBS

Figure 48. Overall HiLiFT Facility general arrangement.

Electrical

The power to the HiLiFT facility will be provided by utility company high voltage transmission line [approximately 360 amp at 161 kV will be required]. A 100 MW substation will be required. It is assumed that the facility will be constructed in close proximity to an existing high-voltage transmission line, and the utility company is able to serve a pulsed-power load of this magnitude (80 MW). If the utility cannot serve such a load, there would be additional cost involved in the design and construction of an energy storage device to convert the pulsed-power load to a load appearing to be continuous to the serving utility. Construction of an energy storage device would offer a cost tradeoff because the size of the substation could be reduced to approximately 25 MW.

A 12.5 kV, 5,000 amp oil circuit breaker and associated relaying on the secondary side of the 161/12.5 kV transformer will provide ground fault, short circuit as well as operating overcurrent

protection. This will feed four pieces of 12.5 kV switchgear as described in Table 11 and depicted in Figure 49.

Table 11. Major 12.5 kV Switchgear Required And Loads Served

#	Specification	Load
2	4,000 amp	80 MW LSM power supplies
1	250 amp for 5 MVA 122 kV to 480/277 V transformer	Tunnel warmup heaters
1	100 amp for 2 MVA 122 kV to 480/277 V transformer	Facility lighting/general

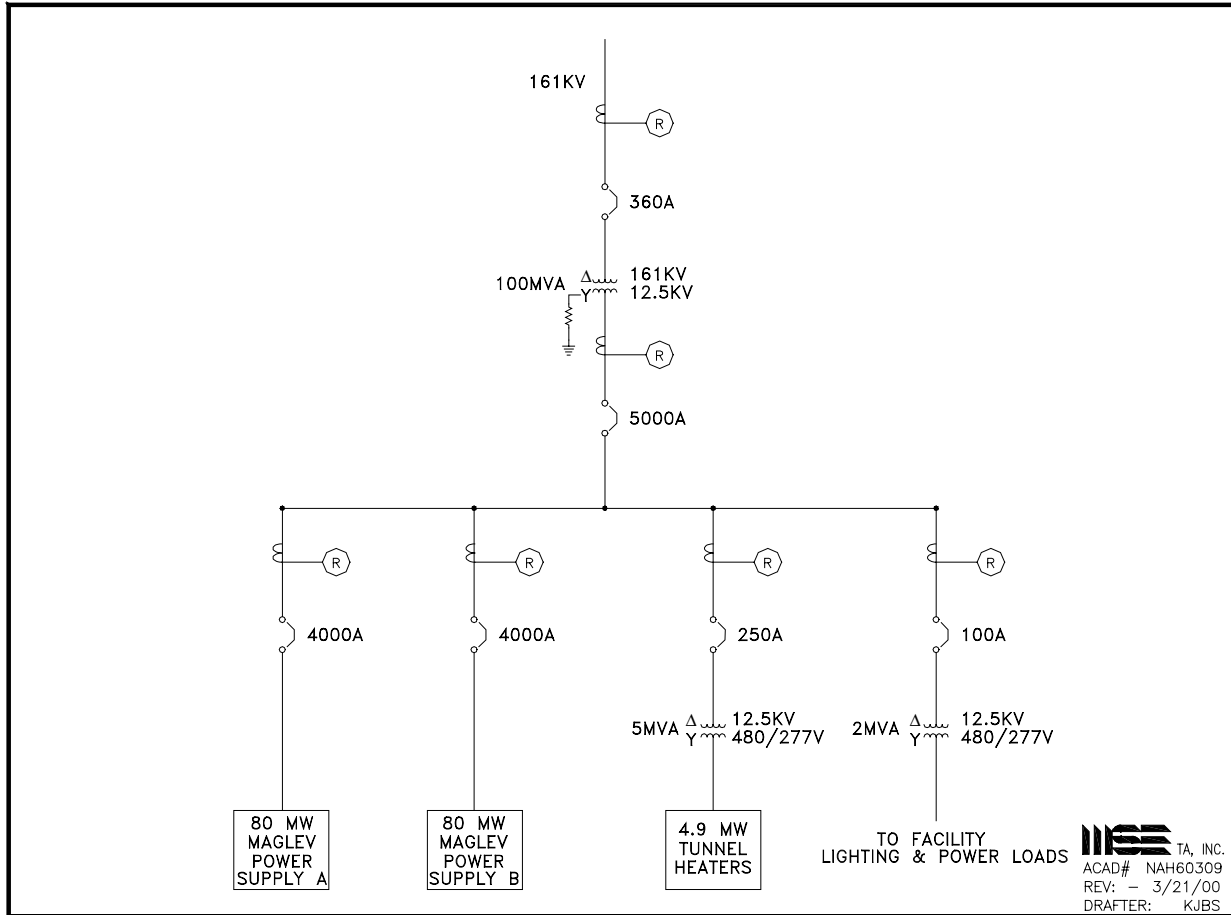


Figure 49. HiLiFT electrical system 1-line diagram.

Nitrogen System

A liquid nitrogen truck offloading system will consist of four truck stations. In addition, a liquid nitrogen pipeline connects the storage tank with a possible cryogenic nitrogen production facility. Two liquid nitrogen storage tanks provide liquid nitrogen supply for tunnel cooldown and model cart cooldown. Two run tanks provide liquid nitrogen to absorb heat gained in the tunnel by leakage through the thermal insulation and heat generated by model cart runs. One tank is used until it is emptied. The system is then shifted to the second tank while the first is refilled from the storage tanks.

The nitrogen dispensing system includes two 477 gpm (1,800 l/min) pumps drawing from the storage tanks for tunnel and model cart cooling, plus two 10 gpm (38 l/min) pumps drawing from the run tanks for heat compensation. liquid nitrogen flow during cooldown is evenly distributed along the tunnel and injected in 125 locations. During operation, liquid nitrogen is supplied using the same pipeline but different injectors to recool the tunnel.

Nitrogen gas exhausted from the tunnel during depressurizations or warmups is placed into a 120-ft (36.6 m)- tall stack to avoid the possibility of creating a suffocation or freezing hazard at ground level. Air is blown into the stack from the bottom during these events to help warm and dilute the cold nitrogen. Electrical resistance heaters will be placed in close proximity to the tunnel shell to assist in warming the tunnel uniformly and relatively rapidly.

A simplified process flow diagram of the nitrogen system is shown in Figure 50.

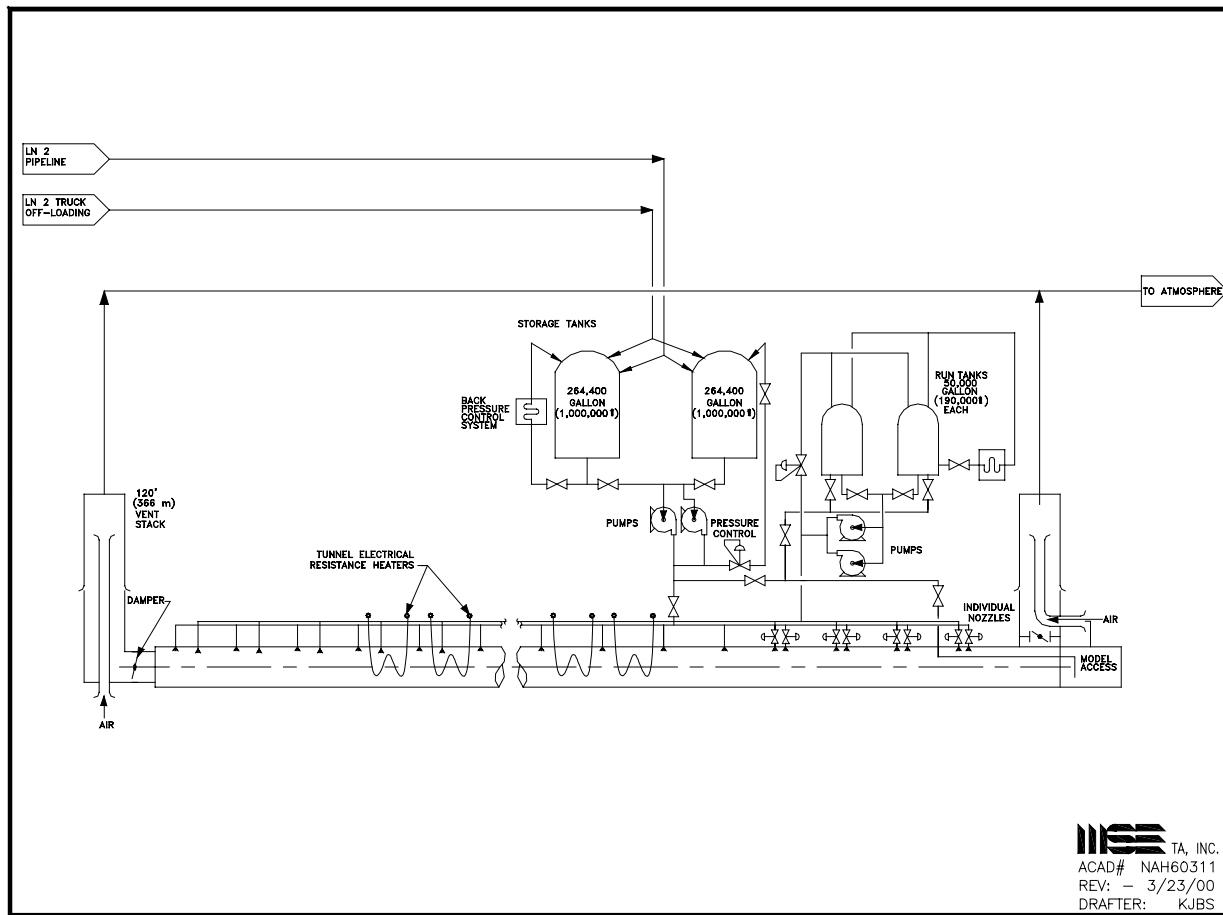


Figure 50. Nitrogen system process flow diagram.

Data Quality

Five data quality requirements were given for the HiLiFT performance:

- Coefficient of drag (C_D) must be corrected to within 0.0005 at Mach 0.3;
- Coefficient of lift (C_L) must be corrected to within 0.005 at Mach 0.3;
- Angle of attack (pitch angle) error must be corrected to within ± 0.01 degree;
- Roll angle error must be corrected to within ± 0.01 degree; and
- Yaw angle error must be corrected to within ± 0.02 degree.

These were analyzed by grouping C_D and C_L and grouping pitch, roll, and yaw errors.

Coefficients of Lift and Drag

For simplicity, the errors associated with coefficient of lift and drag were divided into two categories. The first category was termed free-stream errors or those errors associated with the bulk properties of the test medium. The second category was termed non-free-stream errors or those errors associated with the confining effects of the tunnel walls.

Free-Stream Errors. For free-stream errors, the following equations were derived (see Ref. 2):

$$\begin{aligned}\frac{\epsilon_{C_D}}{C_D} &= \left[\frac{\epsilon_T}{T} + \frac{\epsilon_P}{P} + 2 \frac{\epsilon_V}{V} \right] \\ \frac{\epsilon_{C_L}}{C_L} &= \left[\frac{\epsilon_T}{T} + \frac{\epsilon_P}{P} + 2 \frac{\epsilon_V}{V} \right]\end{aligned}\tag{13}$$

where T is temperature, P is pressure, V is velocity, C_D is the coefficient of drag, C_L is the coefficient of lift, and ϵ represents an error value resulting from any of a number of different sources for the measurement of the respective quantity.

Substituting $\epsilon_{C_D}=0.0005$ and $C_D=0.25$ gives:

$$\frac{\epsilon_{C_D}}{C_D} = \frac{0.0005}{0.25} = 0.002 = 0.2\% = \left[\frac{\epsilon_T}{T} + \frac{\epsilon_P}{P} + 2 \frac{\epsilon_V}{V} \right]\tag{14}$$

Substituting $\epsilon_{C_L}=0.005$ and $C_L=2.5$ gives:

$$\frac{\epsilon_{C_L}}{C_L} = \frac{0.005}{2.5} = 0.002 = 0.2\% = \left[\frac{\epsilon_T}{T} + \frac{\epsilon_P}{P} + 2 \frac{\epsilon_V}{V} \right]\tag{15}$$

which is the same result as before.

Using this relationship between the error in the coefficients of lift and drag and the errors in temperature, pressure, and velocity, the maximum allowable error in the free-stream measurements can be determined. This is done by assuming that each variable by itself contributes the entire error in C_D . The results of this computation, for both lift and drag, show that the maximum allowable temperature, pressure, and velocity errors considered one at a time are:

$$\begin{aligned}\varepsilon_T &= 0.233^\circ C \\ \varepsilon_P &= 1520Pa \\ \varepsilon_V &= 0.06 \frac{m}{s}.\end{aligned}\tag{16}$$

Since temperature, pressure, and velocity are measured quantities, the error contributions from each of these sources is simply the measurement error associated with each of these quantities. The approach to minimizing these free-stream errors is described in Table 12.

Table 12. Coefficient Of Drag/Coefficient Of Lift Error Sources From Free-Stream And Non-Free-Stream Effects And Approach To Mitigating Them

Area	Type	Topic	Approach
Temperature	Free-stream	Require close tolerance temperature measuring system for tunnel temperature measurements	Locate manufacturer of precision temperature measurement systems and incorporate into design
	Non-free-stream	Need to eliminate “pockets” of warm or cool nitrogen	Complete detailed analysis and supplement with scaled testing as required
Pressure	Free-stream	Require close tolerance pressure sensor	Locate manufacturer of precision pressure measurement device and incorporate into design
	Non-free-stream	Eliminate acoustic waves	Locate manufacturer of low frequency energy absorption devices, incorporate into design, and reanalyze to ensure requirements are met
Velocity	Free-stream	Require close tolerance velocity measurements	Determine if inherent maglev system accuracy is sufficient, if not locate manufacturer of precision velocity measurement device and incorporate into design
	Non-free-stream	Verify turbulence has insignificant effect on measurements	Confirm analysis results
	Non-free-stream	Minimize effect of flow acceleration due to model	Determine correction factor algorithm
Aerodynamic	Non-free-stream	Minimize effect of twist on wing due to walls, support, and cart	Determine correction factor algorithm
	Non-free-stream	Minimize flow establishment time to maximize test time	Determine correction factor algorithm
	Non-free-stream	Minimize effect of continuous pitch change on data validity	Determine correction factor algorithm

The error introduced in Mach number (and hence C_D and C_L) due to impurities in nitrogen was analyzed and is believed to be a negligible contributor.

Non-Free-Stream Errors. Eight non-free-stream effects have been identified that may cause errors in the determination of the coefficients of lift and drag including three that should be able to be controlled with appropriate design:

- Small “pockets” of nitrogen gas that are either warmer or cooler than the bulk gas may affect the measurement of C_D and C_L as the model passes through them. With the periodic stirring of the tunnel fluid, these pockets are expected to be small but will require careful analysis and probably experimental testing to determine the extent to which the tunnel can be controlled to a uniform temperature and the real effect of small regions of warmer or cooler gas on C_D and C_L measurements.
- Axial velocity vectors due to turbulence that has not had sufficient time to return to a quiescent state can cause local variations in the measurements of C_D and C_L . With test cycle times on the order of 7.5 minutes, the turbulence is expected to be in small enough regions with low enough energies that no effect on the measurements will be felt, but this needs to be confirmed through additional analysis.
- Pressure disturbances in the form of acoustic waves traveling between the tunnel end walls could have a significant effect on the measurements. This will be mitigated by placing a low frequency energy absorbing material on the tunnel end walls.

The effects of four of the eight non-free-stream error sources will be removed by posttest data processing using error correction algorithms. These include:

- Acceleration of the nitrogen surrounding the model caused by blockage of the tunnel diameter of the model, support, and cart will result in an increase in the axial velocity of the gas over the model from what would be expected due to measuring the velocity of the cart by itself.
- The relative nearness of the walls, cart, and support to the wing will cause an angle-of-attack twist to be induced on the wing, which would not occur in free flight.
- The time required for the flow to reach steady state after a period of acceleration (the “flow establishment time”) will limit the amount of test time available where the required data requirements can be met.
- When testing with a continuous pitch change, unsteady flow will result in limiting the rate of acceptable pitch change.

Finally, one non-free-stream error source is expected to be negligible.

- Buoyancy effects of the model in the working fluid (i.e., cryogenic nitrogen) will be present, but are expected to be sufficiently small that no correction will be needed.

The seven significant non-free-stream error sources and the approach to mitigating their effects are also listed in Table 12.

Pitch, Roll, and Yaw Errors

The error sources, source descriptions, and analyses for pitch, roll, and yaw errors are all quite similar. Nine sources were identified that could cause attitude errors and are shown in Table 13.

Table 13. Sources Of Attitude Error In Pitch, Roll, And Yaw

1	Thermally induced nitrogen velocity vectors
2	Random nitrogen velocity vectors (e.g., caused by decaying vortices)
3	Sting deflections
4	Cart deflections
5	Cart suspension system deflections
6	Rail and tunnel deflections
7	Tunnel support structure deflections
8	Tunnel support structure movement
9	Thermally induced tunnel support structure variations

The first error source, a velocity vector due to thermal convection, is not believed to contribute error since the thermal analysis showed that temperature differential (which is the driving force for convection currents) takes hours to form but cart runs are made every 7.5 minutes. The second error source, a velocity vector due to vortices, is not believed to contribute error because any turbulence will have decayed to small cells and it is assumed that the spatial averaging of the turbulence will result in effective cancellation.

All of the remaining error sources will be minimized through good design but will still result in excess deflection to meet the data quality objective. Therefore, the model attitude will be measured and thus error sources 3) through 9) will be effectively replaced with single measurement error for each of the three rotational axes. Although the required accuracy would not be a problem to measure statically, the dynamic motion of the model at the end of the sting will add significantly to the error. Based upon experience at existing wind tunnels, the dynamic error will be so large, even with correction schemes, as to not permit the design to satisfy the specification. However, this is an area of active research, and the HiLiFT facility will benefit from progress in this field. This analysis is summarized in Table 14.

Table 14. Angle Of Attack/Roll Angle/Yaw Angle Error Sources And Approach To Mitigating Them

Area	Topic	Approach
Nitrogen velocity	Verify turbulence has insignificant effect on measurements	Confirm analysis results
	Verify thermal convection currents have insignificant effect on measurements	Confirm analysis results
Sensors	Require angle of attack (pitch) sensor that meets required accuracy in the presence of dynamic environment	Stay aware of ongoing research in this field and extend it to project needs
	Require roll sensor that meets required accuracy in the presence of dynamic environment	Stay aware of ongoing research in this field and apply it to project needs
	Require yaw sensor that meets required accuracy in the presence of dynamic environment	Stay aware of ongoing research in this field and apply it to project needs

Operating Cost Analysis

Based upon the current design, costs in terms of gallons of liquid nitrogen (\$0.35/gallon or \$1.32/l) and kilowatt-hours (kW-hr) of electricity (\$0.06/kW-hr) were computed for various tunnel operations and are listed in Table 15.

Table 15. Rough-Order-Of-Magnitude Costs For Tunnel Operations

Rough-order-of-magnitude (ROM) costs for tunnel operations		
Operation	Consumable	ROM Cost
Tunnel cooldown to $-250\text{ }^{\circ}\text{F}$ ($-157\text{ }^{\circ}\text{C}$)	Nitrogen (550,000 gallons/2.08Mℓ)	\$192,500.00
Single run cooling @ $-250\text{ }^{\circ}\text{F}$ ($-157\text{ }^{\circ}\text{C}$)	Nitrogen (63.4 gallons/240ℓ)	\$22.19
Hour @ $-250\text{ }^{\circ}\text{F}$ ($-157\text{ }^{\circ}\text{C}$) w/o operation	Nitrogen (600 gallons/2.27kℓ)	\$210.00
Hour of supports cooling	Nitrogen (150 gallons/568ℓ)	\$52.50
Model cooldown to $-250\text{ }^{\circ}\text{F}$ ($-157\text{ }^{\circ}\text{C}$)	Nitrogen (13,500 gallons/51.1kℓ)	\$4,725.00
Single run, LSM power	Electricity (62.5 kW-hr)	\$3.75
Single run, battery recharge	Electricity (<4 kW-hr @ $\eta=0.25$)	<\$1.00
Tunnel warmup from $-250\text{ }^{\circ}\text{F}$ ($-157\text{ }^{\circ}\text{C}$)	Electricity (120 MW-hr)	\$7,200.00
Model warmup from $-250\text{ }^{\circ}\text{F}$ ($-157\text{ }^{\circ}\text{C}$)	Electricity (3 MW-hr)	\$180.00
Change from 1.5 to 3 atm (0.15 to 0.30 MPa) @ $-250\text{ }^{\circ}\text{F}$ ($-157\text{ }^{\circ}\text{C}$)	Nitrogen (35,072 gallons/133kℓ)	\$12,275.00
Change from 3 to 4.5 atm (0.30 to 0.46 MPa) @ $-250\text{ }^{\circ}\text{F}$ ($-157\text{ }^{\circ}\text{C}$)	Nitrogen (36,639 gallons/139kℓ)	\$12,824.00
Change from 4.5 to 6 atm (0.46 to 0.61 MPa) @ $-250\text{ }^{\circ}\text{F}$ ($-157\text{ }^{\circ}\text{C}$)	Nitrogen (38,359 gallons/145kℓ)	\$13,426.00
Change from 6 to 7.5 atm (0.61 to 0.76 MPa) @ $-250\text{ }^{\circ}\text{F}$ ($-157\text{ }^{\circ}\text{C}$)	Nitrogen (40,526 gallons/153kℓ)	\$14,184.00

From the data listed above and the length of estimated time to carry out each type of tunnel operation, the menu given in Table 16 was computed to enable determination of operational costs, both in terms of time and dollars. Some additional assumptions and simplifications were made:

- The average cost of a 1.5 atm (0.15 MPa) pressure change upward was determined by averaging the four values above to reach approximately \$13,200. Pressure changes downward are assumed to have zero cost. A 1.5 atm (0.15 MPa) change in either direction is assumed to take one-half hour.
- The total cost for a single run includes cooling (\$22.19), LSM power (\$3.75), and a battery recharge (\$1.00) for \$26.94.
- Runs are made every 7.5 minutes with 5 data points collected every run so that 20 data points are collected over 4 runs every one-half hour of data collection time. The cost for 20 data points in one-half hour is $\$26.94 \times 4 = \107.76 , which includes power (LSM and battery) and cooling due to the maglev system operation.
- The total cost to maintain a $-250\text{ }^{\circ}\text{F}$ ($-157\text{ }^{\circ}\text{C}$) tunnel temperature includes both tunnel (\$210/hr) and supports (\$52.50/hr) cooling for a total of \$262.50/hr. Four hours are required to make a model adjustment after the model has been warmed and removed from the tunnel.

Table 16. Table Of Operational Costs

Event	Cost	Time
Tunnel cooldown	\$192,500.00	10 hours
Tunnel warmup	\$7,200.00	10 hours
Pressure change upward	\$13,200.00	0.5 hour
Pressure change downward	0	0.5 hour
Collect 20 data points	\$107.76	0.5 hour
Model cooldown	\$4725.00	1 hour
Model warmup	\$180.00	1 hour
Model configuration change	0	4 hours
Tunnel and supports cooling per hour	\$262.50	1 hour

An example of an operational profile was created to allow an estimate of operational costs for a test program. For this purpose, all testing was assumed to be done at $-250\text{ }^{\circ}\text{F}$ ($-157\text{ }^{\circ}\text{C}$) while running 24 hours a day and 7 days a week.

The basic profile for a test program consists of the following:

1. The tunnel is cooled and pressurized while the air is replaced by nitrogen.
2. A data collection run is made.
3. The tunnel is recooled to remove the heat introduced by the run. If additional runs at these conditions are desired, return to 2), otherwise continue to 4).
4. The pressure is changed by injection of additional nitrogen or by bleeding off tunnel pressure. Return to 2) to collect data; or, if all desired pressure conditions are met, continue to 5).
5. The model and cart are moved to the interlock and warmed to ambient. Model modifications are made. The cart and model are placed into interlock and cooled to tunnel temperature. Return to 2) to collect data; or, if no more model modifications are needed, continue to 6).
6. The tunnel is warmed and depressurized while the nitrogen is replaced by air.

This process is shown pictorially in Figure 51. The selected test case included collection of 5,000 data points and includes a Reynolds number sweep, so the data can be correlated against other facilities.

For each model configuration, a 100-point data set is taken as follows:

- For a particular pressure, each data point is at a different angle of attack
- Each angle-of-attack sweep will go from -4 degrees to $+15$ degrees in 1 degree increments (20 data points)
- Collect 20 data points at Mach 0.27 and 1.5 atm (0.15 MPa)
- Collect 20 data points at Mach 0.27 and 3.0 atm (0.30 MPa)

- Collect 20 data points at Mach 0.27 and 4.5 atm (0.46 MPa)
- Collect 20 data points at Mach 0.27 and 6.0 atm (0.61 MPa)
- Collect 20 data points at Mach 0.27 and 7.5 atm (0.76 MPa)

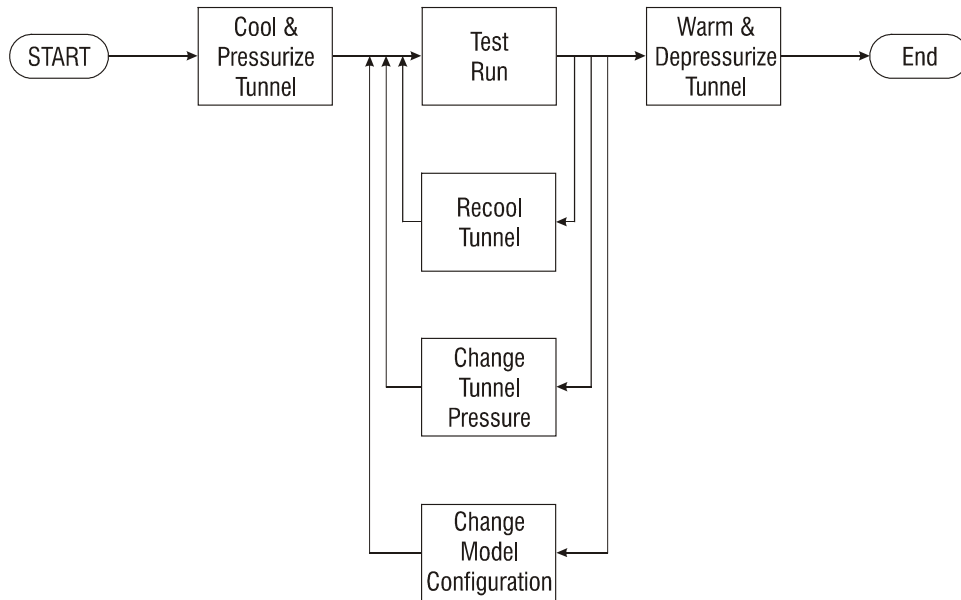


Figure 51. Operational sequence for test program.

There will be 40 model configuration changes in the initial set, plus 10 additional configurations that repeat 10 of the original configurations but with the model inverted to assess flow angularity. This will make a total of 50 configurations.

The detailed cost computations are compiled in Table 17.

Table 17. Detailed Cost Computation Table For Selected Operational Example

Event	#	Time each	Time total	Cost each	Cost total
Tunnel cooldown	1	10 hr	10 hr	\$192,500	\$192,500
Tunnel warm-up	1	10 hr	10 hr	\$7,200	\$7,200
Pressure change up	100	0.5 hr	50 hr	\$13,200	\$1,320,000
Pressure change down	100	0.5 hr	50 hr	0	0
Collect 20 data points	250	0.5 hr	125 hr	\$107.76	\$26,940
Model cooldown	50	1 hr	50 hr	\$4,725	\$236,250
Model warm-up	50	1 hr	50 hr	\$180	\$9,000
Model configuration change	50	4 hr	200 hr	---	---
Hours @ -250 °F (-157 °C)	525	1 hr	---	\$262.50	\$137,813
Total	---	---	545 hr	---	\$1,929,703

These results reflect a cost of almost \$2 million over the course of nearly 23 days. The average cost per data point is approximately \$386. The average time to collect a data point is 6.54 minutes, or 9.2 data points per occupancy hour.

The largest cost drivers are pressure changes (\$1,320,000), model cooldowns after changes (\$236,250), initial tunnel cooldown (\$192,500), and tunnel temperature maintenance (\$137,813). Costs for data collection runs are not as significant as might be expected (\$26,940). The largest time drivers are model changes (300 hours including warm-up and cooldown), data runs (125 hours), and pressure changes (100 hours).

Construction Cost and Schedule

The HiLiFT facility is envisioned as a fairly large project in terms of total cost and complexity of operations. It falls into a category of advanced technologies as many of the principles, although proven in smaller magnitudes, have yet to be enacted on a large scale. This estimate was compiled with the following points in mind.

Capital costs are repeatedly underestimated for advanced processes. Furthermore, the performance of advanced facilities constantly falls short of what was predicted by designers and assumed in any financial/cost analyses.

Greater than expected capital costs and unanticipated performance shortfalls can be explained in terms of the characteristics of the particular technology and the amount of information incorporated into estimates at various points in project development.

Factors that account for poor cost estimates and poor performance can largely be identified early in the development of the technology, long before major expenditures have been made for detailed engineering much less construction.

The accuracy of the capital cost estimate depends on the project phase. New technology entails some research and development (R&D) and progresses into project definition, detailed engineering design, construction, and finally start-up.

Cost estimates are typically developed in each of project phases and their accuracy derives from the knowledge base and methodology developed during that phase.

The methodology of estimating the current HiLiFT project facility is based on an R&D phase as defined in Table 18, as it fits most closely with the HiLiFT conceptual design concept. This is consistent with the amount of effort expended and limits spurious sophistication of estimating procedures and details, which can be self-defeating. *The Richardson Process Plant Construction Estimating Standards*, 1998 edition, was utilized where practical to provide a uniform estimating basis among all the project's systems.

Table 18. Project Phases And Cost Estimation Confidence Levels

Project phases	
Research and development	Entails a new process or equipment or principles significantly different from existing. Provides the basic theoretical understanding of the process to establish its feasibility. One or more “conceptual” cost estimates are made to screen out concepts, define scope, and define basic design of the process. Much of the information varies widely and is quite fluid in nature and thus these estimates vary widely. The target confidence level is typically $\pm 30\%$ to 40% .
Project definition	This effort marks the delineation of scope, layout, and process flow conditions. Most of the major equipment is defined, and the examination of sites is in process. Those projects with rigid requirements may have a confidence level of $\pm 20\%$. For those projects that do not have a rigid set of guidelines, the confidence level could be as high as $\pm 30\%$.
Engineering design	A decision to proceed with full engineering designs is generally based on the Project Definition Estimate. When engineering is about 30% complete, another cost estimate is developed. This estimate is used as a checkpoint to determine if the costs have increased substantially, as a basis for planning capital expenditures, and to establish the cost accounts that will be used to control expenditures during procurement and construction. The confidence level is $\pm 15\%$ to 20% .

The individual system costs were compiled into a total HiLiFT facility construction cost summary, which is shown in Table 19. This is a single-page high-level presentation with backup support from the individual cost estimates. This high-level facility cost estimate includes the appropriate contingency amounts to quantify the uncertainties in cost due to technology status, level of design detail available, and site specific factors. Two types of contingencies were used: 1) a project contingency to cover the uncertainty in the cost estimate itself, and 2) a process contingency to cover the uncertainty in the technical performance and commercial scale of the equipment. A project contingency of 30% was applied to this initial conceptual design detail effort. A process contingency of up to 30% was selectively applied on those major equipment items, which rely on conceptual, unproven ideas. In addition, a factor was applied for inflation to account for the time from when the estimates were prepared until facility construction occurs.

Table 19. Project Construction Cost Estimate Summary

System	Cost (\$000)
Tunnel shell (incl. 10% contingency)	69,662
Cart and sting (incl. 30% contingency)	8,993
Nitrogen system (incl. 15% contingency)	12,045
Maglev (incl. 30% contingency)	54,678
Buildings and grounds (incl. 20% contingency)	34,406
Project contingency (30%) and escalation (3%/year)	120,216
<i>Project construction total</i>	<i>300,000</i>

This construction cost estimate was used as input (ID#13) to compile an overall HiLiFT program cost estimate and schedule. These are presented as Table 20 and Figure 52.

Table 20. Total Project Cost Summary

ID	Task name	Cost (\$000,000)
1	Concept evaluation and technology survey	0
2	Feasibility study	1.3
3	Develop enabling technologies	2.0
4	Decision to proceed with HiLiFT Project	0
5	Determine requirements/conceptual design	2.0
6	Demonstration tests/pilot facility	34.0
7	Planning/design	2.0
8	Construction	27.0
9	Testing	5.0
10	Preliminary design	4.0
11	Full-scale facility	355.0
12	Design	45.0
13	Construction	300.0
14	Commissioning	10.0
15	Facility operational	0
	<i>Total project costs</i>	<i>398.3</i>

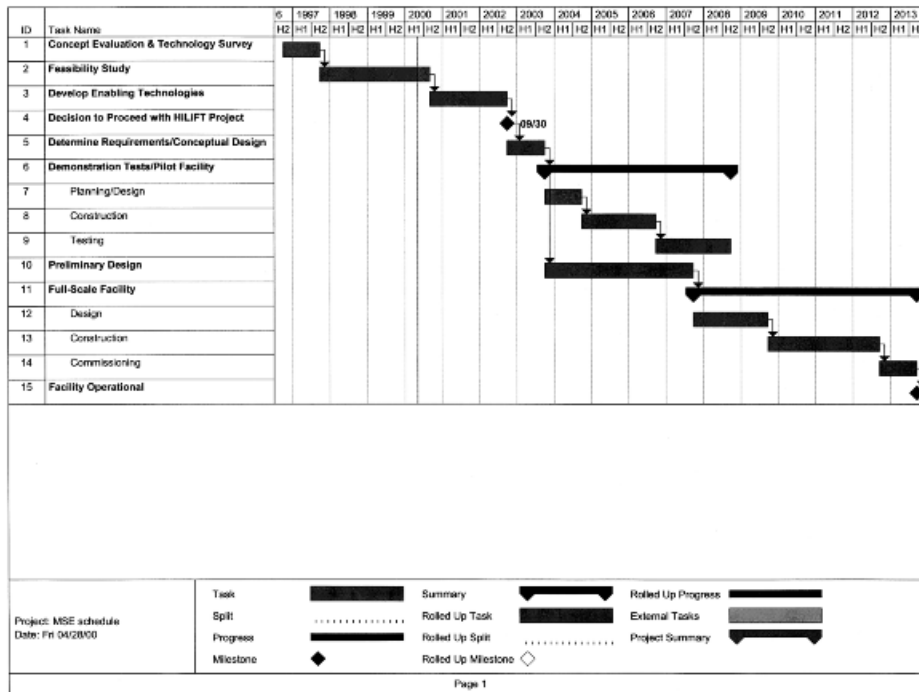


Figure 52. Project schedule.

Conclusions and Recommendations

It was established that a feasible tunnel can be constructed out of welded stainless steel that meets the requirements of the ASME Boiler and Pressure Vessel Code. Substantial analysis engineering remains to be done to complete the design, including constructing a model that would employ the same techniques.

The magnetic levitation and propulsion subsystem design and analysis validated the Phase I assessment regarding the feasibility and performance of these systems. Substantial work remains, however, as systems of this type have not been previously constructed. Subscale room temperature models must first be constructed with the model size increasing and the temperature range dropping until a reasonable scale model is shown to be feasible at cryogenic temperatures.

Aerodynamic analyses show that the HiLiFT facility will satisfy requirements, but that error correction algorithms will need to be applied to the raw data, as is currently done at other wind tunnel facilities. Additional analysis is required to incorporate design enhancements and detail. Error correction algorithms will need to be generated, and the analysis results need to be experimentally confirmed.

The initial cart design utilized a system with the model mounted in front of the cart on a long narrow sting, but this approach was found to be unworkable due to the flexibility of the sting and resulting model oscillations. It was determined that a pedestal for the model mounted on the cart is required. Along with this change, further research must be performed to demonstrate that the design can meet the stringent Mach number and model attitude control and measurement requirements. In addition, a model cart design and model dynamics analysis must be continued.

Due to low temperatures, low viscosity, and the high density of the nitrogen, temperature uniformity was difficult to establish using CFD models without experimental test data to validate results. Test data must be generated to closely establish the means of controlling the temperature within the tunnel.

Preliminary design was conducted for the rest of the facility subsystems including the nitrogen supply system, the electrical distribution system, as well as the buildings and grounds. No significant problems were identified in the designs; however, the question of power storage should be addressed since the fluctuation on the power grid could vary from a 80 MW draw from the grid during acceleration to a 70 MW return to the grid during regenerative braking.

Other analyses including safety, error/performance, operational costs, and productivity were completed.

A preliminary cost estimate and schedule were completed. The results indicate that a full-scale HiLiFT facility could be completed by 2013 for a cost of approximately \$398.3 million including development and design costs. As the design progresses, the cost and schedule will require periodic updating.

Prior to proceeding with Phase III, it is recommended that the model cart design be changed to a pedestal mount and the model dynamics be reassessed to completely validate the HiLiFT concept's conformance to requirements. If this produces an acceptable system, a conceptual design should be completed to ensure that individual subsystem designs are complementary and that the analyses use a consistent data set. During all of the Phase III activities it will be necessary to update the conceptual design to ensure the continuing relevance of test objectives for concurrent and follow-on demonstrations and analyses.

During Phase III, the emphasis will be on subsystem and overall concept demonstration using simplified or subscale hardware. Key Phase III demonstrations include:

- Tunnel design and manufacture – design and fabricate a section of tunnel, including insulation and acoustic material, then pressurize and cool the section to validate design and analysis assumptions and techniques including alignment of the magnetic levitation guideway.
- Thermal design and analysis – use the tunnel section or some other testbed to validate assumptions on thermal behavior especially as it pertains to the length of time needed to establish convection currents and their magnitude.
- Magnetic levitation and propulsion development – starting with small, room temperature models and working up to large cryogenic models to resolve analytical and design issues.
- Cart – develop a pedestal mount for the model and resolve control and measurement issues with respect to model attitude, vibrational resonant modes, and cryogenic performance through the use of CFD and subscale models working up to full-scale models.
- Aerodynamics – continue analytical efforts concurrently with other design efforts to ensure the aerodynamic environment is not compromised, continue development of data correction algorithms, and conduct subscale testing as required to validate assumptions and analysis methods.

At conclusion of Phase III, all key subsystem and concepts will have been validated, and the results of the testing and analysis will have been incorporated into a single consistent system design. Full-scale and detailed design efforts can then follow Phase III with confidence in the required technology, implementation, data quality and quantity to be expected, and cost and schedule estimates.

References

1. HiLiFT Project Phase I, Design Report, MSE Technology Applications, Inc., NASA-2, July 1998.
2. High Lift Flight Tunnel Project Feasibility Study, Final Report, MSE Technology Applications, Inc., NASA -23, July 1999.
3. Rote, Donald M.: "Low Temperature Effects on Magnetically Levitated and Propelled Cart and Associated Systems –An Assessment," Argonne National Laboratory, April 1999.
4. Rae, W.H., and Pope, A.: *Low-Speed Wind Tunnel Testing*, John Wiley and Sons, NY, 1984.
5. Hoerner, S.F.: *Fluid-Dynamic Drag*, published by the author, 1965.
6. Currie, I.G.: *Fundamental Mechanics of Fluids*, McGraw-Hill, New York, NY, 1974.
7. Katz, J., and Plotkin, A.: *Low-Speed Aerodynamics*, McGraw-Hill, New York, NY, 1991.
8. Aihara, Y., Koyama, H., and Murashige, A.: "Transient Aerodynamic Characteristics of a Two-Dimensional Airfoil During Stepwise Incidence Variation," *J. Aircraft*, 22(8), 1985, pp. 661–668.
9. Crow, S.C. and Bate, E.R.: "Lifespan of Trailing Vortices In A Turbulent Atmosphere," *J. Aircraft*, 13(7), 476–482, 1976.
10. Hinze, J.O.: *Turbulence*, McGraw-Hill, New York, N.Y., 1959.

REPORT DOCUMENTATION PAGE			Form Approved OMB No. 0704-0188	
Public reporting burden for this collection of information is estimated to average 1 hour per response, including the time for reviewing instructions, searching existing data sources, gathering and maintaining the data needed, and completing and reviewing the collection of information. Send comments regarding this burden estimate or any other aspect of this collection of information, including suggestions for reducing this burden, to Washington Headquarters Services, Directorate for Information Operations and Reports, 1215 Jefferson Davis Highway, Suite 1204, Arlington, VA 22202-4302, and to the Office of Management and Budget, Paperwork Reduction Project (0704-0188), Washington, DC 20503.				
1. AGENCY USE ONLY (Leave blank)		2. REPORT DATE December 2000	3. REPORT TYPE AND DATES COVERED Contractor Report	
4. TITLE AND SUBTITLE High-Lift Flight Tunnel - Phase II Report			5. FUNDING NUMBERS PO L-8871 WU 522-17-41-20	
6. AUTHOR(S) David Lofftus, Thomas Lund, and Donald Rote				
7. PERFORMING ORGANIZATION NAME(S) AND ADDRESS(ES) MSE Technology Applications, Inc. 200 Technology Way P.O. Box 4078 Butte, MT 59702			8. PERFORMING ORGANIZATION REPORT NUMBER NASA-33	
9. SPONSORING/MONITORING AGENCY NAME(S) AND ADDRESS(ES) National Aeronautics and Space Administration Langley Research Center Hampton, VA 23681-2199			10. SPONSORING/MONITORING AGENCY REPORT NUMBER NASA/CR-2000-210653	
11. SUPPLEMENTARY NOTES Langley Technical Monitor: Dennis M. Bushnell				
12a. DISTRIBUTION/AVAILABILITY STATEMENT Unclassified-Unlimited Subject Category 09 Distribution: Standard Availability: NASA CASI (301) 621-0390			12b. DISTRIBUTION CODE	
13. ABSTRACT (Maximum 200 words) The High-Lift Flight Tunnel (HiLiFT) concept is a revolutionary approach to aerodynamic ground testing. This concept utilizes magnetic levitation and linear motors to propel an aerodynamic model through a tube containing a quiescent test medium. This medium (nitrogen) is cryogenic and pressurized to achieve full flight Reynolds numbers higher than any existing ground test facility world-wide for the range of 0.05 to 0.50 Mach. The results of the Phase II study provide excellent assurance that the HiLiFT concept will provide a valuable low-speed, high Reynolds number ground test facility. The design studies concluded that the HiLiFT facility is feasible to build and operate and the analytical studies revealed no insurmountable difficulties to realizing a practical high Reynolds number ground test facility. It was determined that a national HiLiFT facility, including development, would cost approximately \$400M and could be operational by 2013 if fully funded. Study participants included National Aeronautics and Space Administration Langley Research Center as the Program Manager and MSE Technology Applications, Inc., (MSE) of Butte, Montana as the prime contractor and study integrator. MSE's subcontractors included the University of Texas at Arlington for aerodynamic analyses and the Argonne National Laboratory for magnetic levitation and linear motor technology support.				
14. SUBJECT TERMS high lift, wind tunnel, pressurized cryogenic, subsonic, magnetic propulsion, high Reynolds number			15. NUMBER OF PAGES 91	
			16. PRICE CODE A05	
17. SECURITY CLASSIFICATION OF REPORT Unclassified	18. SECURITY CLASSIFICATION OF THIS PAGE Unclassified	19. SECURITY CLASSIFICATION OF ABSTRACT Unclassified	20. LIMITATION OF ABSTRACT UL	